VERTICAL AIR PROFILING IN FALSE BAY

STUDENT: **Benita Maritz**

Student Number: **MRTBEN004**

SUBMITTED TO THE UNIVERSITY OF CAPE TOWN
In fulfilment of the requirements for the degree

MSc Ocean and Atmosphere Sciences

Faculty of Oceanography

UNIVERSITY OF CAPE TOWN

Date of submission:	**October 2019**
Supervisor [s]:	**Dr K Altieri** **University of Cape Town**
	Prof AMJ van Ejik **NO, Oude Waalsdorperweg 29, 2597 AK** **The Hague, The Netherlands**

DECLARATION

I, *Benita Maritz*, hereby declare that the work on which this dissertation/thesis is based is my original work (except where acknowledgements indicate otherwise) and that neither the whole work nor any part of it has been, is being, or is to be submitted for another degree in this or any other university.

I empower the university to reproduce for the purpose of research either the whole or any portion of the contents in any manner whatsoever.

Signature: ….Signed by candidate

Date: 14 October 2019

Table of Contents

ABSTRACT

Marine surface layer micrometeorology mainly constitutes vertical turbulent fluxes of parameters such as momentum, heat, water vapour and aerosols. These turbulent fluxes have been tested in the laboratory and can be applied to the atmospheric changes over the ocean, where wind speed, the air-sea temperature difference (ASTD) and humidity play a major role. Due to the difficulty of actually measuring these changes directly, equations were derived that describe the micrometeorology in terms of actual meteorological observations. The theory of micrometeorology in turn provided the accepted calculations to predict vertical profiles for wind speed, air temperature and humidity. Nevertheless, using micrometeorology theory to predict atmospheric conditions over the ocean proves to be more difficult than over land. This is mainly due to the complex nature of the oceanic environment and its interaction with the atmosphere directly above it.

The primary objective of this work was therefore to investigate the potential of deploying a Helikite in order to characterise the lower atmosphere in False Bay. Focus was placed on the methods to correctly measure air profiles over the ocean up to a maximum height of 200 m. A description of the system set-up, data acquisition, deployment parameters and data analysis are discussed. The second objective was to evaluate the micrometeorology theory used in a micrometeorological model for the marine surface layer with False Bay data. This was achieved by using experimental data to run the model. The model output was then compared to the experimental profile measured as part of objective one. The micrometeorological model it aimed to assess is based on the standard bulk meteorological observations of wind speed, temperature, humidity and the turbulent fluxes of momentum, heat and water vapour.

Analysis of the various environmental parameters showed a complex oceanographic and atmospheric system. The air profiles recorded for this study were recorded in an area where smaller scale local effects were dominant, which could explain some of the discrepancies encountered when attempting to reproduce the measured profiles using micrometeorology bulk parameterisations. The four profiles described in this thesis were grouped with two profile days showing a good comparison between the predicted and measured profiles. Results also indicated that micrometeorology theory perform better when using the 'bucket' Sea Surface Temperature (SST) at 0.5 m below the surface.

LIST OF FIGURES

LIST OF TABLES

ABBREVIATIONS

ABL	Atmospheric Boundary Layer
ASIS	Air-Sea Interaction Spar
ASL	Atmospheric surface layer
ASTD	Air Sea Temperature Difference
AWAC	Acoustic Waves and Currents
COTS	Commercial-Of-The-Shelf
CSIR	Council for Scientific and Industrial Research
CTD	Conductivity Temperature Depth profiler
EM	Electromagnetic
EO	Electro-Optics
EOSTAR	Electro-Optical Signal Transmission And Ranging
FESTER	First European – South African Transmission ExpeRiment
FOV	Field of View
GPS	Global Positioning System
IMT	Institute for Maritime Technology
INS	Inertial Navigation System
IOP	Intensive Observation Periods
IR	Infrared
LWIR	long wavelength infrared
MPL	Micro pulse lidar
MW	Microwave
ODV	Ocean Data View
PVC	Polyvinyl Chloride
RRL	Roman Rock Lighthouse
SR	Scaning Radiometer
SST	Sea Surface Temperature
TARMOS	Turbulence And Refraction Modelling Over the Sea
TNO	Netherlands Organization for Applied Scientific Research

CHAPTER 1: GENERAL INTRODUCTION

In any study that deals with the lower atmospheric conditions, it is important to first have a basic understanding of the atmospheric boundary layer (ABL) (Arya, 2001) and how micrometeorology relates to this. The ABL is defined as the layer where a fluid (gas or liquid) comes in contact with, or is in the immediate vicinity of, the Earth's surface. At this boundary layer an exchange of either heat, momentum or mass can take place between the fluid and the surface. This layer varies in thickness from tens of meters to several kilometres. The thickness of this boundary layer is dependent on the heating or cooling rate of the surface area, winds, topographic landscape and horizontal advection of moisture and heat. Over land surfaces, it displays diurnal variations with a thicker (deeper) ABL (1-5 km) in the afternoon, due to continuous surface heating by the sun. Cooling of the surface at night will reverse the effect and the weakened turbulent mixing causes a shallower ABL (less than 1 km). This diurnal cycle is also evident in other meteorological parameters such as wind, air temperature and other atmospheric properties.

The maritime atmospheric boundary level will exhibit different dynamic properties, with unique challenges in applying theory (Kettle, 2015). Factors such as wind speed, air temperature, sea surface temperature and wind directions will add to the complexity in describing the ABL in a marine environment. Turbulence at the boundary level will be highly dependent on the atmospheric stability, highlighting the importance of the air-sea temperature difference.

Although turbulent flow occurs throughout the ABL it is especially prominent in the atmospheric surface layer (ASL), which constitutes the lower 1/10 of the ABL (Arya, 2001). Micrometeorology deals with the small-scale, localised atmospheric conditions where the scope is limited to the lower atmosphere and how it interacts with the earth's surface, i.e. ASL (Bauer, 1996) (Figure 1). Important parameters that fall within the micrometeorology scope in the ASL include energy (heat) and momentum exchange between the Earth's surface and the atmosphere (Arya, 2001). In the maritime domain, which is the focus of this thesis, surface fluctuations on the temporal and spatial scale are important to the remote sensing discipline and air-sea interaction studies (G L Geernaert, 1990).

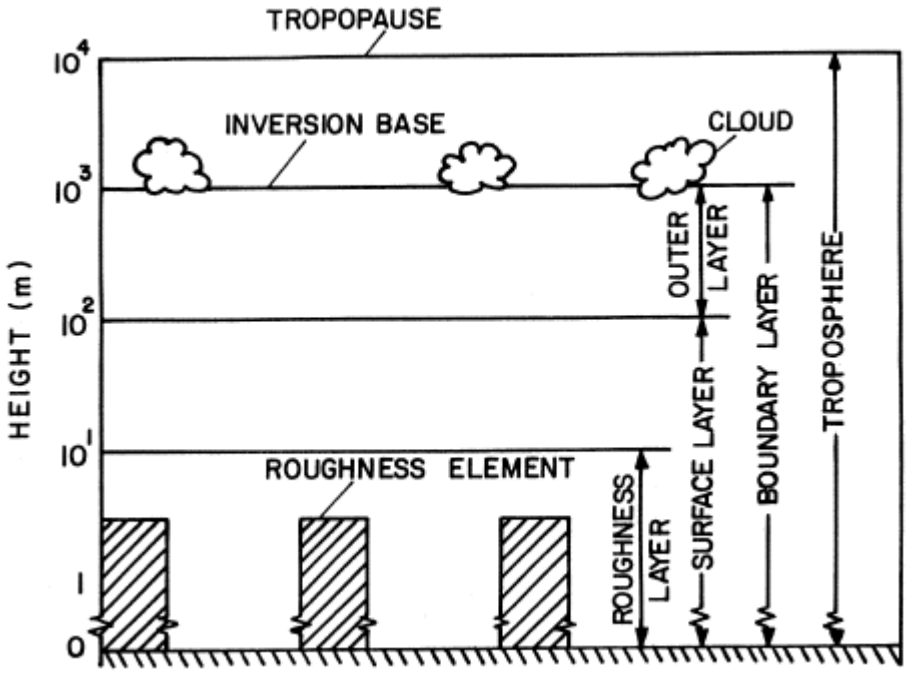

Figure 1: Schematic of the planetary boundary layer as part of the troposphere (Arya, 2001)

The theory of micrometeorology provides equations for turbulent surface fluxes that allow for calculating the vertical profiles of parameters such as wind speed, air temperature and humidity within the ASL (Kunz, 1996). This framework has been tested in a laboratory under controlled conditions as well as in the field. In view of the difficulty of actually measuring the turbulent fluxes in the atmosphere, as well as the difficulties in obtaining the input parameters for the flux equations, the methodology is often reversed. In that case, actual meteorological observations from one or two heights are used in the micrometeorological equations to infer the turbulent surface fluxes. Then, the micrometeorology in turn provides the vertical profiles for wind speed, air temperature and humidity. Nevertheless, using micrometeorological theory to predict atmospheric conditions over the ocean proves to be difficult, with the surface waves adding an additional complication. Consequently, the validity limitations of the theory are regularly challenged, which implies that the actual profiles may not correspond to the theoretical predictions. Specialists in the field (e.g., J.B. Edson, University of Connecticut) informally suggest that micrometeorology only applies 40 – 50% of the time over the oceanic surface (A.M.J. van Eijk, personal communication). This shows that there are many cases where the flow in the lower atmosphere is not fully governed by the surface fluxes. Considering the suggestion above that micrometeorology does not always guarantee a correctly predicted profile in all conditions, actual data from air profiles taken over the ocean in coastal areas could prove beneficial in verifying numerical models that are based on the micrometeorology theory.

The measuring of atmospheric conditions in the lower 200 m over the ocean is also of interest for the understanding of electro-optical (EO) propagation over the ocean. As EO propagation over the ocean could be a possible application for this work, Section 2.6 is included to briefly introduce EO and the effects of the environment thereon. EO propagation in the marine environment is a complex problem and is affected by various parameters including the air-sea temperature difference (ASTD) and atmospheric conditions across the transmission path. Although this study will compare measured vertical profiles to micrometeorological theory, the results of this thesis will also aid in evaluating a micrometeorological module in an EO propagation model. The EO propagation model was developed specifically for use in the naval operational arena. The value added through this research of understanding the environmental effects on EO propagation is of high importance, as the EO sensor suite forms an important part of naval operations.

This thesis forms part of the larger international experiment called the 'First European – South African Transmission ExpeRiment' (FESTER), which took place from April 2015 to February 2016 in False Bay, South Africa (Figure 7 in Section 3). FESTER covered multiple topics related to atmospheric physics, oceanography and electro-optic sensor performance. One of the sub-projects during this experiment included the use of a Helikite system for characterising the atmosphere up to 100-200 meters, which allowed the opportunity to gain experience with the deployment. Results from this investigation form the backbone of this thesis and allow for an evaluation of the applicability of micrometeorology models in describing meteorological profiles in the study area (False Bay). This thesis therefore had two key objectives.

The primary objective was to investigate the potential of deploying a Helikite in order to characterise the lower atmosphere. Focus was placed on the methodology to correctly measure meteorological profiles over the ocean up to a maximum height of 200 m. A description of the system set-up, data acquisition, deployment parameters and data analysis is provided in Sections 3 and 4. During the FESTER experiment, an opportunity to conduct a vertical profile using the sensor package developed for this experiment as described in Section 3.2 and the other from a conventional Radiosonde arose. In this case both sensor packages were attached to the Helikite. The comparison of the simultaneous vertical profiles are presented and discussed in Section 4.3

The second objective was to evaluate the suitability for using the micrometeorology theory to describe the marine surface layer in False Bay. Actual local, single-height observations (from the Helikite) were used to drive the bulk micrometeorological model and the output was compared to the vertical profiles measured with the Helikite (Section 4). The bulk micrometeorological model, used in this thesis for comparison with the measured Helikite profiles, is a module in the Electro-Optical Signal Transmission And Ranging (EOSTAR) model which predicts EO propagation. This module is described in Section 2.4.

CHAPTER 2: LITERATURE REVIEW

This Chapter is divided into multiple sections dealing with the different components and background information. Although the FESTER experiment had a mostly operational emphasis, calling for the results from this study in a more applied context, the thesis objectives required an understanding of the micrometeorology which forms the basis of the Tactical Decision Aid (TDA) module that was assessed. As the theory for predicting the lower atmospheric conditions is largely based on micrometeorology a basic understanding of this topic is necessary – not only in understanding the complexities, but also to ensure that any technical experiments to measure air profiles were conducted correctly. For this reason a section is dedicated to micrometeorology. A section on turbulence is also included as it is closely related to micrometeorology (Section 2.2).

The TDA module, known as Turbulence And Refraction Modelling Over the Sea (TARMOS) (Kunz, 1996), will also be discussed as a separate topic (Section 2.4), as well as a generic discussion on the bulk parameterizations for micrometeorological models (Section 2.3). As the main objective of this thesis is to investigate the possibility of using a Helikite to measure air profiles and to use the data in support of the TDA model, various approaches of measuring air profiles are also reviewed (Section 2.5). Sections 2.3 and 2.5 are inspired by the review provided by G.L. Geernaert, 1990 and referenced as such.

Finally, it is important to discuss some of the basic principles relating to EO propagation as it was highlighted as a possible application for the characterisation of the atmosphere using a Helikite. These principles are included in Section 2.6. This section will also summarise the effects of the atmosphere on that of the EO propagation path.

2.1 Overview of micrometeorology

Micrometeorology can simply be described as the detailed study of the small scale, spatial structure of flow and thermodynamics in a specific area (Figure 2). The driving forces in this small scale, spatial structure include turbulent flow and momentum, heat and moisture fluxes and the radiation budget (Arya, 2001). The rate of warming or cooling of any surface in the ABL is determined by the net radiation at the surface and the change of this radiation that occurs with height.

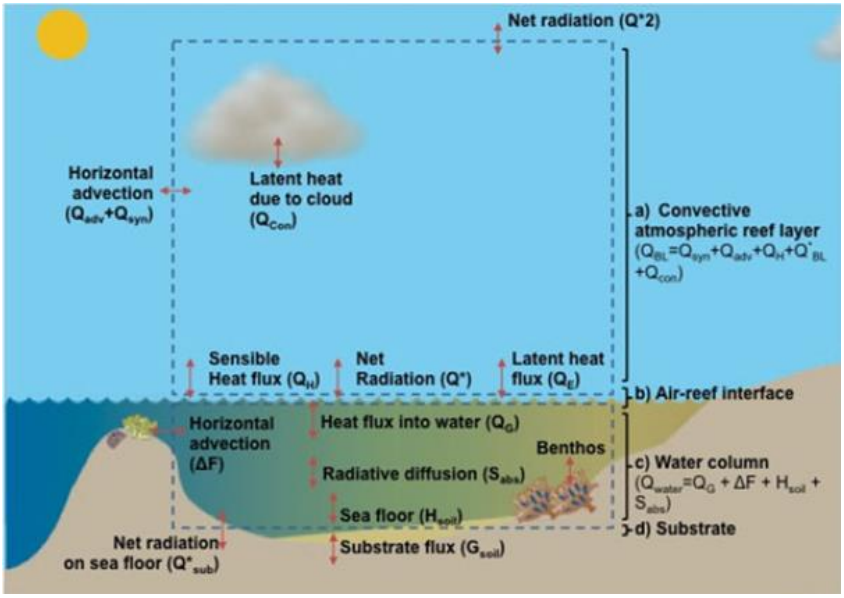

Figure 2: Basic schematic diagram illustrating the heat budget parameters for the (a) convective atmospheric boundary layer, (b) surface energy balance at the air-sea interface, (c) water column, and (d) through the substrate (in shallow water) (MacKellar, McGowan, & Phinn, 2013)**.**

When observing heat fluxes, three contributing terms can be identified. Firstly, the net radiation to or from a surface. This radiation flux constitutes the external forcing, which is not explicitly considered in the micrometeorology framework. The second term represents the sensible (direct) and latent (indirect) heat fluctuations between the atmosphere and the surface and lastly the third term deals with the heat transfer in or out of a sub-medium (either soil or water) (Arya, 2001).

Therefore, the principle of conservation of energy at a surface can be described by equation (2.1.1). It describes how the net radiation must be balanced at the surface by a combination of the sensible and latent heat fluxes as well as the transfer to and from a sub medium (Arya, 2001).

$$R_N = H + H_L + H_G \tag{2.1.1}$$

Where:

R_N is the net radiation

H is the sensible heat flux

H_L is the latent heat flux

H_G is the ground heat flux

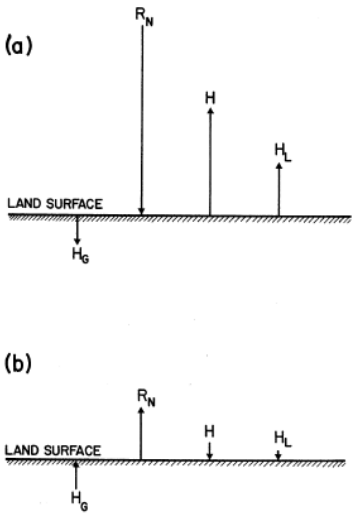

Figure 3: Schematic showing typical surface energy budgets during the day (a) and night (b) over a land surface (Arya, 2001)

The radiation balance at the surface usually has a diurnal pattern. During the day, the sun's energy (solar radiation) is directed at the surface, resulting in heating of the surface and the air directly above it (Figure 3 (a)). At night this reverses, and the radiation is rather directed away from the surface, cooling the surface and the air above (Figure 3 (b)). Temperature differences between the air and the surface give rise to the sensible heat flux. The energy budgets of water surfaces are more complex, due to its fluid nature. Since water acts as a thermal reservoir, the diurnal variation in heat changes over the ocean is generally smaller than over land. Water surfaces are actively moving and the surface boundary layer or mixed layer is generally turbulent. Thus, the ground level heat flux (H_G) is determined by the convective and advective heat transfers in the water. Direct measurements of the energy budget are largely lacking in this instance. However, sensible and latent heat fluxes are routinely measured and it has been shown that latent heat energy will dominate in most of the ocean areas (Arya, 2001). The ratio between sensible (direct heat) and latent (indirect) heat fluxes is called the Bowen Ratio (B) (Arya, 2001) and can be described by the following equations as derived from (2.1.1).

$$H = \frac{R_N - H_G}{1 + B^{-1}} \tag{2.1.2}$$

$$H_L = \frac{R_N - H_G}{1 + B} \tag{2.1.3}$$

The indirect or latent heat instability is also referred to as water vapour flux and is the result of evaporation or condensation. During evaporation heat is taken up resulting in a cooling of the surface and a transfer of energy from the surface to the air above. This process of evaporation generally occurs during the day. Condensation will typically occur when the surface is colder than the surrounding air, therefore the transfer of energy will be reversed and energy will be transferred from the air to the surface (Arya, 2001).

Most of the radiation balance in the atmosphere occurs in the 0.1-100µm frequency range of the electromagnetic wavelength spectrum (Arya, 2001). The radiative flux is defined as the amount of radiant energy received or released by a unit area of a surface per unit time. A blackbody is defined as an object that produces the "maximum possible radiation per unit area of its surface per unit time, at all wavelengths" i.e. the perfect radiator. The emitted radiant energy that is produced per wavelength for a blackbody is described by Planck's law as a function of the surface temperature (2.1.4).

$$R_\lambda = \left(\frac{2\pi h_p c^2}{\lambda^5}\right)\left[\exp\left(\frac{h_p c}{b\lambda T}\right) - 1\right]^{-1} \quad (2.1.4)$$

Where:

h_p is Planck's constant ($6.626 \cdot 10^{-32}$ Js)

b is the Boltzmann constant ($1.381 \cdot 10^{-36}$ JK^{-1})

R_λ is the radiative energy flux density per unit wavelength

λ is wavelength

c is the speed of light in a vacuum

Natural surfaces are considered to be grey bodies as they are not perfect radiators and are characterised by their radiative properties. These radiative properties are emissivity, absorptivity, reflectivity and transmissivity (Arya, 2001). Emissivity (ε_λ) is defined as the ratio of energy change released by a surface, compared to the energy radiated by a blackbody, at a given temperature and wavelength. The ratio of radiant energy absorbed by a surface material and the total amount of energy incident on the surface is known as absorptivity (α_λ). Absorptivity is dependent on the wavelength. Reflectivity (r_λ) is the ratio of the radiation reflected and the total amount of radiation incident on the surface. Transmissivity (t_λ) is defined as the ratio of energy transferred to a subsurface medium and a total amount incident on the surface. According to Kirchhoff's law, the emissivity

and absorptivity for a specific material at a given wavelength are equal. Both the parameters are therefore equal to one for a blackbody.

The energy budget near the earth's surface is dependent on the integrated radiative changes from all the wavelengths. The term albedo is used to define an integrated reflectivity index for shortwave surface radiation (0.15 - 4µm) (Arya, 2001). Shortwave radiations' main source of energy is the sun (solar radiation). Solar radiation is depleted as it passes through the atmosphere due to scattering and absorption by clouds, atmospheric aerosols and molecules. In the natural environment snow has a high albedo (i.e. very effective reflector of solar energy), with water on the other end of the spectrum with the lowest albedo (higher absorption of the energy) at a perpendicular angle. Water can be a strong reflector under grazing angles.

In a typical electro-optical sensor application, which will ultimately benefit from the data and knowledge gained in this study, the net radiation flux will have an influence on the radiant intensity of the image perceived by the sensor (Kunz, 1996).

2.2 Turbulence

Theoretically the flow in fluids can be broadly divided into either ideal flow (inviscid) or viscous flow (Ayra, 1988). In an ideal flow scenario, the effects of viscosity are ignored and the flow is described as non-turbulent. This type of movement is smooth and flow between layers and even different surfaces are without any friction. Ideal flow is generally only present in the absence of boundary layers or density interfaces. Viscous (or turbulent) flow is therefore required to theoretically describe the processes at the boundary or interfacial mixing layers. The fluid viscosity can be defined as "the measurement of the internal resistance of the fluid to deformation" (Ayra, 1988) and occurs on a molecular level. The frictional resistance between the layers causes the flow to be viscous. This resistance force is calculated per unit area and is associated with the shearing motion or variation of velocity between layers, which is known as the shearing stress. The terms laminar and turbulent flow are used to broadly describe all possible viscous flows (Ayra, 1988). Laminar flow is similar to inviscid flow, as it occurs in a smooth, orderly fashion with adjacent layers sliding past each other with limited mixing. Laminar flow is however different in the fact that momentum, heat and mass are transferred on a molecular level between the different fluid layers. In contrast, turbulent flows are more random, fluctuating over a wide temporal and spatial scale.

The flow occurring in the atmospheric boundary layer (ABL) is often turbulent in nature (Tennekes, H. and Lumley, 1972). In the ABL these turbulent fluctuations could be in the order of 10^{-3} to 10^{4} seconds (temporal) and 10^{-3} to 10^{4} m (spatial). The turbulent velocity at a given point is usually described statistically, as it is difficult to predict due to its random nature(G L Geernaert, 1990).

When discussing atmospheric turbulence it is first necessary to have a basic understanding of the nature of turbulence. There are five general characteristics of turbulence that contribute to its random nature. Irregularity (or randomness of the flow) essentially renders turbulent flow unpredictable, which is one of the reasons statistical descriptions are used in practice (Ayra, 1988). Diffusivity describes the ability to mix fluids and can be listed as the most important property in turbulence, as it governs the efficient distribution and rapid mixing of momentum, heat and mass transfer in flows. It is also responsible for evaporation in the atmosphere, and will increase the transfer of momentum between the ocean currents and the wind. The velocity fields in turbulent flow are three-dimensional and vary in time and space leading to a highly rotational vorticity field. Dissipation refers to the kinetic energy that is constantly converted into internal energy or heat, highlighting the fact that in order to have turbulent flow a constant energy source is required (Ayra, 1988). Without this constant energy supply the turbulence will dissipate rapidly (Tennekes, H. and Lumley, 1972). Finally, all turbulent flow can be described by a wide range of scales (e.g., a velocity scale).

A key parameter for the characterization of flows is the Reynolds number (Ayra, 1988), which describes the relationship between laminar and turbulent flow. Otherwise stated, the Reynolds number is a non-dimensional parameter defining the ratio between inertial forces and viscous flow (Ayra, 1988). This ratio provides the relative importance of inertial forces when compared to viscous forces (2.2.1).

$$R_e = \frac{uL}{v} \tag{2.2.1}$$

Where:

R_e is the Reynolds number

u is the velocity scale

L is the length scale

v is the fluctuating viscosity component

At low Reynolds numbers (< 10^3), the flow will be laminar. Laminar flow will start exhibiting turbulent flow characteristics when the Reynolds number increases and flow instabilities appear. Large Reynolds numbers ($10^6 – 10^9$) are generally encountered over most natural surfaces in the atmospheric boundary layers (Ayra, 1988), leading to the conclusion that turbulent flow are most relevant to this thesis as it aims to describe the first 200 m of the lower atmosphere, where the local wind shear stress, larger scale convergence and atmospheric stratification drive the flow (G L Geernaert, 1990).

Both laminar and turbulent flow contribute to the exchanges between the atmosphere and the Earth's surface. Although turbulent flow is the main driving force behind the effective mixing and exchange of mass, heat and momentum throughout the ABL (Arya, 2001), laminar flow is often in the thin micro-layer close to the air-sea interface (G L Geernaert, 1990). The atmospheric micro-layer depth is around 1 mm and is referred to as the viscous sublayer. The viscous sublayer is the space directly above the sea surface that does not directly conform to the widely accepted micrometeorology, and is best defined over flat, glassy seas (Wesely, 1980). In this thin layer, which is in contact with the surface, heat and water vapour exchanges occur in the vertical plane and are molecular in nature.

The two types of turbulence present in the ABL are: mechanical due to surface friction and wind shear, and convective due to the surface heating and buoyancy. Mechanical turbulence is also referred to as "forced convection" and convective as "free convection" (Arya, 2001).

Momentum transfer via turbulence between the Earth and the atmosphere causes wind drag, which is responsible for the generation of waves and currents in the ocean (Arya, 2001). Other examples of turbulent flow in the natural environment include the atmospheric boundary level and jet streams in the troposphere (Tennekes, H. and Lumley, 1972), which in turn contribute to the effective mixing of the lower atmosphere. Turbulent flow also encourages evaporation, which produces latent heat adding to the surface energy budget, especially over large water bodies (Arya, 2001). Larger scale convergence and vorticity, local wind shear, stratification and the lower boundary characteristics are also considered to be driving forces of the turbulent flow in the surface layer (G L Geernaert, 1990).

An unstable lower atmosphere is characterised by a slight decrease in wind stress (momentum) and temperature (heat flux) with an increase in height. The stratification caused by sun-heating of a surface is thermally unstable (Garratt, 1994), and will lead to turbulence. The result of turbulence in unstable atmospheric conditions is a well-mixed layer, usually occurring during the day. A temperature inversion layer (where the temperature will increase rapidly with height) often occurs above this well-mixed layer (G L Geernaert, 1990). In contrast if the lower atmosphere is well stratified and there is no or little turbulence, the atmosphere is considered to be stable. Over land, this mostly occurs at night (Garratt, 1994), as a result of long wave emission into space which causes cooling.

A well-defined, stable layer that varies in depth is often found above the unstable boundary layer (typically between 2 and 3 km altitude), (Garratt, 1994) forming a boundary that is almost impenetrable for turbulent motions caused by the heat fluxes. This boundary is however poorly defined during stable conditions and is generally found lower in the atmosphere (between 50 – 100 m), especially over land on a clear windless night.

The ABL depth is quite low over the open ocean, but it generally exhibits a similar structure to that found over land. However, the oceanic environment differs from land, and exhibits its own features. As an example, during an experiment in the North Atlantic (JASIN experiment) it was found that in coastal regions where warm air flows from land over a cooler ocean, a near-neutral stability profile can be formed giving rise to a shallow boundary layer (0.5 km) (Garratt, 1994).

Mathematically (G L Geernaert, 1990), the motions in fluid flow (and hence turbulence in the atmosphere) are described by the Navier-Stokes equations:

$$\begin{cases} \dfrac{\partial u_i}{\partial x_i} = 0 \\ \dfrac{\partial u_i}{\partial t} + u_j \dfrac{\partial u_i}{\partial x_j} = f_i - \dfrac{1}{\rho}\dfrac{\partial p}{\partial x_i} + \nu \dfrac{\partial^2 u_i}{\partial x_j \partial x_j} \end{cases} \tag{2.2.2}$$

Where:

u is the velocity

x_i is a coordinate (I = 1,2,3)

t is time

ρ is density

p is pressure

f_i represents the external forces.

These equations can be simplified by time-averaging, which exploits the idea of Osborne Reynolds that any instantaneous quantity φ can be decomposed in time-averaged ($\bar{\varphi}$) and fluctuating quantities (φ'):

$$\varphi = \bar{\varphi} + \varphi' \tag{2.2.3}$$

It can be shown that the mean of the fluctuating component is zero. Using this property, the Reynolds-averaged Navier-Stokes (RANS) equation can be derived:

$$\rho\bar{u_j}\frac{\partial\bar{u_\iota}}{\partial x_j} = \rho\bar{f_\iota} + \frac{\partial}{\partial x_j}\left[-\bar{p}\partial_{ij} + \mu\left(\frac{\partial\bar{u_\iota}}{\partial x_j} + \frac{\partial\bar{u_j}}{\partial x_i}\right) - \rho\overline{u_i'u_j'}\right] \tag{2.2.4}$$

Where:

∂_{ij} represents the Kronecker delta

μ the dynamic viscosity.

The left-hand term represents the change in mean momentum of the fluid, due to the terms on the right-hand: mean external force, mean pressure, viscous stress and apparent stress, respectively. The apparent stress is generally referred to as Reynolds stress and arises from turbulence, as indicated by the fluctuating components.

The impact of the Reynolds stress terms on the flow can be explained by depicting horizontal layers of air with different horizontal velocities and temperatures. Vertical velocity incursions from slower parcels will tend to slow the faster flow down. However, when faster parcels of air intrude into a slower stream, the slower flow will speed up, which will hold true for temperature as well where warmer pockets will warm the cooler air. This interaction between the different air parcels introduces (vertical) momentum as well as convective turbulence.

2.3 Generic description of the bulk parameterizations for micrometeorological models

When using the well-defined and established micrometeorology theory to describe various parameters related to surface fluxes, it is important to first have an understanding of the bulk parameterisations used. These parameterisations are empirical equations that characterise the air-sea fluxes, which are a result of complex turbulent processes, in a simple form (Birol Kara, Rochford, & Hurlburt, 2000). These formulas include atmospheric parameters that can be measured easily like near-surface wind speed, air temperature and specific humidity, as well as the sea surface temperature. For atmospheric physics 'near-surface' usually refers to 10 m above sea level (Birol Kara et al., 2000).

The surface fluxes of heat (H), water vapour (E) and momentum or stress (τ), are related to the measured atmospheric bulk parameters through the transfer coefficients C_H, C_E and C_D, respectively (Liu, Katsaros, & Businger, 1979):

$$H = c\rho\,\overline{w'T'} = c\rho C_H(U - U_s)(T_s - T) \tag{2.3.1}$$

$$E = \rho\,\overline{w'Q'} = \rho C_E(U - U_s)(Q_s - Q) \tag{2.3.2}$$

$$\tau = -\rho\,\overline{w'u'} = \rho C_D(U - U_s)^2 \tag{2.3.3}$$

where ρ is again density, c is the isobaric specific heat of air, U, T and Q are wind speed, (potential) temperature and specific humidity at a reference height of 10 m, respectively, and U_s, T_s and Q_s refer to the respective values at the sea surface. Within the fluctuating components, u' refers to a horizontal and w' to a vertical coordinate. Note that the stress term is equal to the one in eq. (2.2.4) that uses a different notation.

The Monin-Obukhov similarity theory is used to describe a wind profile in the ABL under steady state and horizontally uniform conditions. The similarity regime in the viscous sublayer is governed by a dependence of roughness length on viscosity and the friction velocity, while the Monin-Obukhov equations that are responsible for producing the logarithmic profile are dependent on turbulent transport mechanisms (G L Geernaert, 1990).

In the surface layer (outside of the viscous sublayer) diabatic profiles will govern the distribution of the velocity, temperature and humidity parameters (Liu et al., 1979).

Equations (2.3.4) to (2.3.5) are valid for any conditions. However, the difference between neutral, unstable and stable conditions is only in the formulation of the stability function (ψ). These formulations (neutral, unstable and stable) for temperature and specific humidity are provided below:

$$(T - T_s)/T_* = \left[\ln\left(\frac{Z}{Z_T}\right) - \psi_T\right]/\alpha_H k \tag{2.3.4}$$

$$(Q - Q_s)/Q_* = \left[\ln\left(\frac{Z}{Z_Q}\right) - \psi_Q\right]/\alpha_E k \tag{2.3.5}$$

Where

Z is the height above the surface or appropriate plane reference

Z_T is the temperature at a height above the surface or appropriate plane reference

Z_Q is the specific humidity at a height above the surface or appropriate plane reference

$$T_* = -H/(c\rho U_*) \tag{2.3.6}$$

$$Q_* = -E/(\rho U_*) \tag{2.3.7}$$

$$\alpha_H = K_H/K_M \tag{2.3.8}$$

$$\alpha_E = K_E/K_M \tag{2.3.9}$$

And

K_M is the turbulent diffusivity of momentum

K_H is the turbulent diffusivity of heat

K_E is the turbulent diffusivity of moisture

k is the von Kármán constant

Unstable conditions are described by (As per the Businger-Dyer model) (Liu et al., 1979):

$$\psi_T = 2\ln[(1 + Y)/2] \tag{2.3.10}$$

$$\psi_Q = 2\ln[(1 + Y')/2] \tag{2.3.11}$$

Where

$$Y = (1 + a_T\zeta)^{1/2} \tag{2.3.12}$$

$$Y' = \left(1 + a_Q\zeta\right)^{1/2} \tag{2.3.13}$$

$$\zeta = z/L \tag{2.3.14}$$

ζ is the Monin Obukhov stability parameter

L is the Monin Obukhov stability length which can be estimated by:

$$L = \frac{U_*^2\theta\left[\ln\left(\frac{Z}{Z_0}\right) - \psi_m(\zeta)\right]}{\kappa^2 g(\theta_a - \theta_s)} \tag{2.3.15}$$

Where

g is gravity

θ is the mean potential temperature

θ_a is the air potential temperature

θ_s is the sea surface potential temperature

ψ_m is the Monin Obukhov similarity function for normalised velocity

Z_0 is the dynamic surface roughness

U_* is the surface wind friction velocity given by $(\tau/\rho_a)^{1/2}$

Stable conditions are described by:

$$\psi_T = -b_T\zeta \tag{2.3.16}$$

$$\psi_Q = -b_Q\zeta \tag{2.3.17}$$

Where

b_T is a constant for potential temperature

b_Q is a constant for specific humidity

The formulation of the stability function (ψ) (neutral, unstable and stable) for wind is provided below and is described as a vertical wind profile which was developed over land (Lin, Sanford, Suttles, & Valigura, 2002):

$$\frac{U_z}{U_*} = \frac{1}{k}\left[\ln\left(\frac{z}{z_0}\right) - \psi_m\left(\frac{z}{L}\right)\right] \tag{2.3.18}$$

Where

U_z is the wind speed measured at height z

In the event of L being larger than 0 the conditions can be expected to be stable and thus described by (Lin et al., 2002):

$$\psi_m\left(\frac{z}{L}\right) = -7\frac{z}{L} \tag{2.3.19}$$

In an unstable scenario (L is smaller than 0) the equation is:

$$\psi_m\left(\frac{z}{L}\right) = 2\ln\left(\frac{1+x}{2}\right) + \ln\left(\frac{1+x^2}{2}\right) - 2\tan^{-1}(x) + \frac{\pi}{2} \tag{2.3.20}$$

Where

$x = (1 - 16z/L)^{1/4}$

In order for the above equation (2.3.15) to be valid when applied in the maritime environment, micrometeorology theory requires that the ABL over the water take into

account the stationary and horizontally uniform conditions before the stress layer can be treated as a constant stress layer (Lin et al., 2002). Viscous stresses will dominate the momentum change between the air and sea surface during light wind conditions. In this instance the surface roughness (Z_0) is parameterized by

$$Z_0 = 0.11\frac{v_a}{U_*} \tag{2.3.21}$$

Where

v_a is the kinematic viscosity of air ($1.4 \cdot 10^{-5} m^2 s^{-1}$)

$U_* < 2(v_a g)^{1/3}$ calculates the speed limit for a smooth flow condition

The equations above describe the conditions in the surface layer (i.e., the ABL). They are however not valid in very close proximity to the material air-sea interface (viscous sublayer). This is due to the fact that the turbulent motion is suppressed close to the interface where molecular diffusion is expected to dominate instead of turbulence (Wesely, 1980). Most logarithmic profiles based on the micrometeorology theory only start above this layer – in the area where turbulence is dominant. In practice, for an active sea surface the concept of viscous diffusion is considered to be more theoretical and therefore not included in the calculations. Another important note is that the viscous sublayer is dependent on the friction velocity and will decrease as the friction velocity increases (Lin et al., 2002).

It is important to note that the turbulent atmospheric and oceanic boundary layers interact across an interface with waves (Lin et al., 2002). This interaction occurs through the transfer of momentum and heat (latent and sensible) and is described in term of the drag coefficient (C_D) or the aerodynamic surface roughness (Z_0). The drag coefficient is also known as the momentum transfer coefficient which is quantified as a function of wind speed over the deep oceanic areas (Wesely, 1980). The sensible heat (C_H) and water vapour (C_E) are less defined and generally considered to be equal to C_D. Velocity, temperature and humidity profiles are integrated to determine the bulk transfer coefficients. A dependence on wave age when determining the C_D and Z_0 has been shown in coastal areas or fetch-limited conditions (Lin et al., 2002). It can therefore be concluded that the C_D and Z_0 depend on wind speed. A 1997 shallow water study in Denmark also related the drag coefficients to limited fetch and found that C_D increases with wind speeds higher than 4 m/s (Vickers & Mahrt, 1998). This study highlighted the fact that wind speed only explains a small percentage of the variance in neutral drag

coefficient (C_{DN}), and that it is more dependent on wave state. Wave age also played a strong role based on the knowledge that young growing waves travel slower in relation to the wind speed, creating a steeper wave face which leads to a greater drag when compared to older waves in near-equilibrium with the wind field. In addition to wave age, some of the variance seen could be related to the breaking of larger waves during a strong onshore flow.

During neutral conditions the drag coefficient can be defined as

$$C_D = (U_*/U_{10})^2 \tag{2.3.22}$$

Where U_{10} is the wind speed at 10 m height

Eq.(2.3.22) follows directly from (2.3.3), when the wind speed at the surface (U_s) is assumed to be zero and when the friction velocity is defined as:

$$|\vec{\tau}/\rho| = U_*^2 = -\overline{u'w'} \tag{2.3.23}$$

Eq.(2.3.18) then yields the unique relationship between C_D and Z_0 as

$$C_D = [\kappa/\ln(Z/Z_0)]^2 \tag{2.3.24}$$

In general, the smooth flow condition is not satisfied (2.3.21). It is therefore more customary to express the surface roughness length by the Charnock (1955) equation, which accounts for the effects of surface waves (Lin et al., 2002):

$$Z_0 = \alpha \frac{U_*^2}{g} \tag{2.3.25}$$

Where the Charnock constant is α=0.012. The value for this constant was derived using data for the open ocean with well-developed waves and is not representative for fetch-limited areas.

With the increase in wind speed (U) the surface wind friction velocity (U_*) also increases, (2.3.22). This will in turn cause an increase in wave height, slope and energy, indicating that Z_0 could also have a strong dependence on wave state.

This dependence is evident in the relationship between Z_0, significant wave height (H_s) and wave age, which was derived for rough flow based on data from an area with fetch-limited waves in the absence of swells or mixed seas (Lin et al., 2002):

$$\frac{Z_0}{H_s} = 1.38 \times 10^{-4} \left(\frac{C_p}{U_{10}}\right)^{-2.66} \quad (2.3.26)$$

Where

C_p is the phase velocity of the waves at the spectral peak.

However, using combined datasets from three experiments the proposal that Z_0 should be parameterised by the height and wave steepness was put forward (K. Taylor & Yelland, 2000)

$$\frac{z_0}{H_s} = 1200 \left(\frac{H_s}{L_p}\right)^{-2.66} \quad (2.3.27)$$

Where L_p is the wavelength at the spectral peak.

Although the magnitude of the wind stress vector (τ) in equation (2.3.3) is related to the shorter wave slopes, the direction of the stress vector is generally aligned to the long wave propagation, with the surface roughness element contributing to the size of τ (G L Geernaert, 1990). This follows from the fact that the wind speed is proportional to the surface wind stress. Wind stress is often considered to be the momentum flux. This assumption is considered to be true if the wind vector is weak, but proves less accurate in near storm or strong sea breeze conditions. This can be expected as storm conditions, with higher wind speed, will produce a greater surface wind stress, which in turn is related to the surface roughness (2.3.24). Theory suggests that the drag coefficient is dependent on wave state, atmospheric stratification and homogeneity (G L Geernaert, 1990).

In air-sea interaction research the drag coefficient representative of a neutrally stratified and steady-state wave field is defined by the normalised drag coefficient (C_{DNW}). The subscript $_W$ symbolises the relationship between the C_{DN} and the ocean surface (waves). Generally the $_W$ will be used to describe a fully developed wind-wave spectrum in the deep ocean with a smooth surface (G L Geernaert, 1990). This accepted norm of C_{DNW} stems from the fact that surface waves in the deep ocean have very little to no friction

acting on them from the seafloor. This will cause the wave not to break, causing a smoother surface with a longer wavelength.

2.4 Summary of the Turbulence And Refraction Modelling Over the Sea (TARMOS) model

TARMOS is a micrometeorological module describing the marine surface layer, atmospheric refraction and turbulence effects, thereby providing input for a custom TDA – EOSTAR. TARMOS is therefore not only a micrometeorological model as it also evaluates optical properties such as the refractive index structure constant (C_n^2) for application in EO propagation models. The predicted vertical profiles of wind speed, temperature, humidity and various micrometeorological parameters are based on standard bulk meteorological observations (Kunz, 1996). The previous sections discussed the theory on which TARMOS is built.

A report by Kunz (1996) summarises the validation of the model. Validation was done by comparing the output to actual meteorological data and data available from literature (Kunz, 1996). The inputs required are wind speed, air temperature and humidity at the surface and a given height (usually 10 m). For the surface inputs, wind speed (U) is considered equal to 0 m/s and the relative humidity is salinity based (98.6%, or s = 0.0034). These two values are treated as constants in TARMOS, thus only the sea surface temperature (SST) is required as a variable input. Atmospheric values at the second height can all be changed by the operator. From this input, vertical profiles can be predicted. During the development of TARMOS, a verification process took place where model results were generated with wind speed values between 0 and 36 m/s, air-sea temperature difference (ASTD) defined as the air temperature directly above the sea surface and the water temperature just below between -20 and 20°C and relative humidity values of 50 to 95%. For the verification process the SST (10°C) and air pressure (1013.25 hPa) were fixed (Kunz, 1996). The conclusion from this verification exercise was that the model performed correctly.

The profiles predicted by TARMOS describe either a stable, neutral or unstable atmosphere, which is determined by the ASTD and wind speed. Simply put, when the ASTD is negative (SST is higher than the air temperature) it will predict an unstable atmospheric profile. Although this is a general rule of thumb it should be noted that the changeover between unstable and stable conditions is not exactly at ASTD = 0, as both parameters (ASTD and U) will have an impact on L (see (2.3.15) in Section 2.3). During negative ASTD conditions, mechanical mixing is enhanced by convective processes,

leading to a profile representative of a well-mixed atmosphere. During unstable conditions (over water) the atmospheric condition can be described as sunny, with high convection properties. Sub-refractive conditions with a decreased horizon range can be expected (Sub-refractive conditions will be discussed further in Section 2.6). Numerical models generally predict the propagation ranges well in unstable conditions (Bauer, 1996). With a (sufficiently) positive ASTD (air temperature is higher than the SST) the predicted profiles will be stable (G L Geernaert, 1990). Little to no turbulent mechanical mixing will be present in stable conditions leading to the development of a stratified atmosphere. Over water, a stable atmosphere is usually present during clear and calm night time conditions. This leads to super-refractive situation with an increased horizon range (almost double than in unstable conditions) and little convection (Figure 6a). Numerical model predictions do not describe or predict a stable atmosphere well (Bauer, 1996). Cloudy and windy conditions usually lead to a neutral atmosphere with some convection occurring. A fair representation of the refractive effects can be obtained by models (Bauer, 1996).

TARMOS generates the logarithmic profiles (based on micrometeorology) for (potential) temperature, (absolute) humidity and wind speed in the lower atmospheric layer, also known as the surface layer. All the parameters above (wind speed, (potential) temperature and (specific) humidity are generically referred to as X in the formulas below (Van Eijk, 2013):

$$X(z) = X_0 + \frac{X_*}{\kappa}\left[\ln\left(\frac{Z}{Z_{0X}}\right) - \psi\left(\frac{Z}{L}\right)\right] \quad (2.4.1)$$

Initially, the parameters X_*, Z_{0X}, L and ψ are unknown and an iterative solution scheme is used to resolve them. To this end, it is recognized that the three equations for U, Q and T are coupled through *L*. Within TARMOS, L is defined as [Liu et al., 1979]:

$$L = \frac{U_*^2\theta_{v0}}{g\kappa[\theta_*(1+0.608Q_0)+(0.608\theta_0Q_*)]} \quad (2.4.2)$$

where θ_v is the virtual potential temperature and all other parameters have been defined in the previous section.

The stability functions $\psi(\zeta)$ are defined as (Panofsky & Dutton, 1984) :

$\zeta \geq 0$:

$$\psi_m(\zeta) = \psi_{hq}(\zeta) = 5\zeta \tag{2.4.3}$$

$\zeta < 0$:

$$\psi_m(\zeta) = \ln[(0.5 + 0.5x^2)(0.5 + 0.5x)^2] - 2\tan^{-1}(x) + 0.5\pi \tag{2.4.4}$$

$$\psi_{hq}(\zeta) = 2\ln[0.5(1 + x)] \tag{2.4.5}$$

Where $x = \sqrt{1 - 16\zeta}$

ζ is the symbol for Z/L, stability and is dimensionless

TARMOS also provides an alternative equation for stable stratification conditions (Kondo, 1975):

$\zeta \geq 0$:

$$\psi_m(\zeta) = \psi_{hq}(\zeta) = -6\ln(1 + \zeta) \tag{2.4.6}$$

Equations 2.4.1 to 2.4.6 can be closed using a modified Charnock relation for momentum (Stuart D Smith, 1988)

$$z_{0u} = \frac{0.011U_*^2}{g} + \frac{0.11v}{(u_* + 0.01)} \tag{2.4.7}$$

Where the second term on the right hand side of the equation accounts for the viscosity effects as introduced by Businger (v = $1.461 \cdot 10^{-5}$ $m^2.s^{-1}$ as the kinematic viscosity). The factor 0.01 was introduced by Kunz (1996) to avoid singularities.

Alternatively it can be closed following the procedure outlined by Davidson et al, (1981), which exploits the relationship between X_*, X_{10}:

$$X_*^2 = C_{DX}X_{10}^2 \tag{2.4.8}$$

Values suggested for C_{DX} are $1.0 \cdot 10^{-3}$ for temperature and $1.1 \cdot 10^{-3}$ for humidity. For momentum, TARMOS includes two parameterizations for the drag coefficient C_{DX} which are both formulated in terms of wind speed U_{10}:

Open ocean (Smith, 1988): $10^3 C_D = 0.61 + 0.063U_{10}$

Coastal areas (Geernaert et al., 1986): $10^3 C_D = 0.43 + 0.100U_{10}$

The absence of a drag relation for over-land conditions in the model is one of the main reasons that the use of TARMOS is restricted to the maritime environment.

The TARMOS model uses North Sea parameterizations (pers. Comm. AMJ van Ejik, 2017), published by Geerneart, et al (1986 and 1987) for C_D as a default when it is run over shallower waters. Although wave and wind stress parameters were measured during FESTER, the determination of a False Bay specific drag coefficient is far beyond the scope of this thesis. The North Sea wave field was found to be dominated by wind waves with minimal influence from the swell energy (Gerald L. Geernaert, Katsaros, & Richter, 1986), which is similar to the False Bay environment. Given that the water depth (16 m to 20 m) and fetch distances at the study site were also comparable to conditions in the MARSEN experiment (G. Geernaert & Katsaros, 1986) the available TARMOS default settings for C_{DN} were deemed adequate for this thesis.

2.5 Measuring the lower atmosphere and upper ocean for application in air-sea research

This section will describe various experimental methods that could be applied to quantify the variables in the micrometeorological equations. These parameters include the lower atmosphere flux coefficients, atmospheric profiles, atmospheric boundary level heights and sea surface temperature (SST). It will also provide a brief history of the early experimental efforts. The section will conclude detailing some research and measurements done using tethered balloons.

Pioneering laboratory experiments to measure a wind profile over water surfaces were conducted in the late 1940 and early 1950s. The first field experiments to measure flux coefficients over the open ocean were only conducted in the mid-1950s (G L Geernaert, 1990). Wind stress and their drag coefficients were determined over small water bodies using techniques developed over land. These studies revealed a weak dependence on wind speed that was thought to be as a result of the increasing surface roughness. It was assumed that the roughness length is dependent on the wave state, which in turn is related to wind stress. This assumption of the relationship between wave state and wind stress became known as the Charnock relation (G L Geernaert, 1990), which reiterates the dependence of C_{DN} on wind speed (See equations 2.3.25 and 2.4.7).

There was renewed interest in air-sea interaction studies during the early 1960s for both theoretical and experimental expansion, which coincided with a global interest in oceanography. The mid-1960s saw the first field measurement of flux coefficients over

the open ocean (G L Geernaert, 1990). In June of 1978 the Joint Air-Sea Interaction (JASIN) experiment was conducted spanning an area of 300 km^2 in the North Atlantic (Pollard & Gu, 1978). The JASIN project aimed to observe and distinguish between the processes causing mixing in the atmospheric and oceanic boundary layers, as well as quantifying the momentum and heat budgets. The meteorological programme was designed to characterise the marine atmospheric boundary level and relate the boundary level structure to larger-scale meteorological fields. Instrumentation used included radiosonde, tethered balloons, gust probe equipped aircraft and surface measurement equipment on ships (Pollard & Gu, 1978). Measurements included direct fluxes, radiation, surface wave photos and laser altimetry. The oceanographic parameters included physical water properties (temperature, salinity and depth profiles) and vertical drifting current meters. Drifting spar buoys and wave riders were also deployed. The oceanic area of operation was considerably smaller than the atmospheric study area, due to the complexities of measuring the ocean at the time. Various other large scale experiments occurred in Barbados (Davidson, 1968), the Atlantic Ocean (Augstein, Schmidt, & Ostapoff, 1974), the Bass Strait (Dyer, 1967), and the Mediterranean during the late 1960s and early 1970s (similar to the JASIN experiment). Two important results related to the air-sea interaction studies emerged from the Barbados experiment. Firstly, profiling techniques capable of giving wind and surface stress estimates could be obtained via an aircraft. The second important piece of information highlighted the existence of a thin layer of cooler air over the ocean's surface during low wind conditions (G L Geernaert, 1990). Also during this time a close agreement between the C_{DN} and wind speed up to 26 m/s was found, as well as a clear dependence on atmospheric stratification (with relevance to temperature). No stratification was easily visible when looking at the humidity values. Another set of shallow water experiments conducted over the North Sea in 1979, the Marine Atmospheric Remote Sensing (MARSEN) experiment aimed to determine the C_{DN} applicable to the North Sea (G. Geernaert & Katsaros, 1986), as well as the wind stress estimates in order to ground truth remote sensing systems (G L Geernaert, 1990). Shallow water C_{DN} values were found to be higher than those recorded over the deep ocean.

After the detailed experiments in the 1960's and 1970's, various other experimental methods to measure surface fluxes and profiles in the lower atmosphere were developed. One such way to measure surface fluxes of momentum, heat and mass spatially and over time, was to utilise satellites. It is however essential to understand that the remote sensing techniques are not direct measurements. Environmental parameters are inferred

from the normalised backscatter power, measured by a scatterometer, and the radiative brightness provided by a passive microwave radiometer on the satellite (G L Geernaert, 1990). The above measurements are essentially the changes in reflected brightness or power (received by the satellite). Each measurement by the satellite must then be related to a meteorological or oceanographic variable theoretically in order to provide a value. In the case of the scatterometer, the slope and lengths of a surface wave will affect the backscattered power which can then be related to surface oceanic parameters (like wave height and direction). The main parameter used by the radiometer is the mean radiative temperature from the ocean surface. This can be related to the SST, atmospheric temperature and waves (G L Geernaert, 1990). Numeric model functions are used in these cases to relate the relevant information to environmental parameters using only one measured value, not taking into account the influence that could be exerted by the atmosphere or the sea surface.

Methods used to infer flux profiles can largely be grouped into three (budget, local covariance and Monin-Obukhov similarity methods) and will be discussed briefly below (S. D. Smith, Fairall, Geernaert, & Hasse, 1996):

Budget methods

The Wind Set-up method is based on the balance between the imposed wind stress and the pressure exerted on the surface of a shallow water body (G L Geernaert, 1990). It equates the tilt of the water surface to that of the surface wind stress vector (S. D. Smith et al., 1996). This method however proved to be unreliable and produced errors due to the effect of horizontal water density gradients and tidal induced tilts. Drag coefficient values rendered by this method were also found to be larger than values provided by the other techniques (G L Geernaert, 1990).

When the spatial distribution of the wind stresses and drag coefficients are required in the ABL, the vorticity and mass budget method can be used. This method uses a spatial array of ships' weather stations, and *in-situ* radiosonde information to perform a mass budget analysis that will provide the mean vertical velocity above the boundary layer (G L Geernaert, 1990). Error sources in this method include thermal wind calculations and uncertainties in the pressure field and upper boundary conditions, especially in deep convection conditions (S. D. Smith et al., 1996).

Estimates of the drag coefficients extent during hurricanes are provided by employing the Ageostrophic method (G L Geernaert, 1990), which is based on the assumption that there is a transfer of angular momentum during the storm to the ocean, which will be evident in the cross-isobaric flow. Plainly stated this method relies on the wind vector differing from the pressure gradient (S. D. Smith et al., 1996), and is most reliable at wind speeds greater than 25 m/s.

Local covariance methods

The most accurate method in determining fluxes is the Eddy-Correlation Technique, which looks at the covariance between the fluctuating vertical, horizontal and lateral velocities (G L Geernaert, 1990) and are calculated using the equation below.

$$\bar{\tau} = -\rho[\langle u'w'\rangle\hat{\imath} + \langle v'w'\rangle\hat{\jmath}] \tag{2.5.1}$$

Where u, v and w represent the horizontal and vertical wind components respectively

The angle between the stress vector (from 2.5.1) and the mean wind flow is described by:

$$\gamma = \tan^{-1}(\langle v'w'\rangle/\langle u'w'\rangle) \tag{2.5.2}$$

This is done for the momentum flux, sensible heat flux (air temperature) and the latent heat flux (specific humidity). A drawback of this technique is the complexity in measuring the fluctuations of specific humidity over short time periods and on an operational basis. All components can however be measured, which is advantageous. When using this technique to determine fluxes, it should be noted that the measurements must be done on a stable platform.

Monin-Obuhov similarity methods

A simple and popular method to calculate fluxes is the 'Profile Method' (G L Geernaert, 1990), which uses an array of vertically spaced anemometers with intervals that are ideally spaced to coincide with log *z*. This method has proved successful for near-neutral stratifications, but becomes less accurate in conditions that deviate from neutral stratifications. Another major disadvantage is that the mean and turbulent wind fields will cause variations of the logarithmic profile when measured near the ocean surface, especially when there are long, rolling waves present. It is also not very useful in measuring temperature or humidity values, thus rendering mostly drag coefficients.

An alternative method to the Eddy-Correlation Technique that does not require a stable platform is the Dissipation Technique (G L Geernaert, 1990). This technique can be

deployed on ships or buoys as it only requires turbulence information in the higher frequencies. It usually utilises a hot film anemometer with a sensitive voltage response to wind speed. Turbulent kinetic energy equations are used to determine the drag coefficients and wind stress values. The steady condition turbulent kinetic energy equation is provided below:

$$U_*^3 \phi_M / kZ = g/T_v < w'T'_v > -\epsilon - I \quad (2.5.3)$$

Where

ϵ is the dissipation rate

ϕ_M dimensionless wind shear

I is the imbalance term which is described by

$$I = \frac{\partial}{\partial z}[\rho^{-1} < w'p' > + < w'e >] \quad (2.5.4)$$

Where

e is fluctuating turbulence kinetic energy

The imbalance term was found to be small during near neutral and unstable conditions and therefore (2.5.3) can be re-written as:

$$U_*^3 = kZ(\epsilon + I)/\phi_e \quad (2.5.5)$$

Where

$$\phi_M = \phi_e + Z/L \quad (2.5.6)$$

ϕ_e is dimensionless turbulence kinetic energy

It was found that the dissipation and eddy-correlation techniques render similar flux values in near neutral and high wind conditions, when measurements occurred on stable platforms.

Other important parameters in determining atmospheric profiles with micrometeorology theory are SST and ASTD. Traditionally a radiometer is used to measure the SST in any air/sea interaction studies. However, when using microwave (MW) or Infra-Red (IR) sensors (i.e. radiometers) it should be noted that it only measures the sea skin layer with a thickness less than a millimetre. In remote sensing (satellite) applications the MW or IR data are generally calibrated using *in-situ* sensors which actually provide water temperatures more representative of the oceanic surface layer. This layer can vary in depth from mere centimetres to several meters below the ocean surface (Cimini et al., 2003). In Section 4.2 of this thesis the actual skin temperature and that of the surface layer water column (at 0.5 m below the surface) will be presented (as part of the vertical

profile discussions) to illustrate the difference that can be seen between these measurements.

In the study by Cimini et al [2003], the goal was to use a scanning radiometer (SR) technique to measure both oceanic and atmospheric oxygen and carbon dioxide emissions (in a wavelength band that displays relatively high atmospheric attenuation) simultaneously. In the 1999 experiment, two vertically scanning radiometers were used in order to provide continuous boundary level air temperature profiles as well as an accurate ASTD (Cimini et al., 2003).

The upward looking instrument provided air temperature gradients with respect to the surface air temperature. When this measurement was calibrated with a high quality temperature sensor, profiles up to 500 m were possible. The system consisted of one radiometer operating in the MW band and the other in the IR spectral region. A high quality air temperature sensor was used to calibrate the measurements. The microwave scanning radiometer (MWSR) measured the natural emission of oxygen in the atmospheric absorption band as opposed to carbon dioxide measured by the infra-red scanning radiometer (IRSR). The MWSR had an atmospheric optical depth of approximately 300 m and a water penetration depth of 300 µm compared to the IRSR atmospheric optical depth of 150 m and water penetration of 3 µm.

During the experiment the instrumentation was placed on a boom (10 m above sea level) that extended 5 m beyond the vessel's hull. The variable scan rate on both scanning radiometers was 0.55 Hz and completed one scan every 1.8 s. A variation of linear statistical inversion techniques were used to estimate air temperature profiles from the atmospheric radiation observations. In order to calculate the ASTD a physical (as opposed to statistical) inversion method was used. During analysis it was found that foam on the sea surface complicated the recovery of data especially in the MW band and that analysis was limited to days with low wind conditions (lower than 8 – 9 m/s). This wind speed is believed to be the threshold for the creation of breaking waves in the open ocean, and as foam emits as a blackbody in the MW region measurements of the water skin layer were tainted. It was therefore also noted that the performance of the system can be improved if it was moved to the bow of the vessel, allowing the radiometers to scan over undisturbed and foam-free water. However, even with the drawbacks highlighted above, the results still achieved an accuracy of 0.3 K for the air temperature profiles up to 500 m and 0.28 K for the ASTD during the day. At night the accuracy was 0.15 K and 0.11 K,

respectively. This experiment showed that accurate, simultaneous estimates of the ASTD and air temperature profiles is achievable by using two scanning radiometers (Cimini et al., 2003).

In order to interpret remote sensing measurements linked to global atmospheric and oceanographic models, it is essential to simultaneously measure the mass, momentum and energy fluxes (Graber et al., 2000). Thus, with the growing need to understand the coupling of the atmosphere and ocean and the effect of wave dynamics on this, it became necessary to relook at the way in which high-resolution flux and wave measurements were conducted in the oceanic environment. One limitation was that the directional wave properties, largely responsible for these fluxes, were derived from surface-following moored buoys, which only provided a coarse directional resolution. Other shortcomings of these buoys were that they generally cannot resolve waves smaller than their own dimensions (typically between 1 and 10 m) and that they disturb the surface. Considering that many aspects of air-sea interaction and remote sensing are governed by meter to centimetre long waves, these buoys proved to be inadequate (Graber et al., 2000). In an attempt to optimise for the directional wave information, a buoy system was developed that was capable of high-resolution measurements.

This Air-Sea Interaction Spar (ASIS) buoy was developed and built to not only record high-resolution wave parameters, but also the atmospheric fluxes associated with the ocean-atmosphere coupling. The ASIS buoy could be used as a free-drifting or tethered platform. The instruments included on this platform recorded motion, waves, wind and other atmospheric parameters. The motion sensors (inertial package) resolved the wave and turbulence measurements in relation to the buoy movement and were placed at 6 m water depth on the base of the buoy. This package consisted of three orthogonal force balance servo accelerometers, three solid state Systron Donner Gyrochip angular rate gyros and a compass. A GILL sonic anemometer was deployed on top of the 4 m mast (total height above sea level 2.5 m), together with four cup anemometers at 1.5, 2.3, 3.4 and 5.1 m above the mean water level. Wind direction was measured using a vane at 2.4 m above the mean sea level. The wet- and dry-bulb temperatures were recorded using Campbell scientific probes at 1.6, 2.3, 3.6 and 4.9 m, providing temperature and humidity profiles (0 – 5 m above mean sea level). A pressure (Vaisala), rain gauge and radiometers were also installed. The SST was recorded at 1 m below the water surface. Wave data were recorded using eight capacitance wires approximately 2.5 m long. The ASIS buoy was tested on two occasions, where it demonstrated its seaworthiness in winds over 18

m/s and seas with 3 m significant wave heights. The trials confirmed that the ASIS buoy was a good general purpose platform for air-sea interaction studies, capable of rendering wind profiles, wave measurements and momentum fluxes of high quality in the open ocean (Graber et al., 2000).

Progress was also made towards the measurement of atmospheric vertical profiles. In 2000 two lifting platform systems were compared (Muschinski et al., 2001), and even though the data measured do not hold direct relation to this thesis, the comparison between the lifting platforms has added value. This study evaluated the use of tethered balloons or kites to that of aircrafts. The payload for the kite or balloon system included a basic Vaisala RS-80 radiosonde which transmitted real-time measurements of pressure, air temperature and humidity at a frequency of 7 seconds. Additional sensors were attached to record wind speed and direction, solar radiation and the pitch and roll angles. Payload weights were between 5 and 10 kg. The second lifting system consisted of a helicopter-borne payload (called the HELIPOD and weighing 250 kg) that deployed pressure, temperature, velocity vector and humidity sensors. As this system is mobile, it had additional navigational equipment including a Global Positioning System (GPS) receiver, inertial navigation system (INS) and a radio altimeter (for accurate height measurement). When comparing the two systems the major differences were in weight and cost. The balloon or kite lifting system was relatively cheap to operate, but had a very limited lifting weight (in most cases depending on the size of the balloon, less than 10 kg). It was also limited in heights that could be obtained. The HELIPOD in contrast was much heavier and could in theory carry many more sensors. It was also possible to operate this system in worse meteorological conditions and operating heights could be increased to several kilometres above ground. It is also possible to easily change altitudes and fly the sensor package diagonally across the mean wind direction, whilst covering a much larger area in a shorter time. Drawbacks include high cost, positioning, limited ability for true vertical profiling and the impossibility to measure simultaneously at different altitudes. Flow distortion effects introduced by the aircraft must also be accounted for.

A Helikite system very similar to the one deployed during the FESTER experiment was used in at least two other studies. The first was a study conducted at Heron Reef in Australia where a tethered balloon system was used as a first attempt to determine the heat budget of coral reefs (MacKellar et al., 2013). This study used an eddy covariance unit mounted on a pontoon which consisted of a sonic anemometer, a net radiometer, air temperature and relative humidity sensors. All these sensors were mounted 2.2 m above

the water level. Water temperature was provided by sensor manufactured by HOBO. The lower tropospheric measurements were done using a tethered sonde and a Kestrel 4500 weather monitor. These instruments were lifted using a tethered kite (in higher wind speeds) and a Helikite in lower wind speeds. The Helikite reached heights of 200 m with the tethered kite reaching up to 600 m. This study provided valuable insights into the capabilities of the two systems to provide direct measurements of the air-sea energy fluxes for the calculation of heat budgets (MacKellar et al., 2013).

The second Helikite study was conducted in 2011 over False Bay, South Africa (the FESTER study area), where the Council for Scientific and Industrial Research (CSIR) used a 11 m^3 Helikite capable of lifting 5.5 kg to examine the effect of the atmosphere on electromagnetic wave propagation (Naicker, Anderson, Le Roux, & Alhuwaimel, 2011). Atmospheric parameters including temperature, pressure and relative humidity were measured using the iMet-2-AB radiosonde. Data were collected every second and were used to calculate the vertical refractivity profile. Although the Helikite proved useful in obtaining the meteorological parameters (for use in the calculations), no explicit analyses were made of these profiles.

2.6 Basic introduction to atmospheric effects on Electro-optic sensing.

The second objective of the experimental work on which this thesis is based, i.e., a comparison between the actual measured profile of the lower atmosphere (up to 200 m) and the prediction of this profile by micrometeorological bulk parameterisations, pertains to the understanding of electro-optic (EO) transmission across False Bay. This understanding of EO transmission is dependent on three parameters: the radiation source, the sensing equipment used and the atmosphere. This section aims to first provide a basic introduction of the electromagnetic (EM) spectrum and then describe the atmospheric effects.

Electro-optical sensing systems exploit the electromagnetic spectrum for detecting objects and can be defined as a group of systems capable of converting photons to electrons (Gunter, 2010). These systems operate in the wavelength region of 0.2 to 14 µm (ultraviolet to Long wavelength Infrared (LWIR)) (Figure 4). This electro-optical domain is a part of the electromagnetic (EM) spectrum, which includes amongst others radio waves, X-rays and sunlight (Gunter, 2010). EM radiation propagates through space as transverse waves at the speed of light and differs only in wavelength or wave frequency.

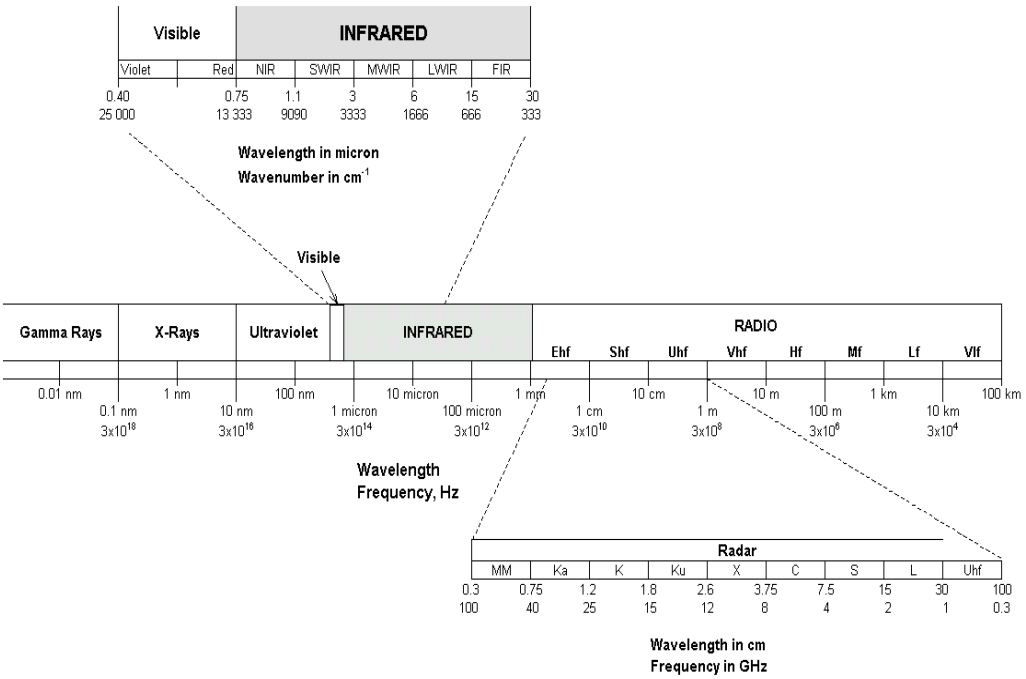

Figure 4: Electromagnetic Spectrum (Gunter, 2010)

The atmosphere acts as a filter on EO sensing equipment which will limit the sensor's performance in observing a target by decreasing the radiant power, reducing the contrast, changing the spectral structure and reducing the resolution of the image (Farmer, 2001). These filter effects on EO imaging are a result of various sources. Absorption and scatter by gases, aerosols, dust and precipitation will cause radiometric attenuation. The refractive (optical) turbulence and change in aerosols, dust and precipitation concentrations cause variations in irradiance. Image resolution reduction is mainly due to the refractive turbulence distortion and larger atmospheric particles whereas contrast reduction is caused by background radiation scattering and absorption in the path between the sensor and the object. Thus, in EO terms the transmission losses, which describe the reduced radiance (or brightness) that is received from a target are mainly due to absorption and scattering which decreases the signal-to-noise ratio (target versus background signal) (Kunz, 1996).

Absorption and scattering are mostly related to atmospheric elements and compounds, essentially what the atmosphere consists of chemically. Of these elements or compounds, water vapour, carbon dioxide, nitrous oxide, carbon monoxide and ozone can be considered the major absorbers and scatterers (Driggers, Cox, & Edwards, 1999). Scattering is predominantly a result of photons and atmospheric particles colliding (thereby changing the direction of the incident radiation), whereas absorption describes

the process of atmospheric molecules extracting energy from the photons (thereby removing the photons from the EM field). Optical turbulence in turn is mostly related to the structural variations of the atmosphere (temperature, pressure and density).

The change in flux, when describing the effects of scattering and absorption (grouped together called extinction) on transmission through the atmosphere, can be described by the following equations (Driggers et al., 1999):

$$d\Phi = -\sigma\Phi dx \tag{2.6.1}$$

Where

dx is the infinitesimal distance

Φ is the incident radiation

σ is the extinction coefficient (made up from two components: absorption coefficient (a) and scattering coefficient (γ)

Equation (2.6.1) can be adapted to (6.2.2) to provide the attenuation over an infinite distance trough a homogenous medium:

$$\Phi = \Phi_0 e^{-\sigma x} = \Phi_0 \tau \tag{2.6.2}$$

Where:

$\tau = e^{-\sigma x}$ is the transmittance of the atmosphere over distance x. This relation is known as the Beer-Lambert law, which, considering the extinction's coefficient's dependence on wavelength can be written as:

$$\tau(\lambda) = e^{-\sigma(\lambda)x} \tag{2.6.3}$$

During the absorption process, the molecule absorbs the energy of the incident photon, which then leads to a temperature change (Driggers et al., 1999). Absorption can only take place when the energy difference between electronic states in the molecule amounts to a specific value, given by Einstein's equation (2.6.4). Hence, the specific composition of the molecule determines which frequencies can be absorbed

$$E = hv \tag{2.6.4}$$

Where

E is the energy of the photon

h is Planck's constant (6.626 X 10-14 J-sec)

v is the frequency of the incident light

During the process of scattering the radiant energy stays the same, but the propagation direction is redistributed. Scattering is grouped in three categories based on the ratio of the particle size and wavelength of the incoming beam (Driggers et al., 1999). Rayleigh scattering occurs when particles have a radius less than 1/10 of the incident beam's wavelength. Considering typical EO wavelengths of the order of a micron, Rayleigh scattering is thus most prominent for nanosized particles and/or molecules. When the particles are approximately the same size as the incident's beam wavelength the scattering process must be described by Mie (or aerosol) scattering. The last category of scattering, geometric optics, will occur when the particles are much larger than the incoming beam wavelength, e.g., raindrops.

A simplified equation for the light attenuation caused by Rayleigh scattering is below (Driggers et al., 1999) with the Rayleigh scattering coefficient γ given by:

$$\gamma = \gamma_r N \tag{2.6.5}$$

Where N is the molecular number density and the Rayleigh scattering cross-section γ_r is given:

$$\gamma_r = \frac{8\pi^3 (n^2 - 1)^2}{3N^2 \lambda^4} \tag{2.6.6}$$

Where n is the refraction index.

Mie scattering is obtained from a complex equation derived from the Maxwell equations that includes refractive index, particle size and the incident and scattering angles. Geometric optics is described by Snell's law (Roychoudhuri & Pedrotti, 2009) and is visually represented in Figure 5.

$$\frac{\sin i}{\sin r} = \frac{n_r}{n_i} \tag{2.6.7}$$

Where

i is the angle of incidence

r is the angle of refraction

n_i is the index in the incident medium

n_r is the index in the refracting medium

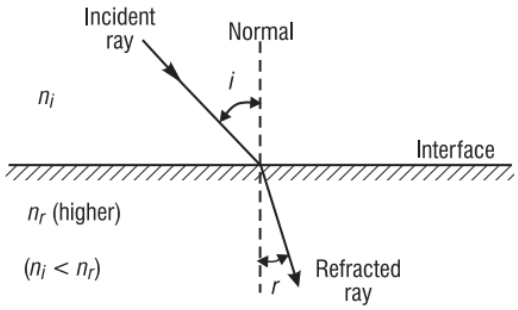

Figure 5: Snell's Law geometry (Roychoudhuri & Pedrotti, 2009)

Propagating electromagnetic radiation may not always follow a straight trajectory through the atmosphere. This "bending of rays" is called refraction and arises from the presence of refraction index gradients in the atmosphere (Gunter, 2010). The atmospheric refractive index (n) is typically 1.00029 in air (Bauer, 1996), but exhibits small variations as a result of variations in air temperature and humidity values in the atmosphere. The refractive index is generally larger near the earth's surface. Since Snell's law predicts that a ray will bend in the direction of the higher index, this will therefore cause light, which is travelling in the horizontal plane, to be bend 'downwards', giving the impression that it is following the curvature of the earth's surface (Gunter, 2010). This is called super-refraction and visualized in Figure 6a. However, positive refraction gradients also occur, and cause light rays to bend upwards – this is called sub-refraction (Figure 6b).

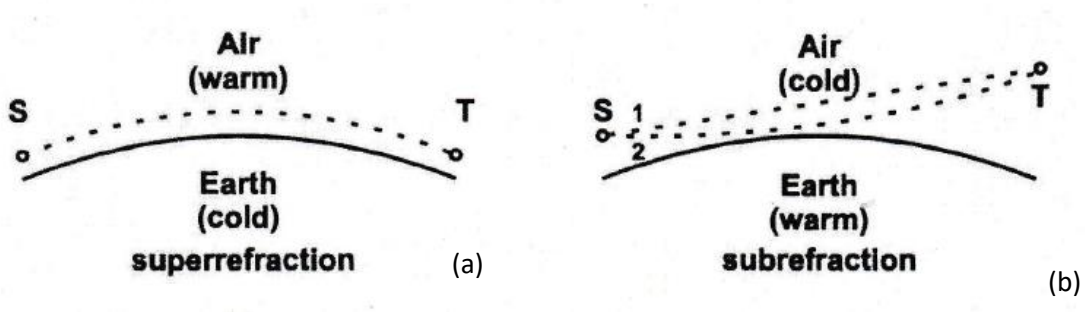

Figure 6: Schematic showing super and sub refraction (Gunter, 2010)

EO sensors operate over an atmospheric optical path that typically ranges more than 10 km (Bauer, 1996), with the ASTD determining the refractive conditions over water. In summary, in unstable atmospheric conditions, the density at higher altitudes is large due to the temperature decrease that occurs with height. This higher density will cause the light rays to bend up, which in turn will reduce the visual range (Bauer, 1996). During stable conditions the light rays will be bend down increasing the visual range. This is due to the high altitude density being relatively small.

CHAPTER 3: MATERIALS AND METHODS

An extensive experiment took place in False Bay, South Africa (Figure 7) called the 'First European – South African Transmission ExpeRiment (FESTER) from April 2015 to February 2016. Multiple parameters related to the atmosphere, ocean and electro-optic sensor performance were measured during this time. The location for the FESTER experiment was mainly chosen for its convenience and access to various structures where sensors and measuring equipment could be deployed.

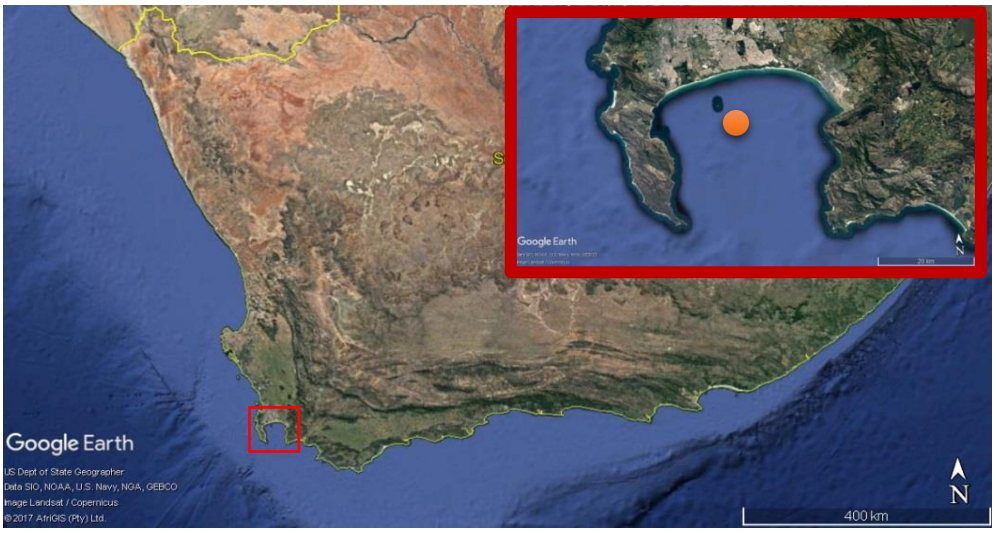

Figure 7: Location of the FESTER experiment in False Bay South Africa

The FESTER experiment was hosted by the Institute of Maritime Technology (IMT) located in Simon's Town at the shores of False Bay. A general climatological description of this area is provided in Section 3.1. FESTER mainly sought to provide data (environmental and sensor specific) for the validation of a particular TDA, i.e., EOSTAR (A.M.J. van Eijk, M.A.C. Degache, D.J. de Lange, 2010). There were also four secondary objectives. The first objective was the measuring of EO dynamic signatures and wakes in order to aid the development and testing of ships' signature models. The second objective looked at the general characterisation of the atmospheric and oceanic environment. Thirdly, the spatial and temporal scales of environmental differences over the transmission path (i.e. meteorological parameters, aerosol concentrations, and turbulence) were assessed. The final secondary objective was to compare the propagation conditions for the electro-optical and radiofrequency domains in the study area.

In order to achieve the above mentioned goals the experiment was broken into two components consisting of continuous measurements and intensive observation periods (IOP).

The continuous measurements aimed to provide a 12 month dataset that characterized the False Bay environment. Measurements included meteorological and oceanographic parameters as well as EO propagation parameters (Van Eijk et al., 2016) .

Each IOP was approximately 2 weeks long and the individual IOP's were spaced over the year to capture the seasonal variability in the area of interest. Dates for the IOP's were 1 to 14 June 2015 (IOP 1), 31 August to 13 September 2015 (IOP 2), 16 to 29 November 2015 (IOP 3), and 15 to 26 February 2016 (IOP4).

During the IOPs various sensor systems were deployed to evaluate their performance as a function of the environmental conditions (Eisele et al., 2016). The vessel Sealab1 was used as a target, and this information from the target (Sealab1) and the different sensor packages provided the core data for the primary objective of FESTER. Data for the secondary objective of understanding the dynamic aspects of EO signatures was also addressed during the IOP's. Environmental characterization was increased during the IOPs highlighting the spatial and temporal differences that occur in the atmosphere and ocean. The intensified environmental characterisation efforts, including the Helikite measurements that are a focal element of this thesis, were timed to coincide with the various high-value EO sensor packages that were made available during the IOP periods.

The environmental data discussed in this thesis focus on the air-sea interface as well as the lower atmosphere (0 – 200m). These data were primarily obtained along a 6.5 km long path, which started in front of the IMT building (34°11.28'S and 18°26.82'E) and ended in the vicinity of St James (34°07.74'S and 18°27.30'E). This path is denoted as the SJ line. ASTD measurements were continuous along the SJ line (made from Sealab1), with the vertical profile station (see section 3.2 below) situated in the middle (Figure 8, right panel) at 34°09.84'S and 18°27.12'E.

Figure 8: FESTER trial area. Left panel: Detailed area, IMT is indicated by the red circle, RR=Roman Rock, SJ=St James, SF=Strandfontein, LR=Long radial. Arrows indicate generic boat tracks. Right panel: Detailed area, showing the positions where oceanographic and atmospheric parameters were measured during the trial (CM: Current Meter; CTD: Conductivity Temperature Depth).

During the IOP's the water column was also sampled and characterised using a Conductivity Temperature Depth (CTD) profiler. These CTD stations were equally spaced along the SJ line with the first station (CTD 1) in front of IMT. The vertical profiling (Helikite profile) and wave measurements were made near the mid-way point, in the vicinity of CTD 3 (Figure 8 right panel). CTD 5 was the oceanographic station closest to St-James.

The collection of environment data served a two-fold purpose. Part of the data could be used as input for sensor performance models or modules, while another part of the data served to verify if the models yield the proper solution. The two main objectives of this thesis relate to these purposes. The deployment of the Helikite and other sensors on board SeaLab1 would allow characterization of the air-sea environment and atmospheric profiles. These profiles can be compared to those predicted by the micrometeorological module TARMOS (cf. section 2.4) on the basis of near-surface input parameters. This then would provide insight into the performance of TARMOS.

Thus, in order to address both objectives of this thesis, a Helikite balloon with an integrated sensor package was designed and used to measure the vertical atmospheric conditions from sea level to a height of approximately 200 m. The sensor package used here provides air pressure, relative humidity, air temperature and wind speed, extending the possibilities of the scanning radiometers (cf. chapter 2 (Shaw et al., 2001) and (Cimini et al., 2003)). In addition, the SST was measured using two methods. A radiometer was deployed, which measured only the skin temperature of the ocean surface. Skin SST is a very thin layer of approximately 10 µm (Talley, Pickard, Emery, & Swift, 2011). The second method used a 'Windsurfer' to measure the bulk SST at 0.5 m below the sea surface and the air temperature directly above it

(0.5 m) simultaneously. This bulk SST measurement is usually referred to as the 'bucket' temperature and is generally available as an input to the micrometeorology models (Wesely, 1980). It is accepted to be the bulk temperature from a few centimetres to 1 m below the surface, and some bulk micrometeorology models will apply a correction to this value in order to evaluate the sensible heat momentum transfer coefficient (C_H) (Wesely, 1980). This method was experimental and produced interesting results when compared to the more conventional method of using a radiometer, discussed below in Chapter 4. The Helikite vertical profiling capability and air-sea interface measuring system are described in detail below.

Additional oceanographic and meteorological parameters were measured in the vicinity for the duration of the FESTER experiment (March 2015 – February 2016). This included time-series wave and meteorological parameters. The wave properties were measured at the vertical profiling station (Figure 8) and the meteorological parameters at Roman Rock Lighthouse, 2 km East from IMT. These additional parameters will be described in Section 3.5.

3.1 General climatological description of the study area – False Bay

False Bay, situated south of Cape Town, is considered to be South Africa's largest natural bay, and covers an area of 1082 km^2 (Wainman, 2000). Simon's Bay, where the bulk of the FESTER data collection occurred, including the vertical air profiles that are principal to this thesis, can be found in the north-western corner of False Bay (Figure 7 – insert). Due to Simons Bay's location it is generally grouped and classified as south-west coast in the South African context. This grouping is mainly attributed to the local weather patterns and oceanic setting. The area is characterized by warm, dry south-easterly winds in summer and north-westerly winds in winter. False Bay also falls within a winter rainfall region with impressive north-westerly storms where gale force winds are known to occur. Cold nutrient rich water from the southern Benguela system can enter False Bay and also Simon's Bay on occasion during the summer months (Wainman, 2000). The seawater temperatures in the region display south and west coast trends. West coast seawater temperatures are largely influenced by upwelling, where temperatures range from 9 – 14°C which can increase to 16°C or higher through sun warming. Oceanic waters in this area have temperatures that can reach up to 20°C. The south coast of South Africa however exhibits temperatures of 20 – 21°C during summer and 16 – 17°C during winter. The water column in the western False Bay is characterized according to spatial and temporal variations and it was found that significant thermal stratification occurs during summer (Wainman, 2000). Case studies in the naval harbour of Simon's Town, close to the FESTER study area, showed that temperatures in the oceanic surface layer (upper 2 m)

were on average 1.2°C higher than those in the FESTER region. Surface temperatures between 13°C and 21.8° were recorded during a 12 year monitoring programme in the naval harbour (Gildenhuys, S. and Wainman, 2012).

3.2 Vertical atmospheric profiling: Helikite and meteorological sensor package

A Helikite – Skyhook 3.0 m with a helium capacity of 3 m^3 was used as the main lifting mechanism for the sensor packages. The Skyhook 3.0 can lift a maximum load of 1.5 kg in the absence of wind (Appendix A). This maximum load was the main limitation in the design of the sensor package. As the aim of this capability was to measure vertical air profiles at sea, the limiting factor in choosing the size of the Helikte (and therefore the load) was deck space on the IMT Workboat Sealab1.

An Airmar PB200 weather station was initially chosen as the main meteorological sensor, primarily due its compact size (circumference: 72 mm; height: 130 mm and weight: 285 g) and because it can calculate true wind speed and direction on a moving platform. The Airmar has an in-built Global Positioning System (GPS), compass and accelerometer in addition to the standard meteorological sensors (i.e., wind speed and wind direction, temperature and pressure). These improvements in technology, since the 2000 study (cf. chapter 2.5) (Muschinski et al., 2001), where one sensor (Airmar) incorporated both the meteorological as well as the motion sensors advanced the use of tethered balloons in the profiling of the lower atmosphere. The altitude data used in the analysis were retrieved from the Airmar's on-board GPS.

The Airmar however had three major shortcomings specifically for the vertical profiling application: (1) The Airmar air pressure sensor was not able to cope with the sudden changes in altitude, and the recorded data did not show the expected drop in pressure as the altitude increased. Thus, a KESTREL 4500 was attached to the Helikite. This pressure sensor provided a better representation of the air pressure. (2) The Airmar sensor was not fitted with a humidity sensor resulting in the use of the humidity sensor on the KESTREL 4500 weather station. Finally (3), the air temperature sensor's resolution and accuracy were not sensitive enough for the application (EO propagation). The Airmar has an accuracy of ± 1°C (Appendix B) with a resolution of 0.1°C. In the case of verifying the TARMOS model that is heavily reliant on the ASTD, an accuracy of 0.5 °C is required. Ideally, the accuracy should be closer to ±0.2°C (pers. Comm. AMJ van Eijk, 2015). In order to increase the accuracy of the temperature measurements, a LM35 air and water temperature sensor was incorporated as part of the package. The LM35 has a typical

accuracy of ±0.2°C (Appendix B) for the temperature range expected (-10 to 25°C). The LM35 was tested against a series of temperatures using a temperature bath located at IMT (F100 thermometer). The comparison clearly shows that the LM35 was performing within the acceptable accuracy range of ±0.2°C (Table 1).

Table 1: Calibration check results for the Helikite LM35 sensor

Sensor	LM35 Temperature	F100 Temperature	Difference
LM35_1	5.11	5.14	-0.03
LM35_1	10.21	10.24	-0.03
LM35_1	15.32	15.20	0.12
LM35_1	21.44	21.47	-0.03
LM35_1	24.96	24.98	-0.02
LM35_1	29.91	29.92	-0.01

The final payload of the Helikite consisted of the Airmar and LM35, both connected to a SEEEDUINO Stalker data logger that was housed in a water-tight container together with a rechargeable battery (Figure 9).

Table 2 summarises the different sensor accuracies and resolutions that were used during the analyses of the data. For a full list of specifications on the above instruments, please see Appendix B.

Table 2: Summary of the instrumentation specification and accuracy.

Atmospheric Parameter	Instrument used	Accuracy
Air Temperature	LM35 air and water sensor	± 0.2°C
Wind Speed	Airmar PB 200	Low winds: 1 knot + 10% of the reading High winds: 2 knots or 5% of the RMS whichever is greater
Relative Humidity	Kestrel 4500	± 3%
Altitude (GPS)	Airmar PB 200	Not available
Air pressure	Kestrel 4500	± 1.5 mbar

During the deployment of the Helikite, air temperature measurements recorded with the LM35 sensor were compared to air temperature measurements recorded using a Vaisala WXT520 scientific weather station. The Vaisala was mounted on the Sealab1 (Figure 13) at approximately 6 m above sea level. This check showed that the LM35 sensor agreed better with the Vaisala on the descending profile after it had time to stabilise. The air temperature measured by the LM35 was approximately 0.53°C higher than measured by

the Vaisala for three of the four profiles. The profile measured on 20150907 was the outlier, and the LM3 air temperature recorded was 0.28°C lower than that of the Vaisala.

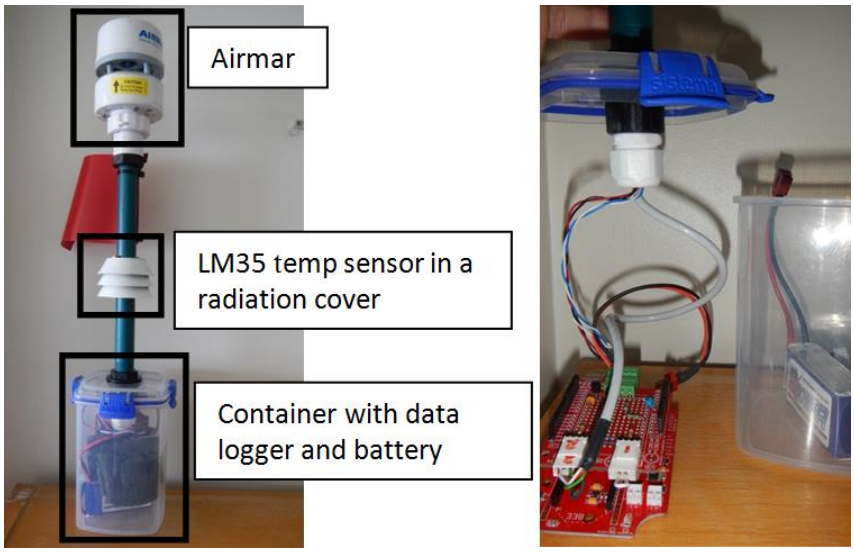

Figure 9: (a) The meteorological sensor package. (b) Data logger attached to the lid of a water tight container

3.3 Air/Sea interaction and SST measuring system.

a. Conventional measuring technique: Heitronics KT15.85IIP Radiometer

A long wavelength infrared (LWIR) radiometer was used on-board Sealab1 to measure the SST. The radiometer operates in a highly transparent atmospheric window, i.e. 9.6 to 11.5 µm thermal IR band (Gunter, 2017) chosen to minimize the impact of water vapour present in the atmosphere (Gunter, 2014). The sensor has a Field Of View (FOV) of approximately 2.6°. With the LWIR radiometer mounted 1.5 m above the sea surface, a surface spot with a diameter of about 6 cm could be imaged (Gunter, 2017).

In 2014, the Heitronics radiometer was tested using an accurate and stable blackbody source (HGH HCH1000) to verify the accuracy (Gunter, 2014) before the commencement of the FESTER experiment in 2015. This accuracy/stability measurement was conducted for an hour involving an indoor measurement set-up. The radiometer was placed at a range of 1.5 m from the blackbody which was set to emit a temperature of 15.0°C (representative of the expected sea temperature). The results from the accuracy calibration are shown in Figure 10 below (Gunter, 2014).

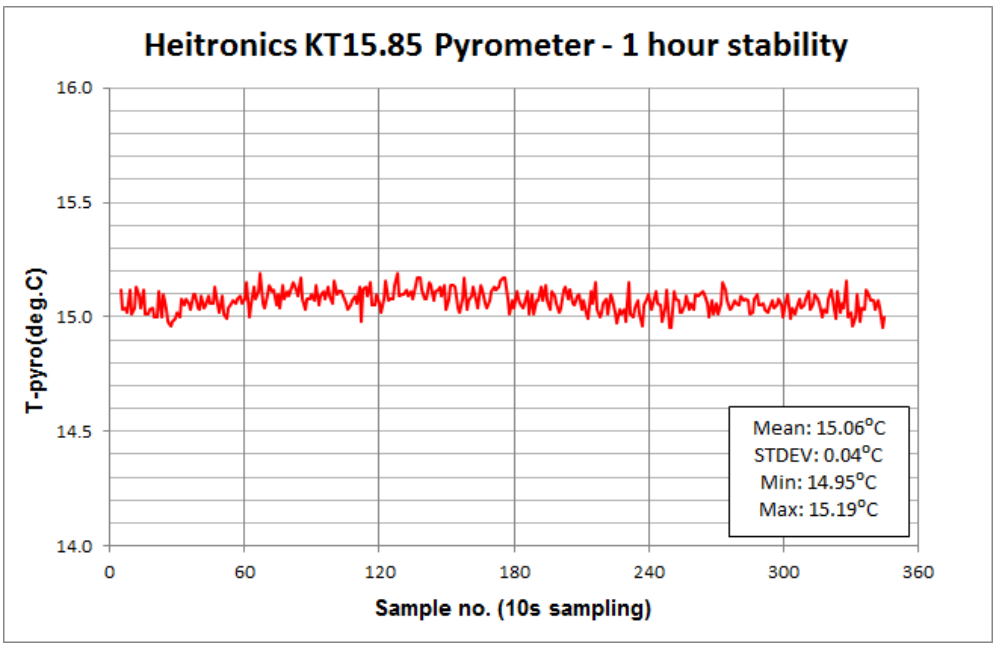

Figure 10: Heitronics KT15.85 Radiometer 1-hour stability (Gunter, 2014).

During FESTER, a calibration check similar to the one described above was conducted before and after each IOP to demonstrate that no significant thermal drift had occurred over a 2 hour period (Gunter, 2017). These checks also confirmed that the uncertainty in the LWIR measured SST for an integration time of 10 seconds was approximately 0.2°C, as shown in Figure 10. It can therefore be stated that the uncertainty for clear sky conditions was 0.2°C for the SST. Taking also into account the above-mentioned uncertainty of 0.2°C in the determination of SST, it is estimated that the uncertainty in the determination of the ASTD was 0.3°C (Gunter, 2017). In overcast conditions the SST uncertainty could increase by a maximum of 0.4°C as no compensation was done for sky reflections during cloudy conditions.

b. Experimental measuring system: 'Surfboard' with in-house developed sensor package

A standard windsurfer board (Figure 11) was fitted with a sensor package using PVC piping. The surfboard sensor package consisted of two LM35 temperature sensors, one in a radiation cover for measuring air temperature 0.5 m above the sea surface and one 0.5 m below the sea surface. Initially only one LM35 sensor was going to be used on the surfboard to measure the water temperature. This sensor was compared to a scientifically calibrated F100 thermometer in a temperature bath for a temperature range from 5°C to 30°C (LM35_2 in Table 3). When the second sensor to

measure air temperature was added a single temperature comparison at 15°C was done (LM35_3 in Table 3). Both sensors performed within the acceptable accuracy range of ±0.2°C.

Table 3: Temperature check for the surfboard LM35 sensors

Sensor	LM35 Temperature	F100 Temperature	Difference
LM35_2	5.12	5.14	-0.02
LM35_2	10.22	10.24	-0.02
LM35_2	15.20	15.19	0.01
LM35_3	15.18	15.18	0.00
LM35_2	21.52	21.47	0.05
LM35_2	25.02	24.98	0.04
LM35_2	29.96	29.92	0.04

The SEEEDUINO Stalker data logger and battery were placed in a watertight container (Figure 12). For full specifications see Appendix B

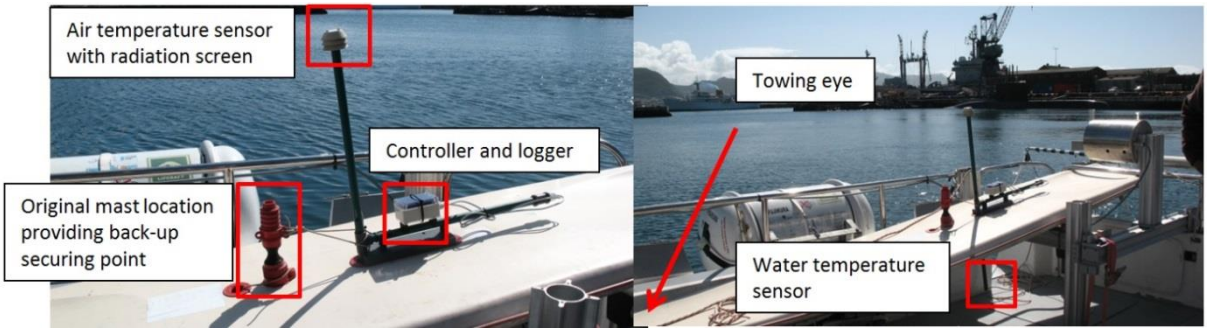

Figure 11: The Surfboard with sensor package installed on the Sealab1 ready for deployment

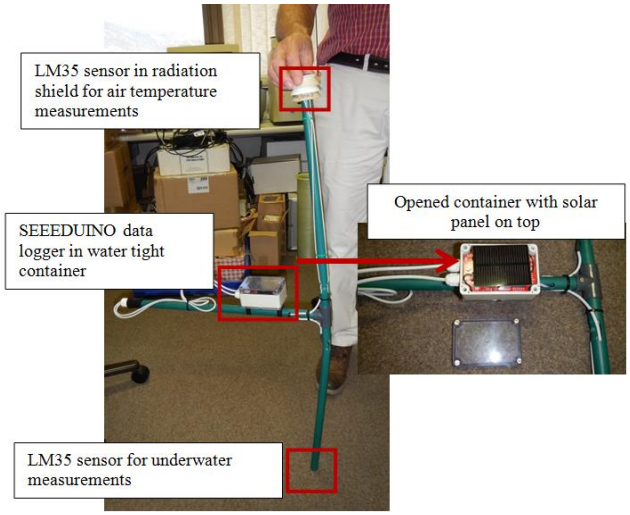

Figure 12: The Surfboard sensor package

3.4 Basic operation of the ASTD and Helikite systems

The LWIR radiometer was mounted on a pole extending the sensor out in front of the Sealab1's bow by about 1.5 m (Figure 13) in order to sample 'undisturbed' surface temperatures (Gunter, 2017). The sensor was positioned perpendicular to the sea surface. The logging interval was set at a period of 10 s. With an integration time of 10 s the average spot area of 6 cm (diameter) was recorded along a 50 m line if the boat was sailing at 10 knots (Gunter, 2017). For the type of infra-red sensor involved, the temperature resolution improves with a longer integration time (according to the specification the temperature resolution improves from 0.4°C to 0.15°C when the integration time increases from 1 s to 10 s). Data were logged on a laptop using a serial link (RS232). The laptop time was synchronised with the on-board GPS-receiver recording the Sealab1's position every second (Gunter, 2014).

Figure 13: Instrumentation deployed on Sealab1: Radiometer deployed in-front (1), Vaisala automatic weather station (2) and Airmar automatic weather station (3)

At the starting point of the SJ line (in-front of IMT – CTD 1), the 'surfboard' was deployed over the stern and towed to the side of the Sealab1. Care was taken to tow it outside the wake of the boat, at a maximum speed of 5 knots (Figure 14).

Figure 14: The Surfboard towed alongside Sealab1

Continuous measurements were taken over the length of the transect IMT – SJ in order to record the ASTD and characterise the inhomogeneous nature of the propagation path. The CTD profiles and vertical profile were only taken on the way back from the St James station, at the stations specified above (Figure 8). During the vertical profiling (at station CTD 3) the 'surfboard' was left drifting next to the Sealab1 in order to record the ASTD.

At the profiling station, the Helikite was secured to the winch, and handled with care during the launching and retrieval phase (Figure 15). Once clear of the deck it was left to ascend in 50 m intervals using a marked cable, whilst judging the tension on the cable to determine the maximum height. In low wind conditions 250 m of cable was let out. In stronger conditions, the strain on both the cable and the winch was significantly more, thus less cable was deployed (between 100 and 200 m). Wind speed was the limiting factor in the operation of the Helikite and all profiling was stopped if the wind speed exceeded 10 m/s due to the difficulty in controlling the Helikite close to the deck.

Figure 15: (Left) The meteorological sensor package attached to the Helikite. (Right) Helikite with sensors launched off the back of Sealab1

The Helikite took approximately 30 minutes to reach its maximum height which was dependent on the atmospheric conditions at the time. In higher wind speeds, the drag on the control line was more and it pushed the kite down which led to lower altitudes reached during the profile. Highest altitudes were reached on calm days with virtually no drag on the line.

Data presented in this thesis were collected during IOP2 and IOP4 on the dates summarised below (Table 4).

Table 4: Summary of the air profile data collected during the experiment

IOP	Date	Vertical profile time	Max line out	Max height reached	General weather/sea conditions
2	2015/09/01	14:39 start 15:32 end	200 m	125 m	SE wind direction
2	2015/09/07	12:27 start 13:20 end	200 m	158 m	NW wind direction Overcast (60% sky coverage) Rain during part of the profile
2	2015/09/08	15:10 start 16:08 end	200 m	150 m	Weak NW wind direction
2	2015/09/10	12:21 start 13:21 end	250 m	244 m	Variable wind direction Rain started on the down profile
4	2016/02/24	08:29 start 09:32 end	250 m	209 m	Calm conditions Morning measurements

3.5 Air profiling and air/sea interaction data processing and analysis

Data from both the Helikite system and the surfboard were downloaded and analysed using MS Excel and MATLAB. Data from the Helikite and Surfboard were recorded in 1 s intervals. The Kestrel recorded at a rate of 4 s. Thus, before any analysis could take place the relevant datasets (Table 2) were aligned according to GPS time and only the records corresponding to the Kestrel (every 4 s) were extracted for the altitude, wind speed and air temperature data. As the Helikite ascended at less than a meter in the 4 s timeframe the data every 4 s were considered to be representative of the atmospheric conditions in that pocket of atmosphere, and averaging the values would not have made a difference in the model output. The data were also separated into ascending and descending profiles. These profiles were plotted together, which revealed whether or not the atmospheric state had changed during the approximately 30 minutes it took to complete the ascending and descending leg. When the data close to the sea surface for the ascending and descending profile was compared to the Vaisala WXT520 scientific weather station on-board Sealab1, it was apparent that the Helikite sensor package took some time to

stabilise. This was especially true for the air temperature sensor. For this reason the decision was made to use the descending profile for analysis in this thesis. However, both the ascending and descending profiles are presented.

Surfboard data were extracted to coincide with the descending profile. These values were averaged and used as the SST input (T_{sea}) for the TARMOS model. Only the water temperature measurement was used.

Data analysis of the radiometer involved alignment of the SST measurement with the spatial position of the Sealab1, which was accomplished using the GPS time stamp. Once a time-stamp was obtained, the SST values were extracted between CTD station 4 and CTD station 3 in order to ensure that the radiometer measurements were collected over an undisturbed sea surface. It is noted that the SST-values obtained from the radiometer correspond to a different spatial area and a different timeframe than the Helikite data. Values obtained during the profile measurements were not used as the vessel was drifting and that could have caused some surface mixing. The values selected were then averaged to give one value that was used as an alternative SST input for TARMOS (T_{Sea}).

The TARMOS model was executed three times per vertical profile. The first two model runs used the actual meteorological values (p, U, Q, T) measured by the Helikite at a height of 10 m as starting parameters. The reason for using the 10 m values in this study was to comply with the accepted norm used in most bulk micrometeorology prediction models (G L Geernaert, 1990) in order to deal with the rapid increase in wind speed directly above the ocean surface. These two model runs use different SST input values. The first TARMOS model run (denoted as "Modelled (SST)") was initialized using the radiometer SST, while the second TARMOS model run (Modelled (-0.5)) was initialized with the 'Surfboard' data SST, which was 0.5 m below the sea surface. The third TARMOS model run (Modelled (*m) was initialized with the 'skin' SST (radiometer) value and the 'lowest' recorded Helikite values for air temperature, wind speed, air pressure and relative humidity (i.e., below 10 m). The vertical profiles resulting from these model runs were plotted against the 'ACTUAL' ascending ($Actual_u$) and descending ($Actual_d$) profiles as measured by the Helikite (using the sensors / parameters summarised in Table 2). This was done in order to compare the predicted output from bulk micrometeorological models using the 'skin' SST (radiometer) and the 'bucket' SST (surfboard).

On 2016/02/24 (Profile during IOP4) a radiosonde was available and the opportunity to attach it to the Helikite for comparison purposes arose. Unfortunately no surfboard or radiometer data were recorded during this Helikite deployment. This profile and the data it produced were therefore analysed differently and the focus was placed on comparing the values recorded by the Helikite sensor package with those of the radiosonde. In order to obtain TARMOS predictions, for comparison to the Helikite and radiosonde profiles, a SST value was retrieved from the MODIS satellite. This SST value was measured at 12:30 in the afternoon, whereas the profile was recorded at 08:30 in the morning, so this could have had an effect on the TARMOS predictions and must be considered with the results. In this case TARMOS was run twice. The first predicted profile used the Helikite data at 10 m altitude (Modelled (heli)). The second TARMOS prediction (Modelled (sonde)) used the radiosonde data at 23 m, which was the first recorded value. Both predicted TARMOS profiles used the satellite SST as an input value.

3.6 Additional environmental information

Weather and wave data to describe the general conditions during the vertical profiles were extracted from 2015/08/30 to 2015/09/12 (IOP2). Hourly data are used and are presented in the results below (Section 4).Water column data were collected during IOP2 and will be used to augment the SST data from the Surfboard and radiometer. No additional environmental information will be discussed for the profile on 2016/02/24 (IOP4) as the focus was on the comparison of different sensor packages.

a. Time-series meteorological data

Two automatic weather stations were deployed on Roman Rock Lighthouse (RRL) during the study period: Airmar 200WX and a German customized package including a Gill HS-50 ultrasonic anemometer. Data from the Airmar were used in this study for comparative purposes as it has the same specification as the Airmar PB200 used as part of the vertical profiling sensor package.

The Airmar was situated on a 6 m pole fastened to the safety railing on RRL. The weather station is approximately 16 m above sea level and protrudes 2 m above the lighthouse roof. The pole is secured with 2 stays to reduce vibration.

The data for air temperature, relative humidity, wind speed, wind direction and air pressure were plotted using MATLAB to provide an overview of the general conditions

prior, during and shortly after the vertical profiles. Relevant information is discussed in section 4.1a.

b. Wave measurements

A NORTEK Acoustic Waves and Currents (AWAC) meter was deployed at the mid-point of the SJ-line (Figure 8) in the position where the vertical profile was recorded. The AWAC provides a current profile and wave measurements. The time series of wave height, period and direction are presented in section 4.1b of this report as background information. There is, however, more directional and detailed measurements available that could be used in the future to characterise the wave spectra in more detail and to determine a C_D parameterisation for False Bay. That analysis is beyond the scope of this thesis. The AWAC was set-up to record current information every 20 minutes and waves every hour.

The wave data was plotted using MATLAB to provide an overview of the general conditions prior, during and shortly after the vertical profile, and is further discussed in section 4.1b.

c. Water column properties

During IOP2 a SeaBird SBE19 profiler was used to provide vertical water profiles for temperature, salinity, dissolved oxygen and turbidity. These profiles where recorded along the SJ-line at CTD stations 1 – 5 (Figure 8). A summary of the CTD stations with the relevant data collected is available in Table 5.

Table 5: The CTD station positions and times taken (CTD3 highlighted blue was done during the helikite profile)

CTD Station	Date	Time	Lat DD S	Long DD E	Additional remarks
CTD5	01/09/2015	13H47	34.129	18.455	Convergent zone noticed during dip
CTD4	01/09/2015	14H14	34.146	18.451	
CTD3 (Profile 1)	01/09/2015	14H42	34.160	18.446	
CTD2	01/09/2015	15H48	34.175	18.448	
CTD1	01/09/2015	16H05	34.188	18.447	
CTD5	07/09/2015	11H53	34.130	18.456	Did not hit bottom due to drifting
CTD4	07/09/2015	12H11	34.147	18.452	Did not hit bottom due to drifting
CTD3 (Profile 2)	07/09/2015	12H46	34.164	18.452	Did not hit bottom due to drifting
CTD2	07/09/2015	13H38	34.174	18.451	Rain
CTD1	07/09/2015	13H55	34.187	18.448	
CTD5	08/09/2015	13H46	34.130	18.456	fuel contamination on surface
CTD4	08/09/2015	14H42	34.146	18.452	
CTD3 (Profile 3)	08/09/2015	14H54	34.162	18.450	
CTD2	08/09/2015	16H18	34.175	18.450	did not hit bottom due to drifting
CTD1	08/09/2015	16H30	34.187	18.449	
CTD5	10/09/2015	11H36	34.130	18.455	overcast
CTD4	10/09/2015	12H39	34.146	18.451	overcast
CTD3 (Profile 4)	10/09/2015	12H08	34.162	18.448	overcast
CTD2	10/09/2015	12H39	34.175	18.449	overcast/rain, mist
CTD1	10/09/2015	13H55	34.187	18.448	

The data from the five stations (CTD 1 – CTD 5) were processed using the Ocean Data View (ODV) programme to plot an interpolated view of the water column across the SJ-line. These plots were useful in describing at the water column properties (temperature and salinity) and in determining the surface mixed layer depth and will be reported on in Section 4.2.

CHAPTER 4: RESULTS

In this chapter we will present the results of the five Helikite deployments reported in Table 4. To appreciate the general meteorological and oceanographic conditions during which the deployments took place, the first section of this chapter discusses the supporting weather, wave and water measurements. This allows us to relate the Helikite data to this framework.

4.1 Time series results during the sampling period

a. Meteorological conditions

The meteorological conditions for IOP2 were extracted from 31 August to 12 September 2015. This timeframe included the week where air profiles were measured using the Helikite. The values for wind speed and direction, air temperature and air pressure were plotted using MATLAB to provide a look at the general atmospheric conditions during this time. The Figures (16 – 18) below show data for the period 31 Augustus to 12 September 2015 in subplot (a). Subplots (b) to (d) represent subsections of the data presented in (a) for each of the vertical profiling events during IOP2.

Wind conditions – IOP2

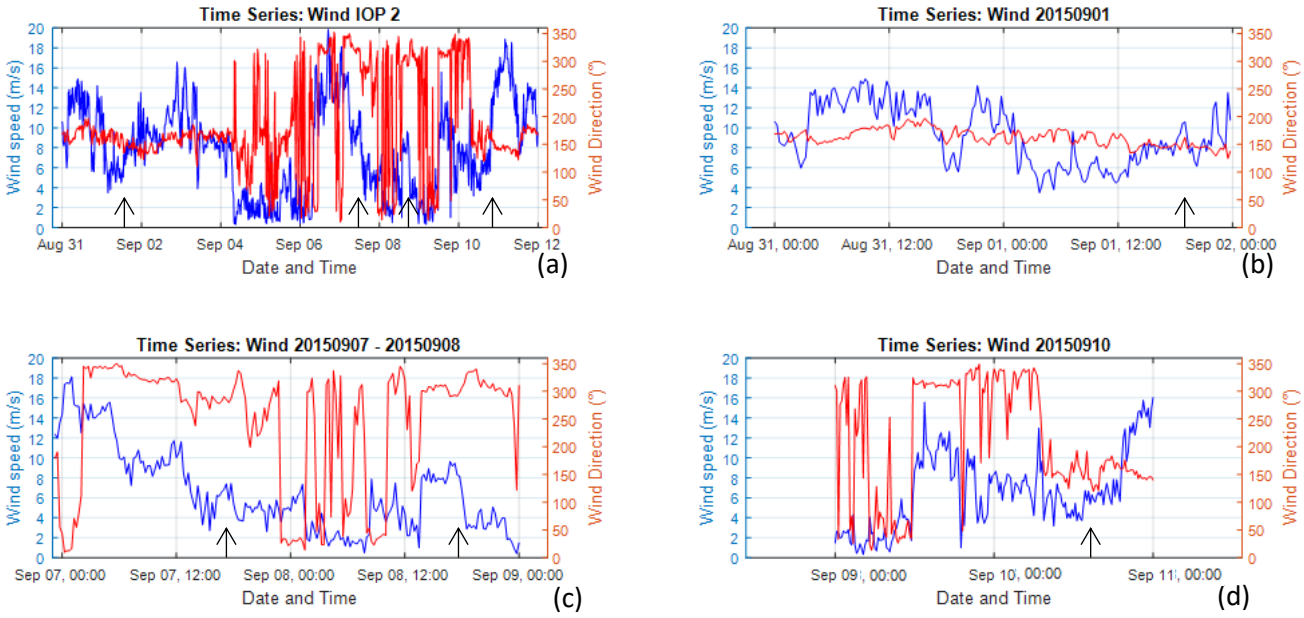

Figure 16: General background wind speed (blue line) and direction (red line) measurements for IOP2 during the time of taking the vertical profiles. Black arrows show when the air profiles were measured

During IOP2, the wind speed ranged between 0.5 and 18 m/s (Fig 16a) with the direction showing the two dominant wind conditions in False Bay: Southeast (SE) (Fig 16b) and Northwest (NW) (Fig 16c and d). Strongest speeds (18 – 20 m/s) were recorded on 6 and 7 September during the NW conditions.

On 2015/09/01 (Profile 1) the wind direction was mainly in the S to SE sector (150° – 180°) which is representative of one of False Bay's dominant wind conditions. A strong SE (12 – 14 m/s) was recorded on the day prior to the Helikite profile, dropping slightly during the time of profiling. Wind speed for this time ranged between 4 and 11 m/s with an average speed of 8 m/s during Profile 1 (Fig 16b).

Conditions on 2015/09/07 (Profile 2) and 2015/09/08 (Profile 3) represented the other dominant wind condition in False Bay namely NW. Profile 2 was taken when the wind was mainly from the NW (270° to 300°), with Profile 3 displaying a stronger northerly component (25° to 325°). Near-gale conditions (16 – 18 m/s) were recorded in the early hours of 2015/09/07, dropping significantly to 6 – 8 m/s during the time of Profile 2. This downward trend continued and Profile 3 was recorded in a weak NW (2 – 4 m/s) as is shown in Figure 16 (c).

Profile 4 (2015/09/10) was obtained in variable wind conditions. The wind direction varied and directions from NNW through to SSW were observed. The wind speed decreased from 13 m/s in the early morning to 6 – 8 m/s during the profile (Fig 16d).

Air Temperature – IOP2

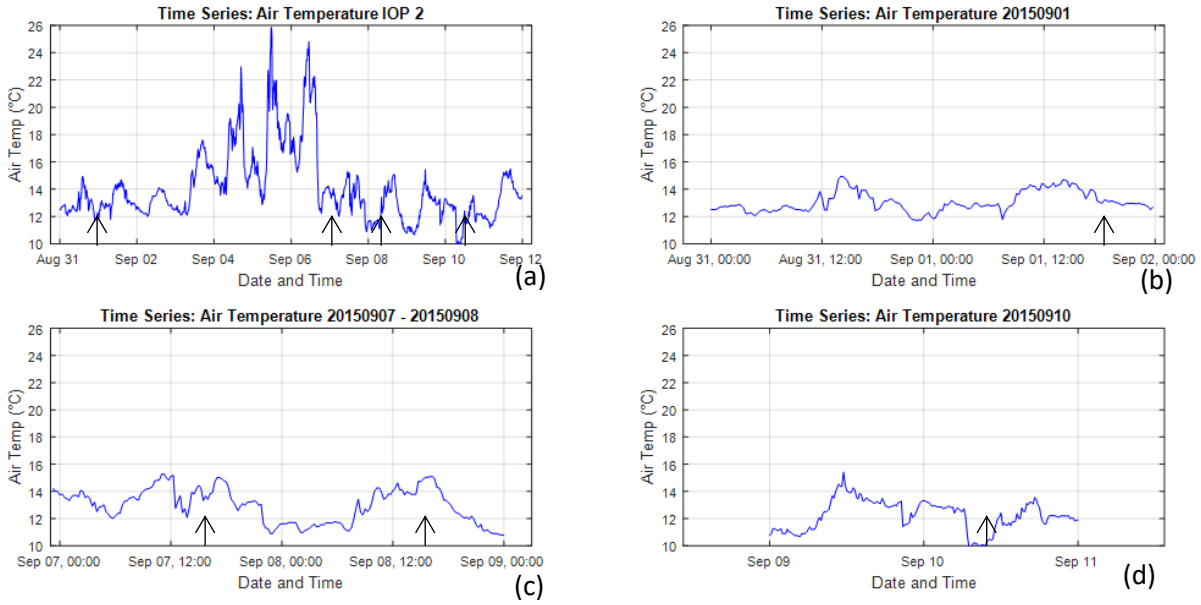

Figure 17: General background air temperature measurements for IOP2 during the time of taking the vertical profiles. Black arrows show when the air profiles were measured

Air temperatures during IOP2 varied and ranged between 10 and 26°C (Fig 17a). Highest temperatures (22 – 26°C) were recorded between 4 and 7 September, and considerable overnight cooling occurred (10 – 13°C).

Three of the four Helikite profiles (Profile 1, 2 and 4) recorded during IOP2 were taken during air temperatures of 12 – 14°C (Figure 17 (b), (c) and (d)). Profile 3 (Fig 17c, afternoon of 8 Sep) was recorded in a slightly higher temperature range (14 – 16°C).

Air Pressure – IOP2

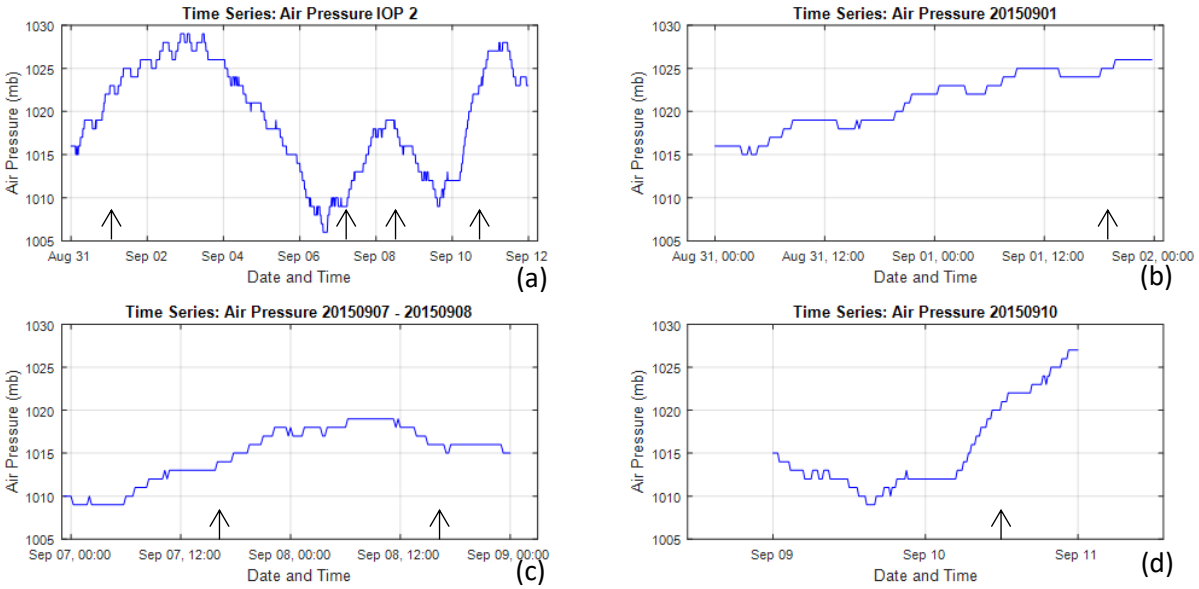

Figure 18: General background air pressure measurements for IOP2 during the time of taking the vertical profiles. Black arrows show when the air profiles were measured

Air pressure during IOP2 ranged between 1005 and 1030 mb (Fig 18a). Higher air pressures (1020 – 1030 mb) were recorded between 2 and 5 September, with pressures less than 1020 between 6 and 9 September.

Profile 1 (2015/09/01) was recorded during a period where the air pressure was rising from approximately 1020 to 1025 mb (Fig 18b). An air pressure of approximately 1014 mb was recorded during Profile 2 and 1016 mb (Profile 3) as is shown in Figure 18 (c). The last profile for IOP2 (Fig 18d) was recorded at a slightly higher pressure (1020 mb).

b. Wave conditions

Wave conditions for IOP2 were also extracted from 31 August to 12 September 2015. The vertical air profiles measured using the Helikite fell within this time frame. All values were plotted using MATLAB to provide a look at the general wave conditions during this time. Figures 19 and 20 show data for the period 31 Augustus to 12 September 2015 in subplot (a). Subplots (b) to (d) represent subsections of the data presented in (a) for each of the vertical profiling events during IOP2.

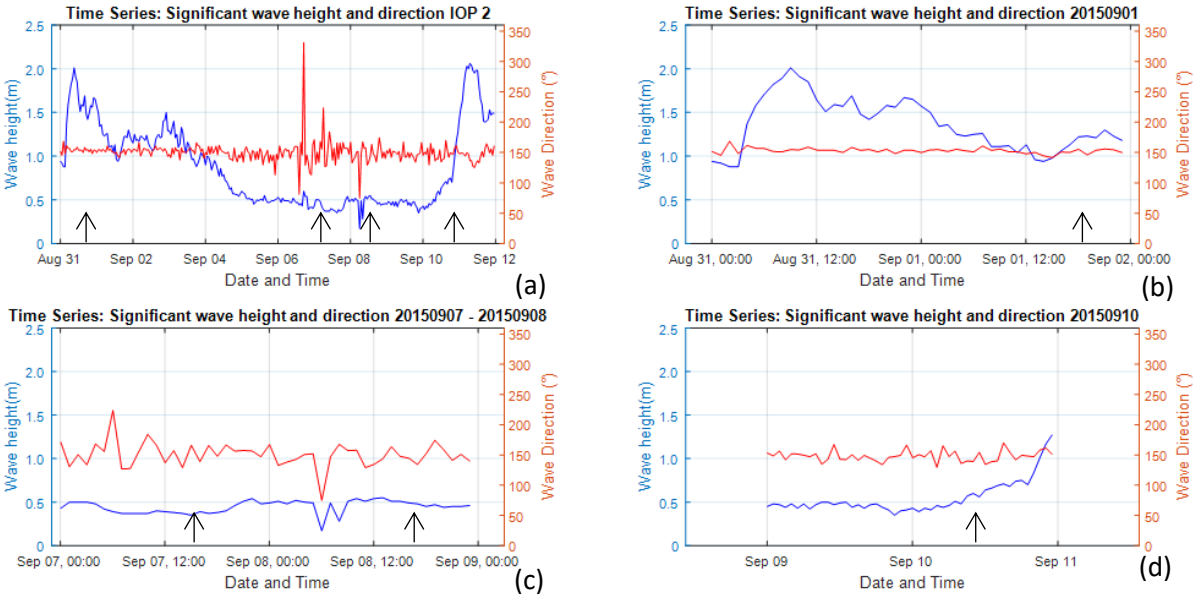

Figure 19: General background wave height (blue line) and direction (red line) for IOP2 during the time of taking the vertical profiles. Black arrows show when the air profiles were measured

The highest waves recorded during IOP2 were 2 m (Figure 19a), dropping to 1 m during the time of Profile 1. Between 4 and 10 September 2015, the wave height remained stable at approximately 0.5 m after which it increased to 2 m again. The wave direction was predominantly from the SSE (150°) for the relevant period in IOP2. Some variation occurred between 6 and 8 September 2015 when the direction ranged between 90° and 200°.

On 2015/09/01 (Profile 1) the maximum height was 1 m coming from the SSE (150°) with no variation in the direction for a day before and after the recorded Helikite profile (Figure 19b). Both profiles 2 and 3 were obtained during a time when the wave height was less than 0.5 m. The direction was alternating between SSW (210°) and SE (130°) during Profile 2. Direction for Profile 3 was predominantly from the S (150° - 180°). During Profile 4 (2015/09/10) the maximum wave height was 0.5 m with a direction of 150° (Fig 19d).

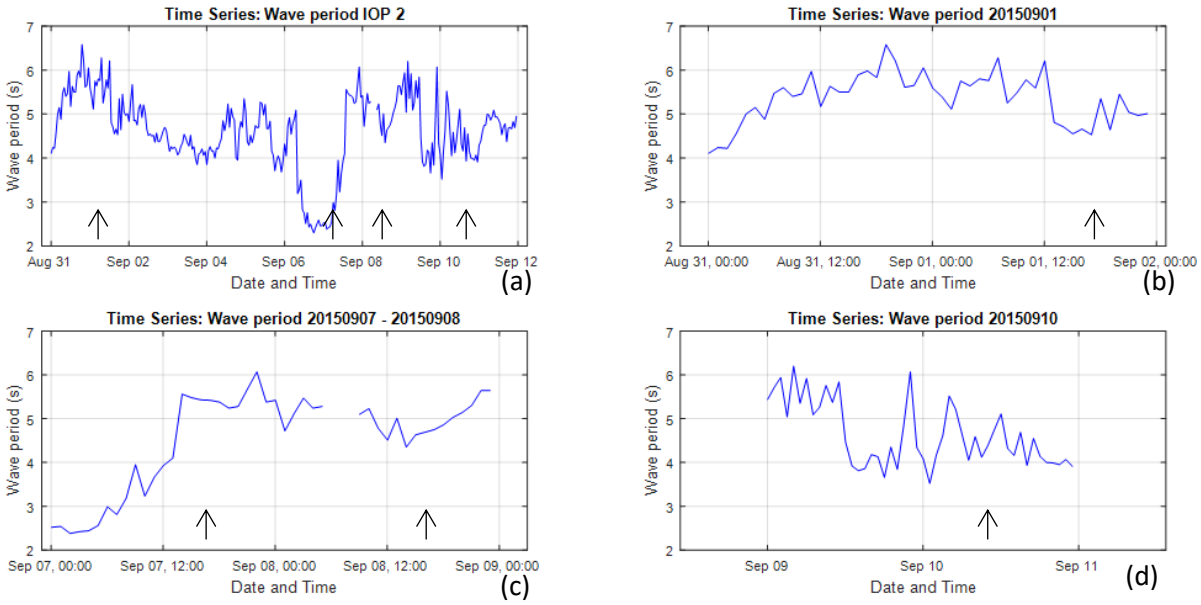

Figure 20: General background wave period for IOP2 during the time of taking the vertical profiles. Black arrows show when the air profiles were measured

The wave period was predominantly between 4 s and 7 s between 31 August and 12 September. Periods below 3 s were recorded for a short time on the 6th and 7th (Figure 20a).

During Profile 1 the period was between 5 and 6 s (Figure 20b). The period increase from 4 – 6 s at the time of Profile 2, where it remained for the next two days (including Profile 3). The period for the last Profile during IOP2 was between 4 s and 5 s (Figure 20d).

c. Water temperature properties

The water temperature profiles are included in this section as they were recorded at the same time as the Helikite vertical profiles. The water column structure, especially in relation to the depth of the ocean surface mixed layer could be of particular interest when compared with the air characteristics directly above the sea surface. Figures 21, 22, 23 and 24 show the water temperature structure for the transect on the SJ-line. The 5 CTD stations was plotted and interpolated using the ODV programme. The black arrow on each image shows the position where the vertical profile was taken (CTD 3). The temperature profile insert is the single plot for CTD 3.

2015/09/01 (Profile 1)

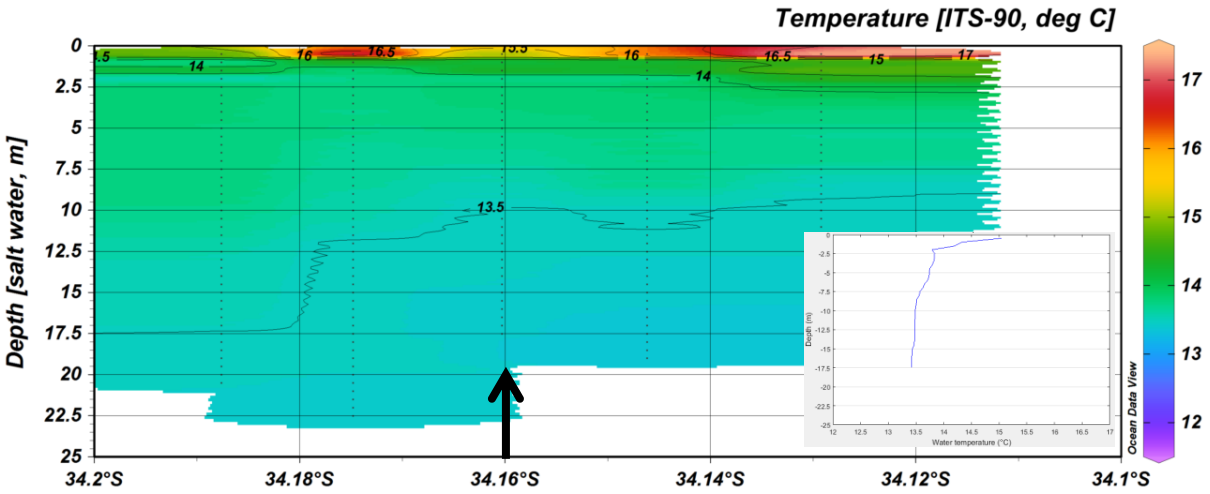

Figure 21: Water column temperature values for Profile 1 along the SJ-line (Schlitzer, 2019)

A shallow thermocline (above 2.5 m below the sea surface) was present during the time that Profile 1 was recorded (Figure 21). Temperatures in this layer were between 15.5°C and 17°C. The water column below this shallow thermocline up to a depth of 7.5 m was well mixed with temperatures between 13.5°C and 14.0°C. Bottom water (below 7.5 m) cooled slightly to below 13.5°C. Two areas with higher temperatures (16 – 17°C) are present on either side of the profile site. Water temperature recorded by CTD 3 in the upper 1 m (Figure 21, inset) was between 15°C and 16°C. This does not compare well with the values measured by the surfboard (13.8°C) and radiometer (12.37°). The water column at the time of Profile 1 was more complex than the other profiles, which is discussed in Chapter 5 (pg. 85 – 86). Thus, the discrepancy seen between the CTD and other measurements could be a result of the different instrumentation and their respective settling times. The CTD also takes an average over a much longer time period in the surface layers (i.e. 2 minutes), where the vessel could have drifted from the cooler areas into one of the warmer pockets.

2015/09/07 (Profile 2)

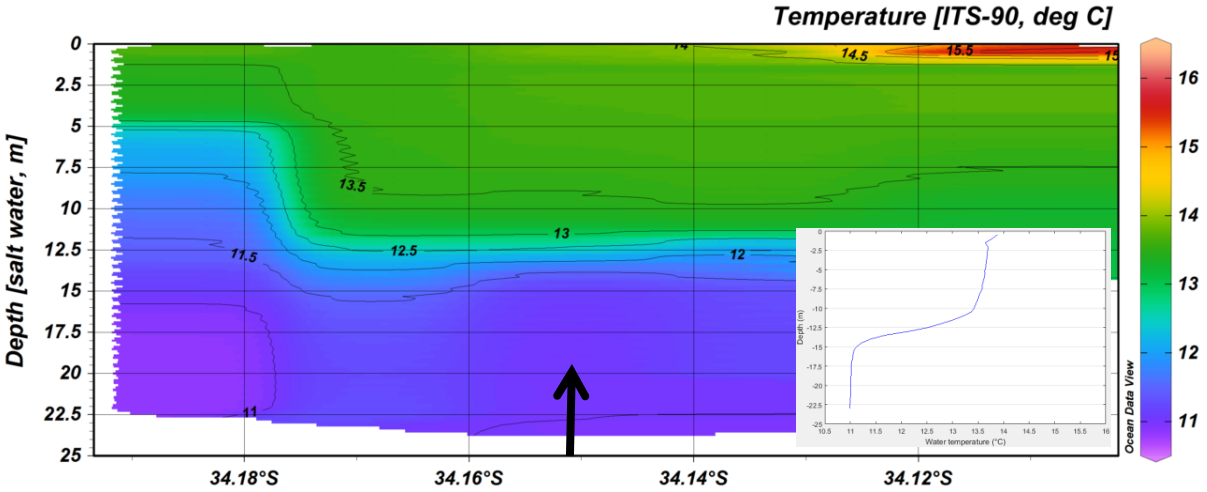

Figure 22: Water column temperature values for Profile 2 along the SJ-line (Schlitzer, 2019)

The thermocline present during Profile 2 (Figure 22) was much deeper (between 5 and 12.5 m) than the one present during Profile 1. The upper 12 m at the Profile 2 site was well mixed with temperatures ranging between 13°C and 14°C. These surface values (upper 1 m) show some resemblance with the surfboard (13.73°C) and radiometer (16.19°C) measurements. A pocket of warmer surface water was present approximately 1.7 km from the site in the direction of St James (Figure 8). The surface temperatures in this area were above 15°C and the water column was more stratified.

2015/09/08 (Profile 3)

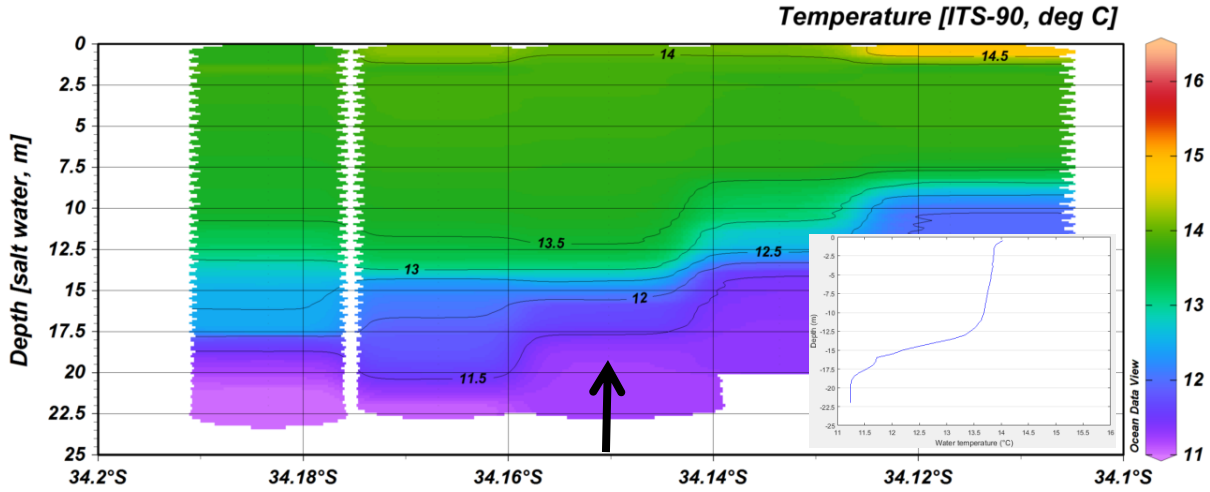

Figure 23: Water column temperature values for Profile 3 along the SJ-line (Schlitzer, 2019)

The water column had a well-mixed surface layer during Profile 3 (Figure 23) with the thermocline present between 7.5 and 12.5 m. The upper 12 m at the Profile site was also well mixed with temperatures ranging between 13.5°C and 14°C. These surface values (upper 1 m) are lower than the surfboard recorded values (16.92°C). The radiometer measured a skin temperature of 13.8°C which corresponds to the values in the upper 1 m of the water column. A pocket of warmer surface water was present approximately 3 km from the site in the direction of St James (Figure 8). The surface temperatures in this area were above 14.5°C.

2015/09/10 (Profile 4)

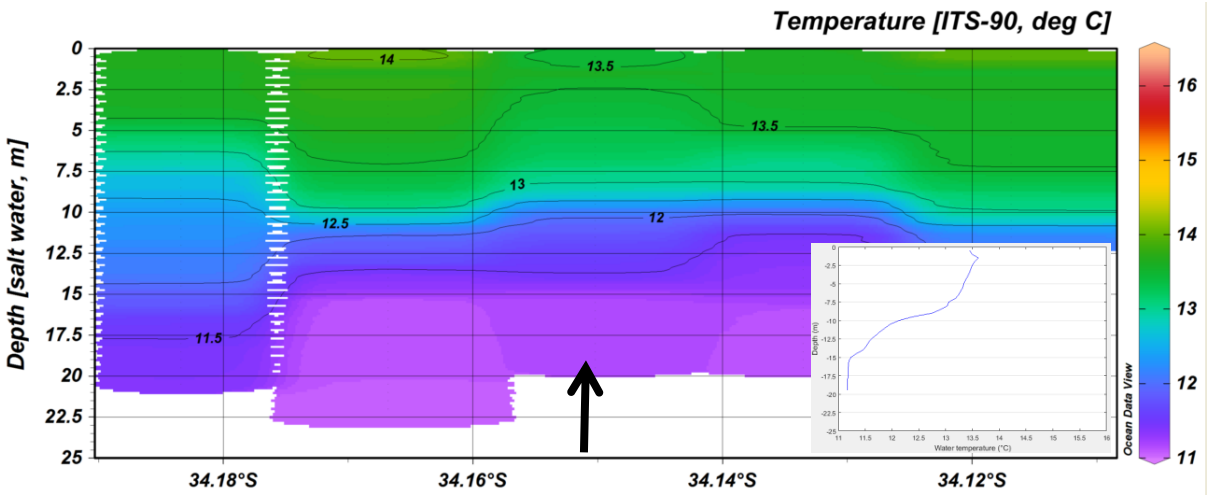

Figure 24: Water column temperature values for Profile 4 along the SJ-line (Schlitzer, 2019)

A well-mixed surface layer occurred during Profile 4 (Figure 24) with the thermocline present at approximately 8 m for the SJ transect. The upper 7.5 m at the Profile site was also well mixed with temperatures ranging between 13°C and 13.5°C. These surface values (upper 1 m) corresponded well with the surfboard recorded values (13.56°C). The radiometer measured a skin temperature of 16.49°C which was higher than the values in the upper 1 m of the water column.

4.2 Comparative vertical air profiling results – IOP2

In this section the experimental Helikite profiles will be compared to micrometeorological predictions by the TARMOS code. Vertical atmospheric conditions for air temperature, relative humidity and wind speed were available from each Helikite profile and are presented below. The results show the comparison between the actual atmospheric conditions and the predictions using various start values for the TARMOS model. Two of

the predicted profiles used the atmospheric parameters at the standard 10 m height, with only the SST input value changing, one profile utilised the radiometer value or 'skin' SST (green line) and the other the 'bucket' SST (blue line). Finally, the validity of using a 10 m standard as start atmospheric values was tested by using atmospheric values measured closer to the sea surface (pink line).

The profile legend, with a description of the parameters are summarised in Table 6.

Table 6: Summary of the vertical atmospheric graphs presented in this section

Legend	**Line**	**Description**
$Actual_d$	Solid red line	Helikite measured descending profile
$Actual_u$	Dotted red line	Helikite measured ascending profile
Modelled (-0.5m)	Solid blue line	TARMOS predicted profile using atmospheric values from the standard 10 m height (measured by the Helikite) as input. The SST value was obtained from the **surfboard** which was 0.5 m below the sea surface.
Modelled (SST)	Solid green line	TARMOS predicted profile using atmospheric values from the standard 10 m height (measured by the Helikite) as input. The SST value was obtained from the **radiometer** which measures the 'skin' temperature of the sea surface
Modelled (*m)	Solid pink line	TARMOS predicted profile using atmospheric values from the *lowest recorded* height (measured by the Helikite) as input. The input height used is provided in the legend (*m). The SST value was obtained from the **radiometer** which measures the 'skin' temperature of the sea surface

The various ASTD's for all the predicted values were calculated and summarised in Tables 7, 8, 9 and 10. This was done as a first attempt to see whether stable or unstable conditions could be expected, from the micrometeorology theory.

a. 2015/09/01 (Profile 1)

The ASTD calculated using the available values for air and sea temperatures all indicated stable atmospheric conditions. The respective ASTD's are provided in Table 7.

Table 7: Expected stability conditions for predicted profiles from the calculated ASTD: Profile 1

Legend	Air temperature	SST used	ASTD
Modelled (-0.5m) (Blue line)	14.94 °C (at 10 m)	13.85°C (surfboard) 'bucket' SST	+1.09°C
Modelled (SST) (Green line)	14.94°C (at 10 m)	12.37 °C (radiometer) 'skin' SST	+2.57°C
Modelled (3.4m) (Pink line)	15.08°C (at 3.4m)	12.37°C (radiometer) 'skin' SST	+2.71°C

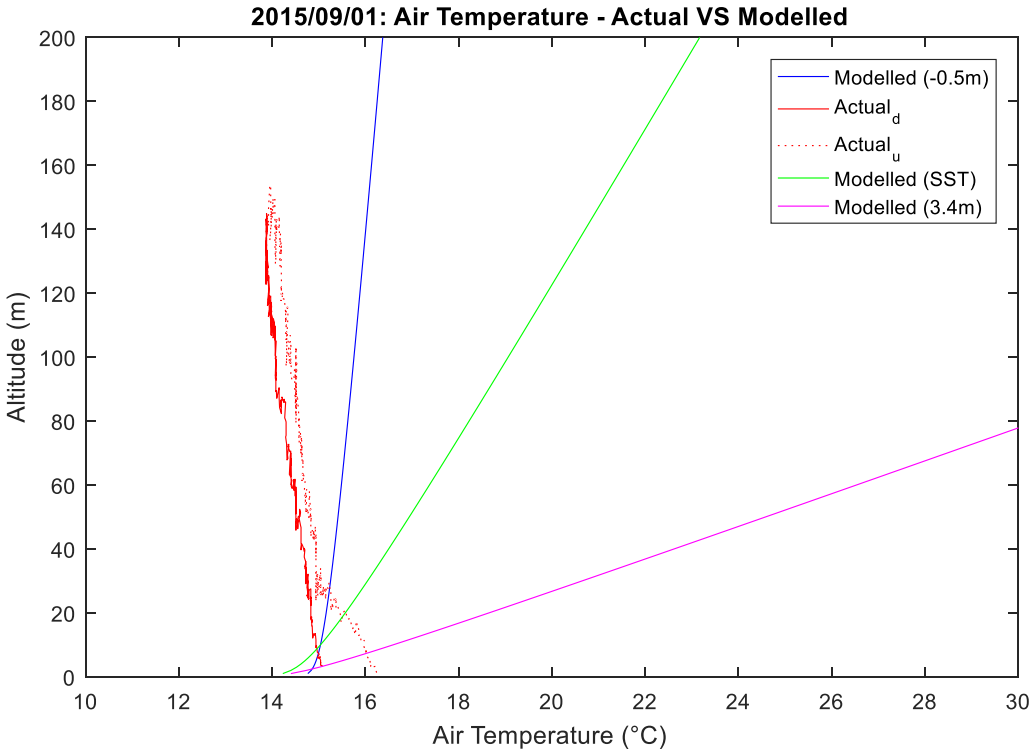

Figure 25: Profile 1: Helikite and TARMOS air temperature profiles

In accordance with the ASTD values, all the predicted profiles represent a stable atmosphere (Table 7 and Figure 25). Predicted temperature values increase with height, which is contrary to both measured profiles. The measured ascending profile showed unstable properties. In the lower 50 m the profile had a 1°C temperature drop from 16°C (0 m) to 15°C (50 m). From 50 m – 160 m the profile showed very little variation which indicates an unstable atmosphere. This 1°C drop in the temperature (16°C to 15°C) from the start of the profile (ascending) to the end of the descending profile in the lower 50 m is in accordance to the 1°C drop noticed in the general meteorological conditions measured on Roman Rock (14°C to 13°C) at the same time

(Figure 17b). The descending profile is primarily representative of unstable conditions with very little to no temperature change.

The predicted air temperature profile that best describes the measurements is obtained using atmospheric input values at 10 m and the SST values from the surfboard (i.e. the 'bucket' temperature), showing approximately 2°C difference between the measured and predicted profiles. The worst comparison was seen in the predicted profile that used input values at 3.4 m and the 'skin' temperature. This combination of input parameters produced a logarithmic plot with unrealistic temperature values at 200 m (55°C). Thus, the TARMOS model does not cope well with the surface layer conditions (as described by atmospheric input variables lower than the accepted 10 m and 'skin' SST).

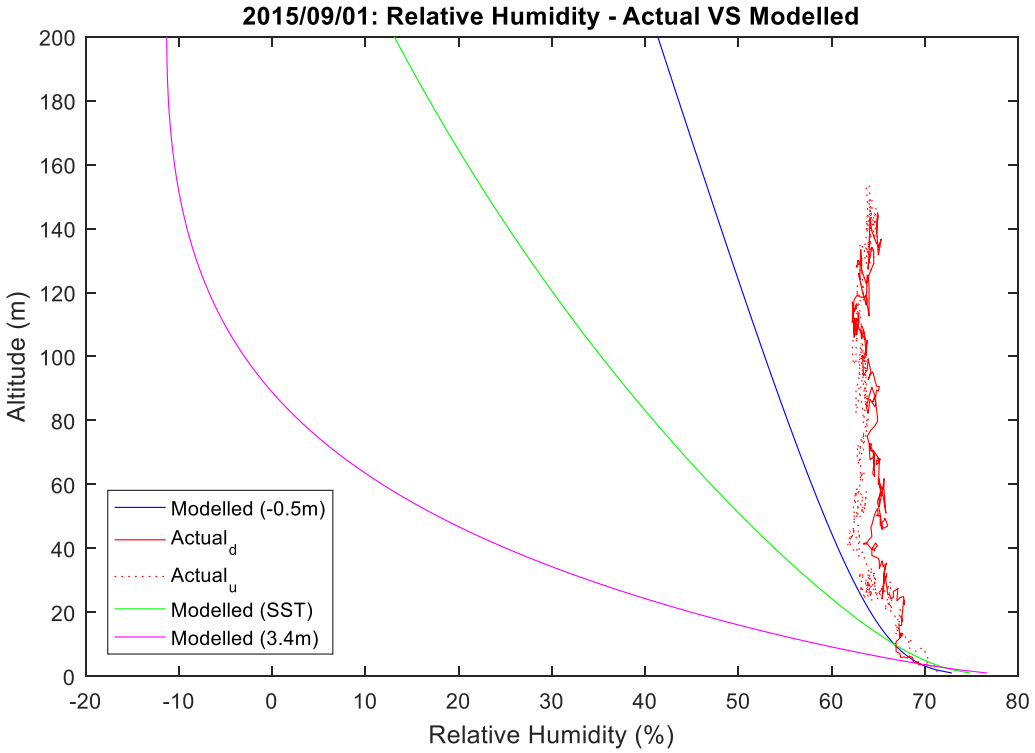

Figure 26: Profile 1: Helikite and TARMOS relative humidity

The relative humidity, as with the air temperature, represented a stable atmosphere for all the predicted profiles (Figure 26). Predicted relative humidity values decrease with height. The measured ascending and descending profile were similar ranging between 65% and 80%. Both measured profiles showed changing properties in the lower 20 m, with a 5% drop in relative humidity from 72% (0 m) to 68% (20 m). From 20 m – 160 m the profiles showed very little variation.

The predicted relative humidity profile that best described the measurements used atmospheric input values at 10 m and the SST values from the surfboard (i.e. the 'bucket' temperature). This predicted profile followed the measured profiles up to 40 m where they then diverge. At the highest point (160 m) the predicted profile was approximately 16% lower than the measured profile. The worst comparison was seen in the predicted profile that used input values at 3.4 m and the 'skin' temperature. This result, when using the 'skin' SST at 3.4 m could be indicative that TARMOS is not able to model the atmosphere correctly on the basis of the input data provided, and the clearest indication of this failure is given by the occurrence of negative relative humidity values. Also the validity of similarity theory (on which TARMOS is based) in the vertical plane is limited, implying that TARMOS inherently incapable of generating proper relative humidity profiles above a certain height (depended on the specific conditions), which in this case appeared to be in the region of 90 m altitude.

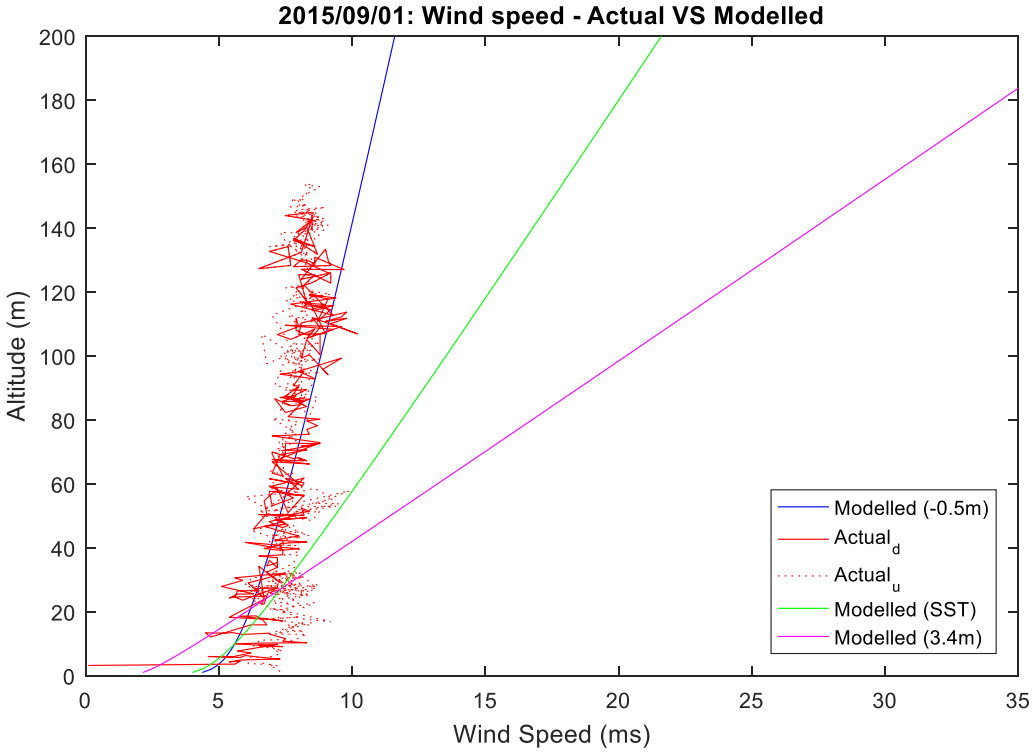

Figure 27: Profile 1: Helikite and TARMOS wind speed profiles

All the predicted wind speed profiles represented a stable atmosphere (Figure 27) and increased with height. The measured ascending and descending profiles both showed some variation in the lower 20 m. Wind speeds ranged between 5 m/s and 7 m/s.

The predicted wind speed profile that best described the measurements used atmospheric input values at 10 m and the SST values from the surfboard (i.e. the 'bucket' temperature). This profile followed the actual profile up to 130 m altitude. The worst comparison was seen in the predicted profile that used input values at 3.4 m and the 'skin' temperature with a 30 m/s difference between the two.

The atmospheric boundary layer on 2015/09/01 appears to be divided into two layers depicting changing conditions in the lower 50 m. This is evident in both the air temperature and relative humidity measured profiles (Figure 25 and Figure 26). In a separate unpublished study using WRF modelled runs, it was concluded that the atmosphere was slightly unstable on 2015/09/01 (pers. Comm. AMJ van Eijk, 2018), which is in accordance with most (above 50 m) of the Helikite profile. However, if it is accepted that the atmospheric surface layer only extended to a maximum of 50 m (as per the measured profiles), it would imply that TARMOS should not be used for predictions above this. Therefore, it can be concluded that the best fit for all parameters were the predicted profiles that used 10 m atmospheric values and the 'bucket' SST which was obtained from the surfboard measurements, but only in the lower 50 m. Using values from 3.4 m produced the worst comparison with the actual measurements in all cases.

b. 2015/09/07 (Profile 2)

The ASTD calculated using the relevant values for all the predicted profiles indicated unstable atmospheric conditions. The respective ASTD's are provided in Table 8 below.

Table 8: Expected stability conditions for predicted profiles from the calculated ASTD: Profile 2

Legend	Air temperature	SST used	ASTD
Modelled (-0.5m) (Blue line)	13.44°C (at 10 m)	13.73°C (surfboard) 'bucket' SST	-0.29°C
Modelled (SST) (Green line)	13.44°C (at 10 m)	16.19°C (radiometer) 'skin' SST	-2.75°C
Modelled (3.4m) (Pink line)	13.67°C (at 2.1m)	16.19°C (radiometer) 'skin' SST	-2.52°C

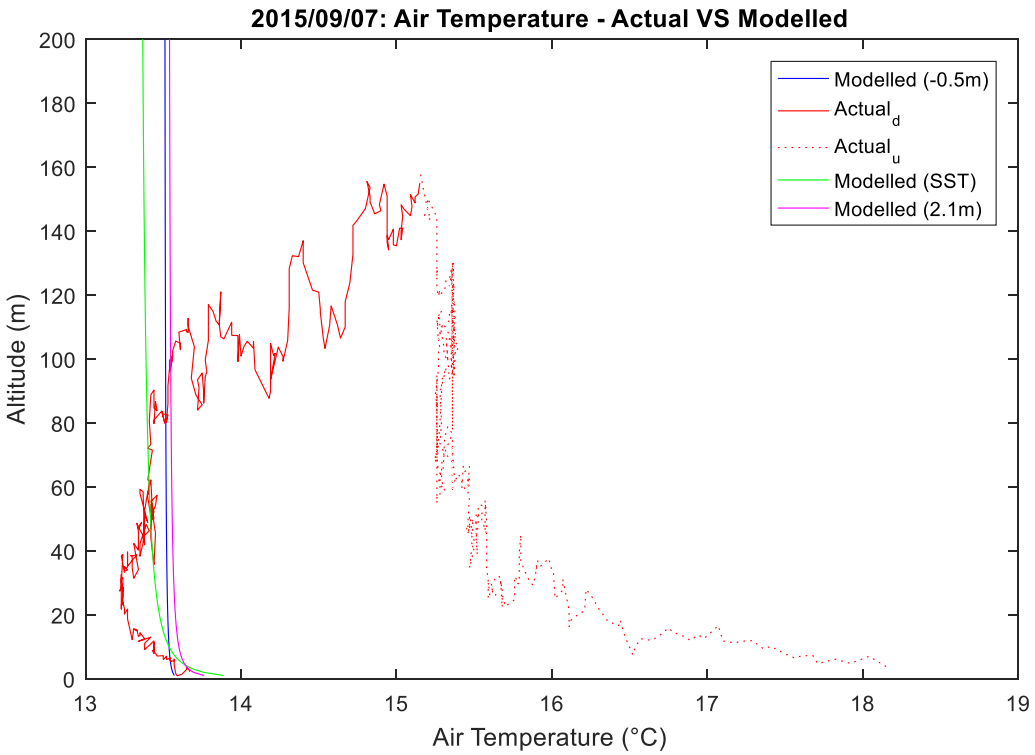

Figure 28: Profile 2: Helikite and TARMOS air temperature profiles

All the predicted profiles represent an unstable atmosphere (Figure 28). Predicted temperature values decreased fairly rapidly by 0.5°C above 10 m after which it remained uniform until 200 m. The measured ascending and descending profiles showed unstable properties, which could be as a result of the fact that it started raining during the taking of the profile. In the lower 50 m the profiles were again varying, with a 2.5°C temperature drop from 18°C (0 m) to 15.5°C (50 m) for the ascending profile and a 0.75°C drop (14.0°C – 13.25°C) for the descending profile. The descending profile displayed variable conditions from 80 m – 160 m and more constant conditions with very little to no temperature changes between 50 m and 80 m. There was also a 5°C temperature difference between the ascending (18°C at 0 m) to 13.5°C (at 0 m) for the descending value.

There was very little difference between all the predicted air temperature profiles (less than 0.5°C). All profiles however follow the descending profile below 100 m better (unstable conditions). This is could be explained by the fact the descending profile values were used as input to TARMOS when producing the predicted values. No comparison is seen between the predicted profiles and the atmosphere above 100 m. None of the predictions are representative of the ascending profile.

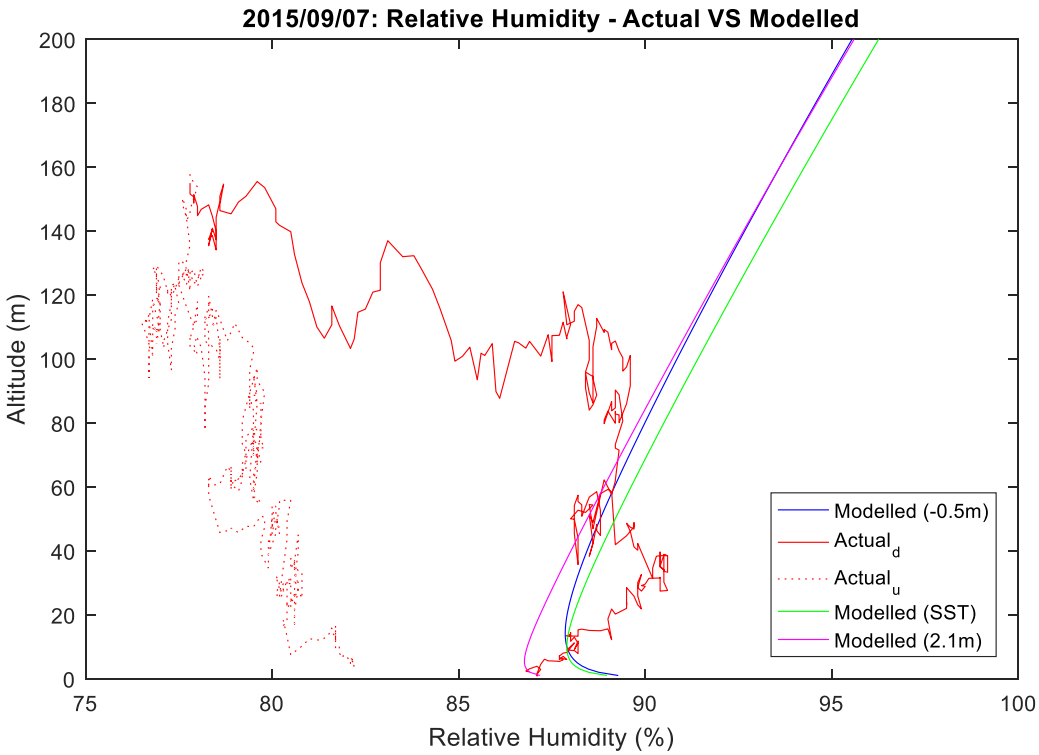

Figure 29: Profile 2: Helikite and TARMOS relative humidity profiles

Predicted relative humidity values increased with height. The measured ascending and descending profiles differed, ranging between 75% and 90%. The descending profile showed unstable properties in a changing atmospheric state. In the lower 50 m the profile showed a 5% increase in relative humidity from 87% (0 m) to 92% (40 m). Between 50 m and 120 m the profile depicts conditions with no variation in the relative humidity (88%). After 120 m the conditions again fluctuate decreasing with 10%. The ascending profile displayed less variation and ranged between 76% and 83%.

The predicted relative humidity profiles are very similar and tend to describe the descending measurements more (up to 60 m). Above 60 m this changes as the measured relative humidity (90% - 80%) decreases for both profiles as the height increases. The predicted relative humidity values (86% - 96%) increase with height.

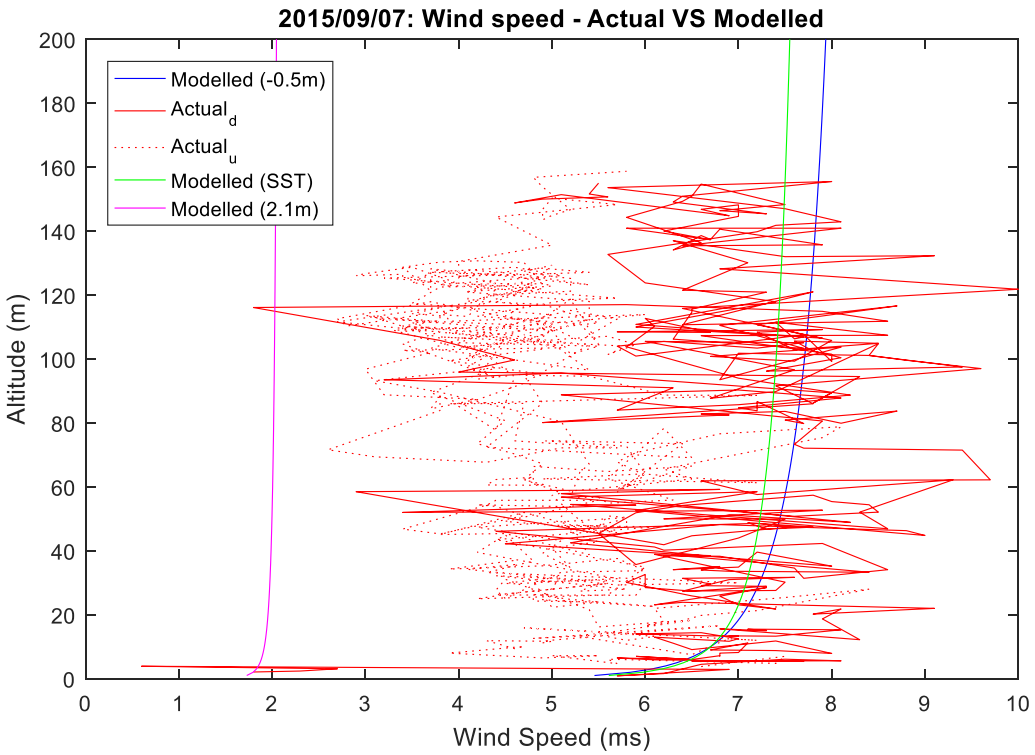

Figure 30: Profile 2: Helikite and TARMOS wind speed profiles

All the predicted wind speed profiles represented an unstable atmosphere (Figure 30), and displayed little to no variation with height. Both predicted profiles using the 10 m input values showed a 0.5 m/s change in wind speed in the lower 20 m. The measured ascending and descending profiles varied considerably and ranged between 1 m/s and 10 m/s. More variation was present in the ascending profile. Both measured profiles showed unstable properties.

The predicted wind speed profiles which used the 10 m input values (for both the surfboard and radiometer SST) described the measurements best, although it did not show the varying speeds (approximately 8 m/s difference) apparent in the measurements. The worst comparison was seen in the predicted profile that used input values at 2.1 m and the 'skin' temperature with a 6 to 8 m/s difference between the actual and predicted profiles.

It seemed as if the atmospheric conditions on 2015/09/07 were very variable and no clear pattern emerged from the measurements. Considerable variation is also present between the ascending and descending profiles for all atmospheric conditions.

The variation between the two measured profiles can be attributed to the fact that it started to rain in the descending profile. Generally rain would cause a lowering in temperatures (Figure 28), rise in relative humidity (Figure 29) and wind speeds becoming more variable (Figure 30). In False Bay the wind speed is known to increase during NW conditions which were present during this time (Figure 16 (c)). There was more similarity in the predicted profiles for all the parameters. Using values from 2.1 m produced the worst comparison with the actual measurements for wind speed. Relative humidity and air temperature showed some comparison between the actual measurements and all the predicted profiles.

c. 2015/09/08 (Profile 3)

The ASTD calculated using the relevant values for two of the predicted profiles indicated stable atmospheric conditions, and the third indicated unstable conditions. The respective ASTD's are provided in Table 9 below.

Table 9: Expected stability conditions for predicted profiles from the calculated ASTD: Profile 3

Legend	Air temperature	SST used	ASTD
Modelled (-0.5m) (Blue line)	16.49°C (at 10 m)	16.92°C (surfboard) 'bucket' SST	-0.43°C
Modelled (SST) (Green line)	16.49°C (at 10 m)	13.80°C (radiometer) 'skin' SST	+2.69°C
Modelled (3.4m) (Pink line)	16.54 l (at 1.5m)	13.80°C (radiometer) 'skin' SST	+2.74°C

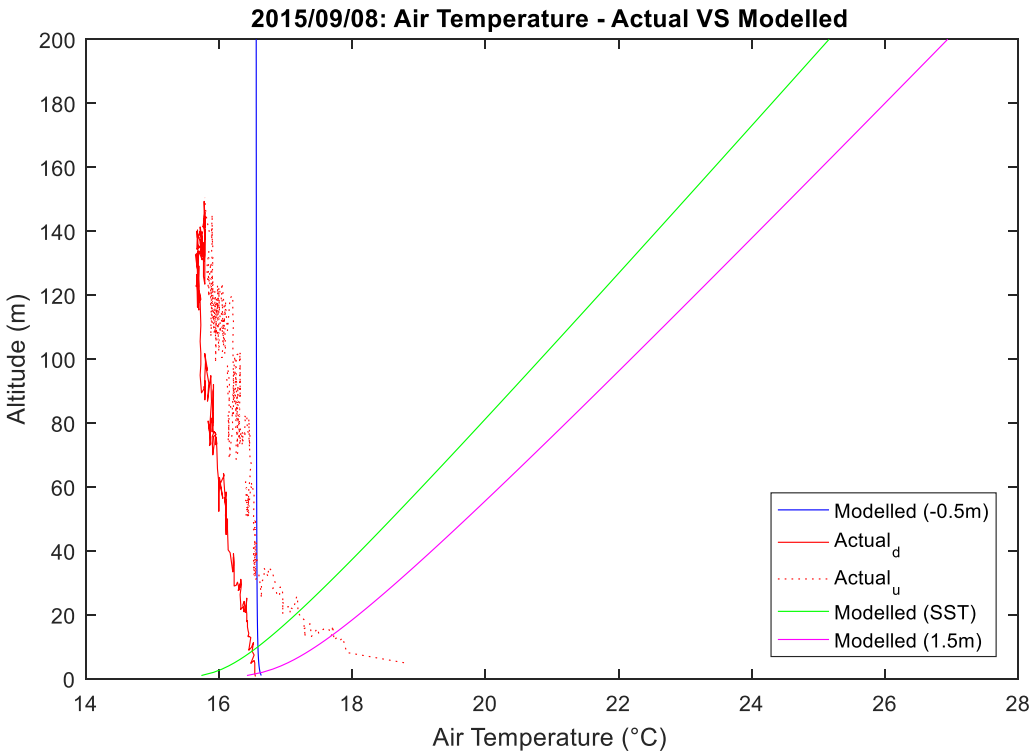

Figure 31: Profile 3: Helikite and TARMOS air temperature profiles

The predicted profiles using the 'skin' SST represented a stable atmosphere (Figure 31), whilst the 'bucket' temperature profile showed unstable conditions. This unstable profile displayed no change with height, remaining uniform at 16.5°C. The stable atmosphere profiles predicted temperature values that increased with height (from 16°C to 26°C). The measured ascending profile alluded to the possibility of a two atmospheric layers. A 2°C temperature drop from 19°C (0 m) to 17°C (50 m) occurred in the lower 50 m. A possible explanation for this could have been the temperature sensor response time, which highligh the fact that the sensor package must be stored away from direct sunlight and given an opportunity to stabilise before commencement of the profile. From 50 m – 150 m the profile showed very little variation. The descending profile was well-mixed with very little to no temperature changes (16°C – 16.5°C).

The predicted air temperature profile that best described the measurements used atmospheric input values at 10 m and the SST values from the surfboard (I.e. the 'bucket' temperature), showing approximately 1°C difference between the measured and predicted profiles. A better representation was seen above 50 m (unstable conditions). Both predicted profiles using the 'skin' temperature did not compare with the measured values.

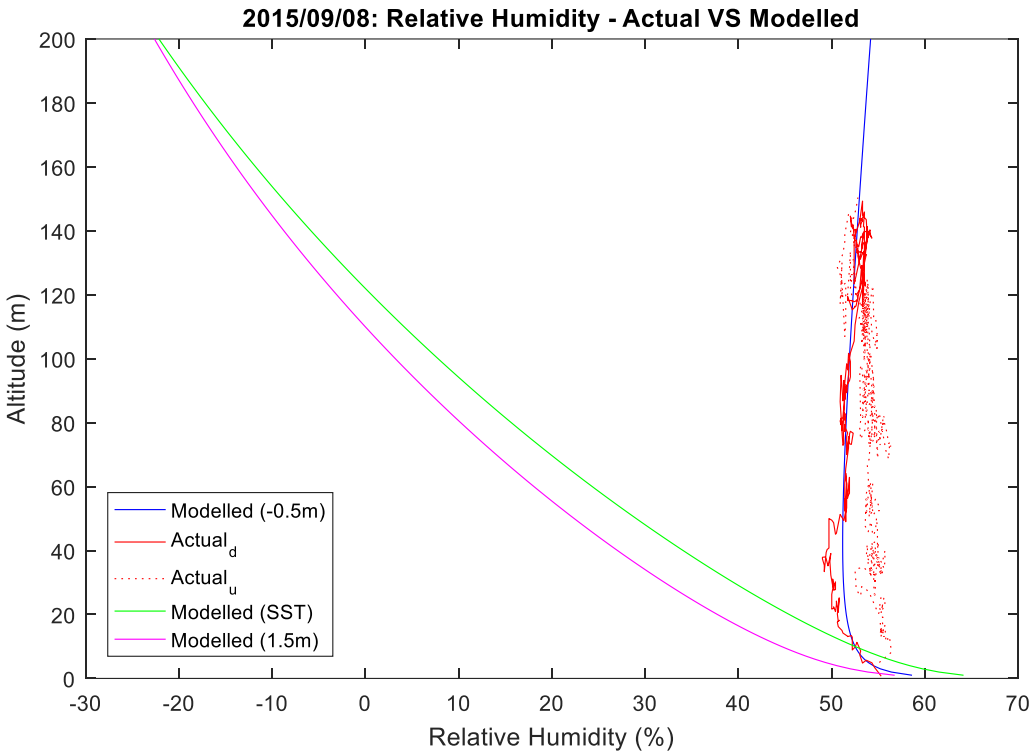

Figure 32: Profile 3: Helikite and TARMOS relative humidity profiles

The relative humidity followed the same trend as the air temperature, with the predicted profiles using the 'skin' SST not showing any comparison to that of the Helikite profiles (Figure 32). These predicted relative humidity values decreased with height. The measured ascending and descending profile was similar ranging between 53% and 56%.

The 'bucket' SST predicted profile (atmospheric input values at 10 m and the SST values from the surfboard) perfectly fits the descending relative humidity profile, with both depicting a value of approximately 52%. No comparison was seen in the predicted profiles that used input values at 'skin' temperature (radiometer SST). Those profiles also produced an unrealistic atmosphere (relative humidity values less than 0%) similar to what was seen in Profile 1 (Figure 26), which again shows that bulk micrometeorological equations utilised in TARMOS could not cope with this specific set of surface layer boundary conditions in False Bay. As with the relative humidity result in Profile 1, when using the 'skin' SST (Figure 26), the result above displayed the inability of TARMOS to generate proper relative humidity profiles above a certain height (depended on the specific conditions), which in this case appeared to be in the region of 80 m altitude.

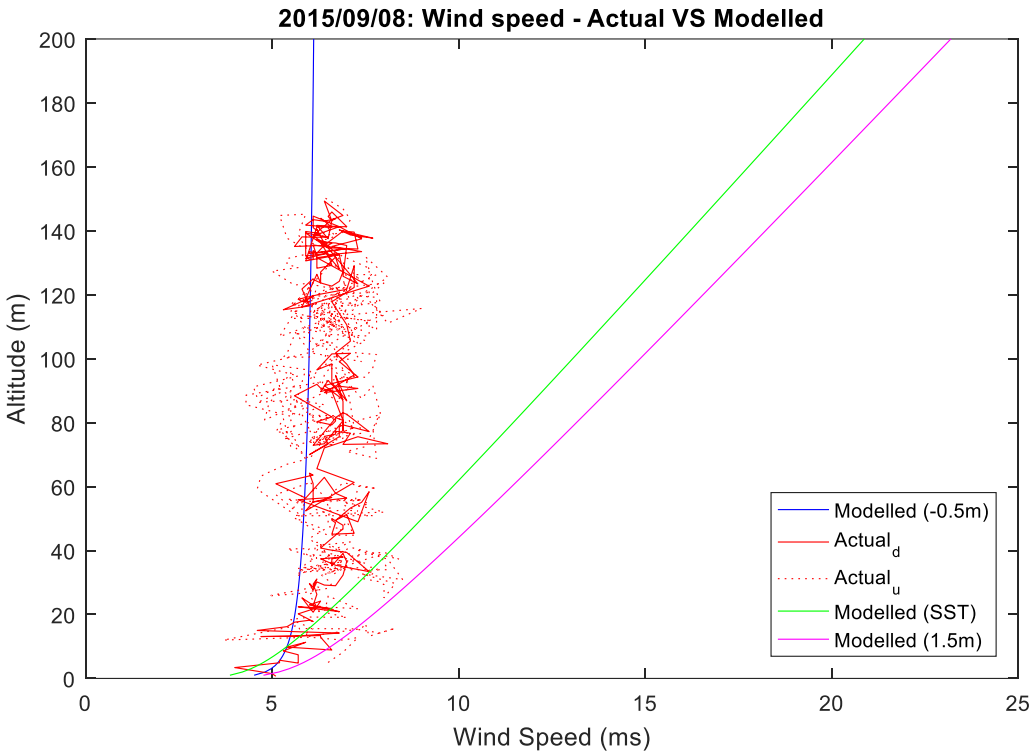

Figure 33: Profile 3: Helikite and TARMOS wind speed profiles

Two of the three predicted wind speed profiles represented a stable atmosphere (Figure 33), and increased with height. The predicted profile that used the 'bucket' temperature displayed properties of an unstable atmosphere with no change in wind speed as the height increased. The measured ascending and descending profile was similar ranging between 4 m/s and 8 m/s. Both measured profiles showed a well-mixed atmospheric layer with very little variation.

The predicted wind speed profile that best described the measurements used atmospheric input values at 10 m and the SST values from the surfboard (i.e. the 'bucket' temperature). Both predicted profiles that showed a stable atmosphere differed from the actual measured profiles as both increased in wind speed from 5 m/s (0 m) to 24 m/s (200 m).

It seemed as if the atmospheric conditions on 2015/09/08 were generally unstable with very little variation with an increase in height. All parameters followed this trend (Figures 30, 31, 32 and 33). There was an almost perfect fit with the predicted profile that used the 10 m atmospheric input values and a 'bucket' temperature (surfboard

values) for all parameters. The two profiles that used the radiometer SST values followed a similar trend and did not compare to the measured profiles.

d. 2015/09/10 (Profile 4)

The ASTD calculated using the relevant values for all the predicted profiles indicated unstable atmospheric conditions. The respective ASTD's are provided in Table 10 below.

Table 10: Expected stability conditions for predicted profiles from the calculated ASTD: Profile 4

Legend	Air temperature	SST used	ASTD
Modelled (-0.5m) (Blue line)	12.98°C (at 10 m)	13.56°C (surfboard) 'bucket' SST	-0.58°C
Modelled (SST) (Green line)	12.98°C (at 10 m)	16.49°C (radiometer) 'skin' SST	-3.51°C
Modelled (3.4m) (Pink line)	13.23°C (at 2.1m)	16.49°C (radiometer) 'skin' SST	-3.26°C

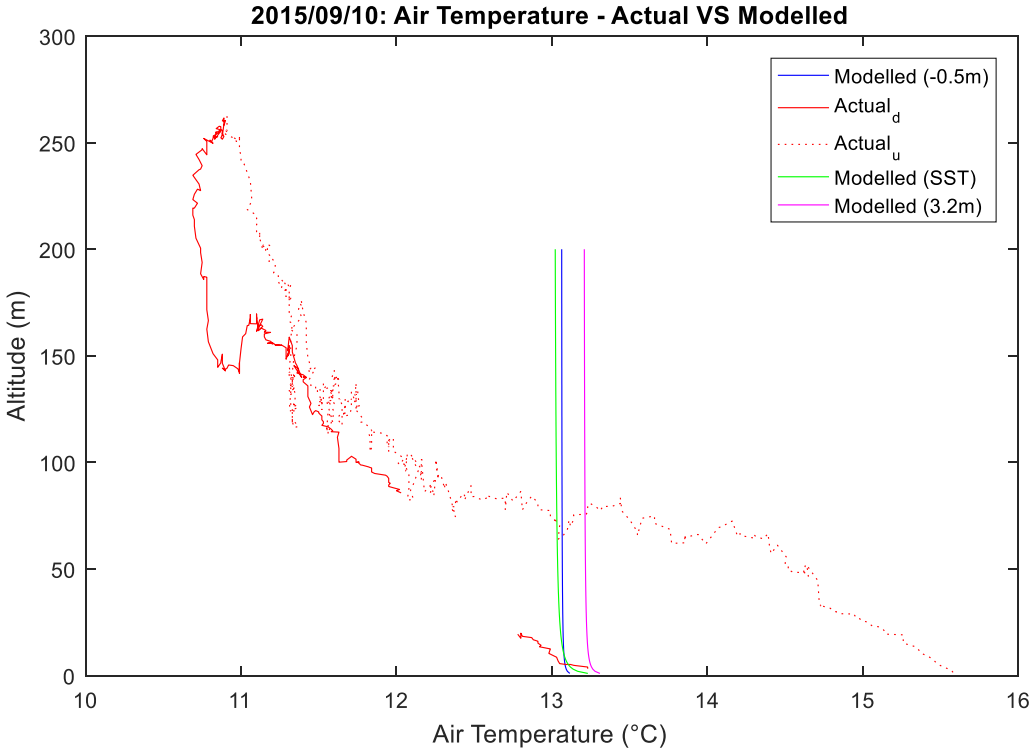

Figure 34: Profile 4: Helikite and TARMOS air temperature

All the predicted profiles represent an unstable atmosphere (Figure 34) and remained uniform until 200 m. There was also less than 0.5°C difference between the predicted profile values. The measured ascending and descending profiles showed variable conditions, with a 5°C temperature drop from 16°C (0 m) to 11°C (250 m) for the ascending profile and a 2°C drop (13°C – 11°C) for the descending profile. There was also a 3°C temperature difference between the ascending (13°C at 0 m) to 13°C (at 0 m) for the descending value.

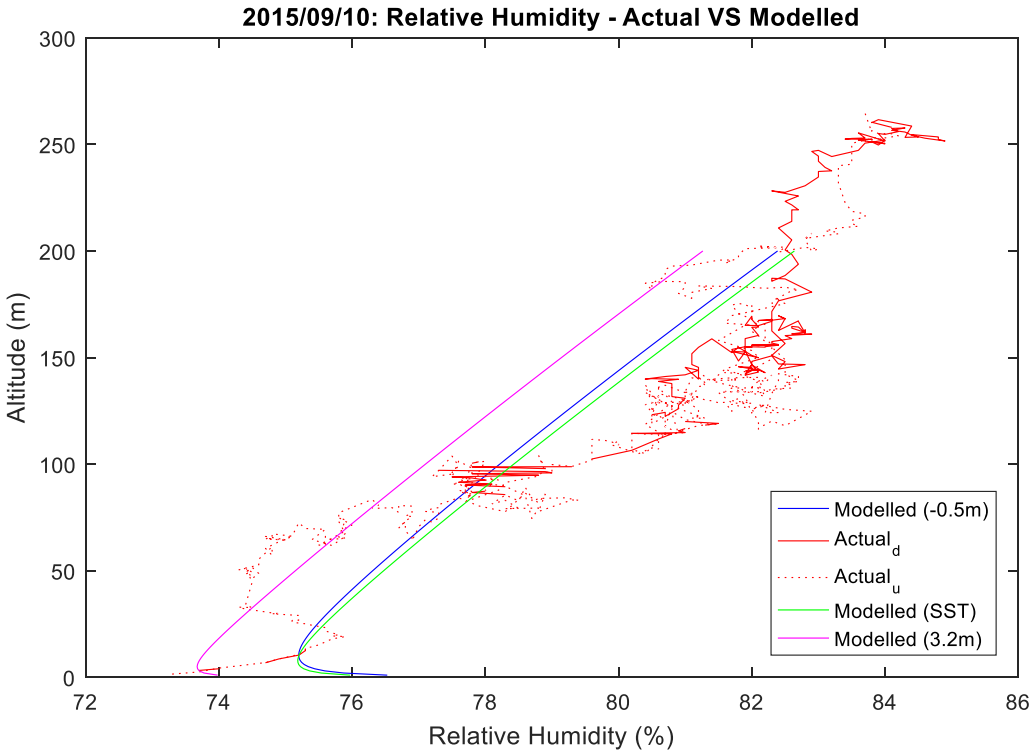

Figure 35: Profile 4: Helikite and TARMOS relative humidity

The relative humidity depicted an unstable atmosphere for all the predicted profiles (Figure 35). Predicted relative humidity values increased with height (74% - 82%). The measured ascending and descending were similar and representative of a two layered atmosphere ranging from 74% at 0 m altitude to 84% at 250 m.

The predicted relative humidity profiles are very similar and tend to follow the actual measurements well.

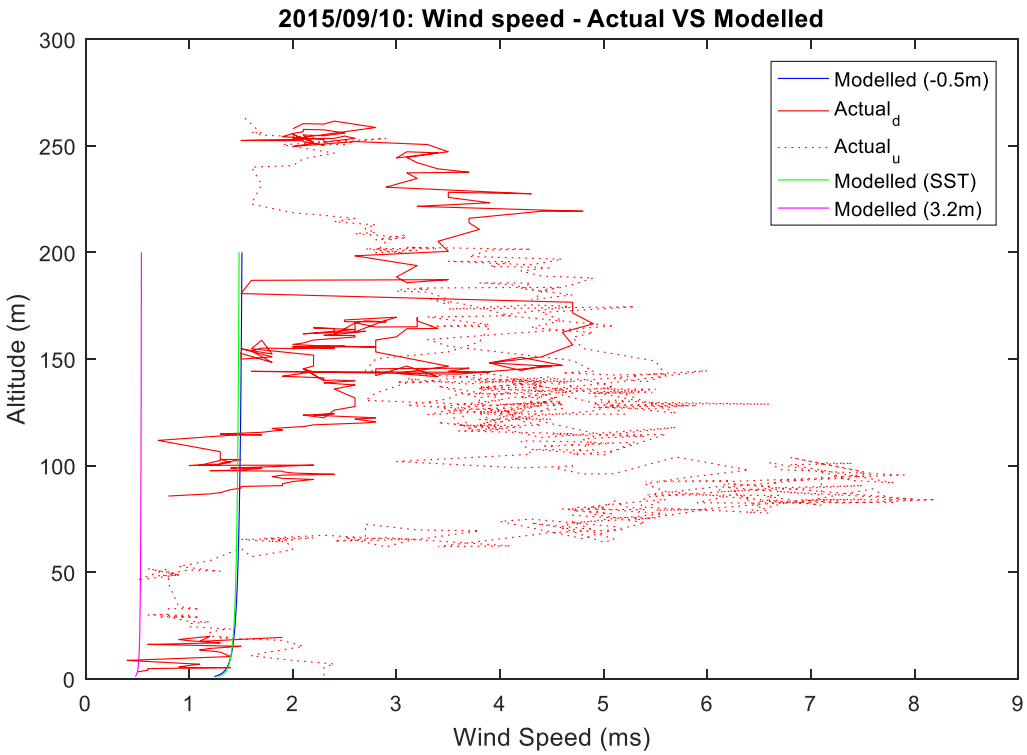

Figure 36: Profile 4: Helikite and TARMOS wind speed profiles

All the predicted wind speed profiles represented an unstable atmosphere (Figure 36), and displayed little to no variation with height. The predicted profiles using the 10 m input values were identical. The predicted profile using input values from 3.2 m was approximately 1 m/s lower than the other two profiles. The measured ascending and descending profiles varied considerably and ranged between 0.5 m/s and 8 m/s. More variation was present in the ascending profile.

It seemed as if the atmospheric conditions on 2015/09/10 were very variable and no clear pattern emerged from the measurements. However, little variation is seen between the ascending and descending profiles for the wind and relative humidity conditions. The temperature profiles show a 2.5°C difference between the beginning of the ascending and the end of the descending profile (Figure 34). Again this change can be attributed to the fact that it started raining during the descending profile. There was more similarity in the predicted profiles for all the parameters. Relative humidity showed some correlation between the actual measurements and all the predicted profiles.

4.3 Comparison between the Helikite sensor package and the radiosonde

As discussed previously, we were able to deploy the Helikite with two sensor packages attached to it, i.e., our own sensor package and a radiosonde package provided by WTD91 (Germany). Figure 36 shows the atmospheric profiles obtained during this deployment, the Helikite sensor package in red, and the radiosonde package in black. It should be noted that these profiles were recorded during sunny and calm conditions.

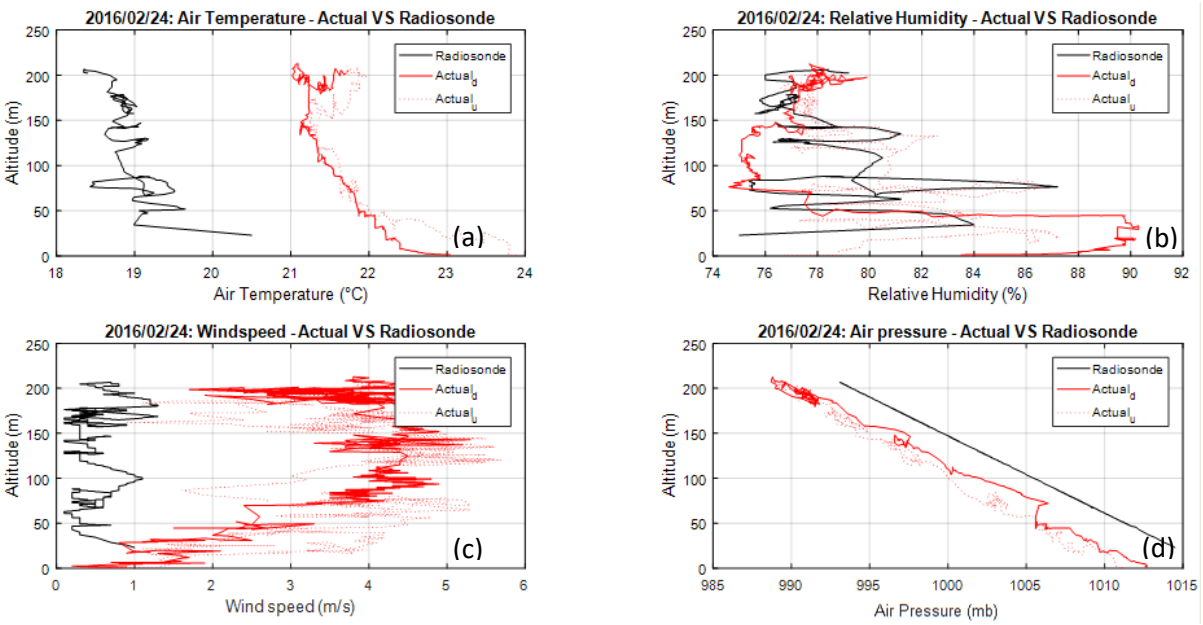

Figure 37: Comparative profiles from the different sensor packages

When comparing the Helikite and radiosonde air temperature values, it is apparent that there is a considerable difference. Both the ascending and descending profiles from the Helikite (red lines Figure 37a) were similar above the 50 m altitude. There was a 1°C temperature difference between the ascending (24°C) and descending (23°C) profiles in the lower 50 m altitude. The lowest value recorded by the Helikite was 21°C. The profile recorded by the radiosonde ranged between 18°C and 20.5°C and was approximately 2°C colder than the Helikite. Both sensor packages however recorded a higher temperature in the lower 50 m, cooling as the altitude increased, resulting in the shape of the profiles being similar.

Relative humidity data showed more variation ranging between 76% and 90% for the Helikite and 75% and 87% for the radiosonde (Figure 37b). A better comparison was present above 100 m altitude. The lower 100 m was more variable in both profiles.

The wind speed data did not correspond well (Figure 37c). The Helikite wind speed increased from 0.5 m/s to 5 m/s in the first 150 m before it decreased to approximately 2 m/s in the last 50 m. The radiosonde data were less variable reaching a highest speed of 1.5 m/s.

Profiles for air pressure showed a similar trend with the radiosonde pressure being slightly higher (approximately 2 – 6 mb) than the Helikite at all heights (Figure 37d). Highest values were 1015 mb (radiosonde) and 1013 mb (Helikite). The lowest values were 987 mb (Helikite) and 993 mb (radiosonde), respectively.

In assessing the comparative results it is seen that only the air pressure is comparable. The air temperature shows the same trends but the difference of 2°C between the profiles could pose a problem when using this data in the TARMOS model.

In order to see the effect of the different measurements on the bulk micrometeorological theory on which TARMOS is based, the Helikite and radiosonde data were used to generate predictions. As discussed in Section 3.5 no SST data from the radiosonde or surfboard were available during this comparison and the SST was inferred from MODIS at the location and time closest to the Helikite deployment.

The profile legend for these graphs are summarised in Table 11.

Table 11: Summary of the comparative graphs presented in this section

Legend	**Line**	**Description**
$Actual_d$	Solid red line	Helikite measured descending profile
$Actual_u$	Dotted red line	Helikite measure ascending profile
Modelled (heli)	Solid cyan line	TARMOS predicted profile using atmospheric values from the standard 10 m height (measured by the Helikite) as input. The SST value was obtained from the **MODIS satellite at 12:30**
Modelled (sonde)	Dashed black line	TARMOS predicted profile using atmospheric values from the radiosonde as input. The SST value was obtained from the **MODIS satellite at 12:30**

The ASTD calculated using the relevant values for the two predicted profiles indicated stable atmospheric conditions. The respective ASTD's are provided in Table 12 below.

Table 12: Calculated ASTD for the profile on 2016/02/24

Legend	Air temperature	SST used	ASTD
Modelled (heli)	22.40°C (at 11.2 m)	19.97°C	2.43°C
Modelled (sonde)	20.50°C (at 23 m)	19.97°C	0.53°C

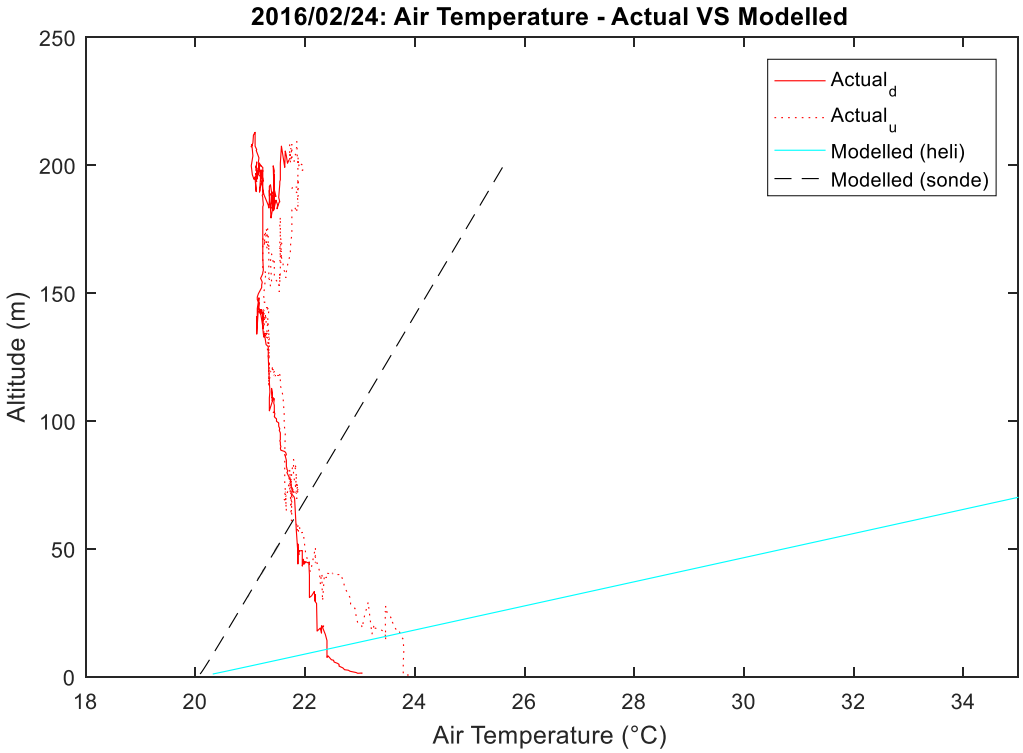

Figure 38: Air temperature – Comparing the measurements (Red plots) with TARMOS profiles using (a) Helikite values at 10 m as starting input with the satellite SST (cyan line); (b) Radiosonde values at 23 m as starting input with satellite SST (dashed black line)

Both the predicted profiles represent a stable atmosphere (Figure 38) and increased with height. There was a considerable change in the two predicted profiles with the Helikite predicted profile changing rapidly (20°C to 35°C) in the lower 100 m. The profile using radiosonde data varied between 20°C and 26°C (up to 200 m). The measured ascending and descending profiles showed unstable properties in the lower 50 m changing to unstable conditions above 50 m. A 2°C temperature drop from 24°C (0 m) to 22°C (50 m) for the ascending profile and a 1°C drop (23°C – 22°C) for the descending profile was seen.

No agreement is seen between the absolute values for the predicted and measured profiles.

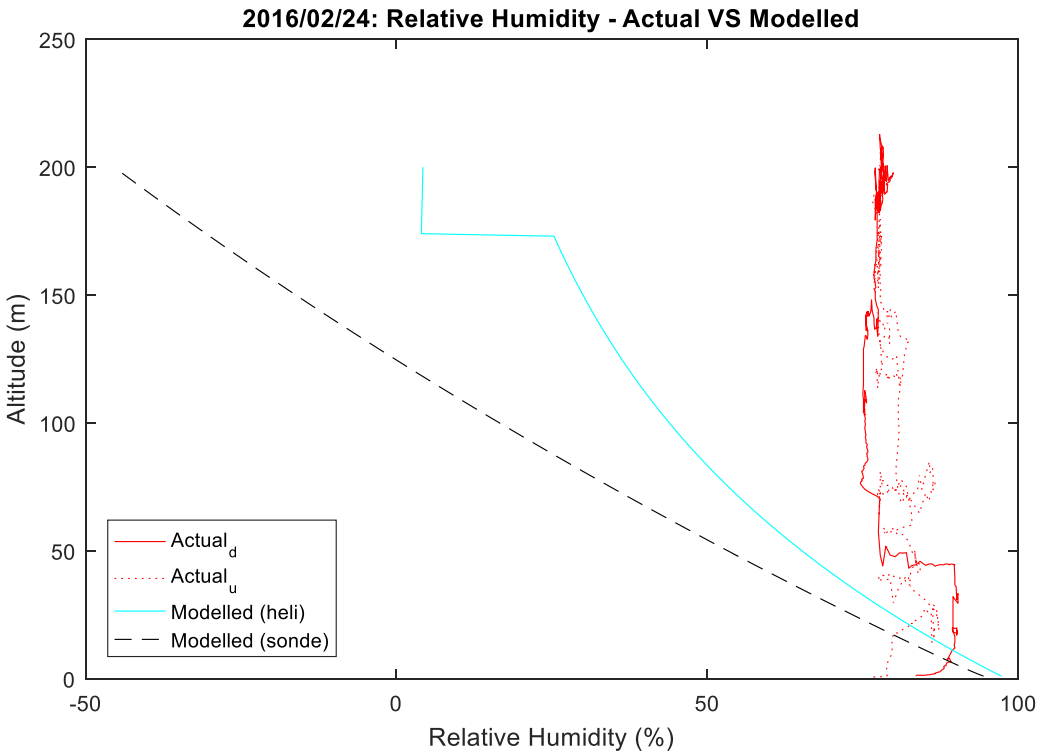

Figure 39: Relative humidity – Comparing the measurements (Red plots) with TARMOS profiles using (a) Helikite values at 10 m as starting input with the satellite SST (cyan line); (b) Radiosonde values at 23 m as starting input with satellite SST (dashed black line

The relative humidity depicted a stable atmosphere for both predicted profiles (Figure 39). Predicted relative humidity values decreased with height (0% - 100%). The profile using radiosonde data produced an unrealistic atmosphere (i.e. relative humidity values less than 0%), indicating that the bulk micrometeorological equations utilised in TARMOS could not cope with this specific set off surface layer boundary conditions. As with the relative humidity result in Profile 1 (Figure 26) and Profile 3 (Figure 32), the result above displayed the inability of TARMOS to generate proper relative humidity profiles above a certain height (depended on the specific conditions), which in this case appeared to be in the region of 140 m altitude. The measured ascending and descending profiles were similar, with the descending profile showing a rapid change in relative humidity (70% to 90%) at 50 m. Atmospheric conditions above and below this layer where the change occurred were representative of unstable conditions.

Neither predicted relative humidity profiles compared well with the actual measurements.

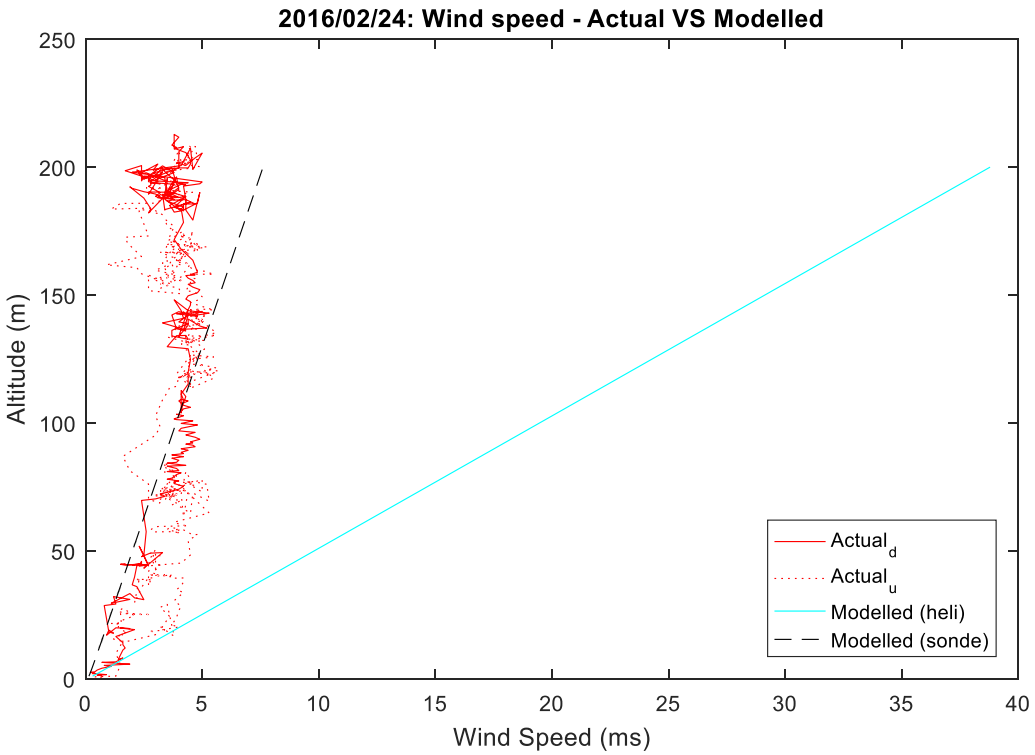

Figure 40: Wind speed – Comparing the measurements (Red plots) with TARMOS profiles using (a) Helikite values at 10 m as starting input with the satellite SST (cyan line); (b) Radiosonde values at 23 m as starting input with satellite SST (dashed black line)

The predicted wind speed profile using Helikite data represented a stable atmosphere (Figure 40), and increased with height (0 – 40 m/s). The predicted profile that used the radiosonde data was less variable ranging between 0 m/s and 5 m/s. This profile also compared the best with the measured profiles. The measured ascending and descending profile also ranged between 0 m/s and 5 m/s. Both measured profiles showed unstable properties with very little variation.

4.4 Results Summary

Both dominant wind conditions in False Bay (SE and NW) were present during the time of the measurements. Profile 1 was done during the SE conditions and Profiles 2 and 3 during NW conditions. The wind speed on the day of Profile 3 was lower than that of Profile 2. Wind conditions (speed and directions) were variable during the taking of Profile 4.

General air temperatures in the area were below 16°C on the days when profiles were measured. However, the air temperature reached heights of 23°C (4th), 26°C (5th) and

25°C (6th) the three days prior to Profiles 2 and 3. These higher temperatures were also present during low (less than 4 m/s) wind speed conditions (Figure 17 and 16).

The air pressure was increasing from 1015 to 1025 mbar the day before Profile 1. After Profile 1 the pressure dropped to 1005 mbar on the day before Profile 2. On the day of Profile 2 the air pressure remained stable with only a 5 mbar change (1005 – 1010 mbar), climbing 10 mbar to reach 1020 mbar on the 8th (Profile 3). The air pressure was stable (1010 - 1015 mbar) the day before and on the day of Profile 4 (Figure 18).

Rain was present during the recording of Profiles 2 and 4. No rain occurred during Profiles 1 and 3. Both measured 'dry' profiles for air temperature showed a decrease in temperature from the sea surface to approximately 20 – 40 m altitude during the ascending measurement highlighting the fact that the sensor package must be stored away from direct sunlight and given an opportunity to stabilise before commencement of the profile. The descending profile for air temperature does not show this. It is also clear that the predicted TARMOS profile that resembles this shape the best were using atmospheric input data from the 10 m Helikite readings and the 'bucket' temperature (which comes from the surfboard) as start values. Both predicted profiles using the radiometer SST value as a start do not correspond with the measurement from the Helikite. This trend is also apparent for the relative humidity and wind speed. On the 8th (Profile 3) the shape of the 'bucket' temperature SST predicted profile for relative humidity and wind speed almost exactly follows that of the descending measured profile.

The results were different between the measured and predicted profiles on the 'wet' days (Profiles 2 and 4) with the exception of relative humidity on the 10th (Profile 4). On this day all the TARMOS predictions follow the same trend as the measured data (Figure 35). Air temperatures in the lower 100 m show a 4°C and 3°C difference respectively between the ascending and descending profiles. Wind speed measurements were also much more variable when compared to the predictions.

When analysing the recorded temperatures at CTD3 (Figure 21 – insert) for Profile 1, it is seen that the CTD surface values (upper 1 m) were higher when compared to the surfboard and radiometer values (Table 14) as discussed in section 4.1c – Profile 1. If these higher values from the CTD were used to drive the TARMOS model, the ASTD (–0.06°C) would have forced the modelled output towards neutral or unstable profiles. This could possibly have compared better with the measured profiles (above 50 m) on

2015/09/01 (see Figures 25, 26 and 27). The upper water layer (0 – 1 m) across the SJ-line was mostly homogeneous only increasing slightly towards the SJ CTD station (Figure 22) on 2015/09/07. CTD recorded temperatures at the profile site was similar to that of the surfboard temperature (Section 4.1 c – Profile 2). It was however lower than the radiometer values (Figure 22 – insert). Using all available water temperature values as SST inputs, the ASTD for Profile 2 indicated unstable conditions (Table 13) which is in accordance with the measured profiles above 50 m. However, none of the predicted profiles were representative of the measured conditions (Figures 28, 29 and 30). Surface water temperatures from the CTD during Profile 3 compared better with the radiometer value (Figure 23 – insert). The water column is also well-mixed at the site, with the warmer pocket towards the SJ site weakening. Both ASTD's (CTD and radiometer) depict stable conditions, whilst the surfboard is indicative of unstable atmospheric conditions (Table 13). This unstable condition is best represented by the measured profiles (Figure 31, 32 and 33). On 2015/09/10 (Section 4.1 c – Profile 4) the CTD measurements was again similar to that of the surfboard values (Figure 24 – insert). All water temperature measurements suggest unstable conditions, whereas the measured profiles are representative of stable conditions (Figures 34, 35 and 36).

Table 13: Water column characteristic summary, including ASTD calculations using different instruments for SST values

Profile	Air (10m)	Surf	Radio	CTD	ASTD Surf	ASTD Radio	ASTD CTD	Transect description
1	14.94	13.85	12.37	15.00	1.09	2.57	-0.06	Inhomogeneous
2	13.44	13.73	16.19	13.75	-0.29	-2.75	-0.31	Homogeneous
3	16.49	16.92	13.80	14.00	-0.43	2.69	2.49	Homogeneous
4	12.98	13.60	16.49	13.50	-0.62	-3.51	-0.52	Homogeneous

The wave conditions during IOP2 (time of all profiles) were below 2 m with the highest waves recorded during Profile 1 which coincided with the SE wind conditions. A strong SE (12 – 14 m/s) was present the day before Profile 1, which could have influenced the height (1 – 2 m). Southeasterly wind conditions are onshore and have a long fetch (29 km) from the entrance of False Bay. Thus, SE conditions are generally associated with higher waves in the study area. Wave heights below 0.5 m were present for the rest of the Profiles which were collected during the NW and variable conditions. This could be explained by the fact that the waves were measured close to the shore (1.6 km). During northwesterly wind conditions, the wind blows offshore and the areas closer inshore tend

to be in a lee created by the surrounding mountain ranges. These areas usually display low wave heights, with surface chop. The wave period was between 4 and 6 seconds during all the profiles and does not seem to be affected by the wind direction.

Table 14 summarises all parameters during the four profiles and serves as a quick look for changes and similarities:

Table 14: Summary of parameters on the profile days

Parameter	**Profile 1**	**Profile 2**	**Profile 3**	**Profile 4**
Wind direction	Strong SE	Fresh NW	Light NW	Variable
Air Temperature	Low	Low but preceded by 3 days of high temperatures	Low but preceded by 3 days of high temperatures	Low
Air pressure	Increasing	Stable	Increasing	Stable
Precipitation	No rain	Rain	No rain	Rain
Wave height	Highest 2 m	Below 0.5 m	Below 0.5 m	Below 0.5 m
Water column temperature	Highly stratified. Surface (up to 2.5 m) 15 – 17°C Shallow thermocline Two hot pockets in front and after profile site	Well mixed up to 10 m. Surface mixed layer 13 – 14°C Deeper thermocline (12m). One hot pocket after profile site	Well mixed up to 12.5 m. Surface mixed layer 13.5 – 14°C Deeper thermocline (12.5m). No hot pockets	Well mixed up to 10 m. Surface mixed layer 13 – 13.5°C Deeper thermocline (10m). No hot pockets
Predicted VS measured	'Bucket' SST and 10 m input. Other two profiles show bad correlation	None of the predicted represent the measured	'Bucket' SST and 10 m input. Other two profiles show bad correlation	None of the predicted represent the measured – except Relative humidity for all predictions

CHAPTER 5: DISCUSSION

This thesis had two objectives: Proving that the Helikite and the sensor package developed for this study could be used to measure and characterise the lower atmosphere in False Bay, as well as evaluating the suitability in using micrometeorology theory to describe the marine surface layer in the study area. Following these two objectives this chapter aims to provide input into evaluating the physical system and its overall suitability for measuring profiles at sea in the study area. It will also describe the complexity of the environment and the possible effect atmospheric, oceanic and geographic conditions in False Bay had on the measurements and subsequent predictions when applying micrometeorology theory. A brief section discussing the value of using measured profiles, or the correct input parameters in prediction models when estimating EO propagation along a transmission path is also included for completion sake.

From the preceding studies (Section 2.5) it is clear that a Helikite has been used successfully as a lifting platform and is a relatively cost effective system. What set this study apart though was the measurement package utilised. The Airmar PB200 is currently the best suited for this type of measurements due to its compact size, fast response times (1s) and ability to correct for platform movement internally, which currently separate it from other compact weather stations. It should be noted that there is a growing concern in the scientific community that the Airmar over-estimates wind speed and that the data gathered are not considered to be of a scientific standard. This could have contributed to the discrepancies seen in some of the predicted vs. measured profiles in Chapter 4. The Airmar's temperature sensor was also not accurate enough for this work (Section 3.2), which is why a LM35 temperature sensor was incorporated into the measurement package for this study. When comparing the radiosonde data to that of the Helikite sensor package (Section 4.3), it seemed as if the Helikite sensor package was relevant. This comparison demonstrated that the Helikite was more suited to measuring high-resolution profiles up to 200 m than the radiosonde.

At the time of the experiment, focus was also placed on the ASTD measurements, and the experimental use of the surfboard (Section 3.3b) proved valuable. The fact that this experiment considered both the skin and 'bucket' SST was unique for comparison purposes, specifically when taking into account the ASTD differences that were seen between using the two values and the resultant air profile predictions. The 'surfboard' performed well in providing continuous bulk SST values during the study.

In Muschinski et al., (2001) two lifting systems were used to measure the turbulence in the lower atmosphere and although both systems showed their capability to do this, it cannot easily be compared to the IMT Helikite system used in the FESTER experiment. The systems discussed were much larger and considerably more expensive (especially the HELIPOD). However, the above comparison between using an aircraft (HELIPOD) or tethered balloon highlighted the advantages and disadvantages of a fixed balloon or kite platform over that of an air-borne system. Although the IMT Helikite proved useful in acquiring vertical air profiles at sea during this study, the disadvantages found by Muschinski et al., (2001) for tethered platforms became apparent. Firstly the deck space on the workboat proved to be a limiting factor in the size balloon that could be used, limiting the weight of the payload. A second very important limitation was the wind speed, as it became nearly impossible to operate the Helikite safely in speeds higher than 10 m/s. Higher wind speeds (above 5 m/s) also increased the sway of the sensor package below the Helikite which could affect the measurements. Furthermore, maximum heights obtained were limited as it is reliant on available cable (tether). Hence, it should be noted that the weight of the tether and wind drag on it must be considered as this affects the operation of the Helikite and heights it could reach.

During the analysis of the environmental data for this study it became apparent that the environmental conditions in the study area can be considered to be complex. This holds true for both the oceanic as well as the atmospheric conditions.

In a study aimed at understanding the seasonal and inter-annual variability in the False Bay SST (Dufois & Rouault, 2012), satellite data from 2000 to 2009 were analysed. This study found that the northern part of the bay (area where profiles were taken) in general displayed a higher variation during summer months. As the study period in this thesis occurred during the transition between spring and summer it is understandable that there was a higher variability in SST during the taking of the atmospheric profiles, given the results from Dufois and Rouault (2012). In general local seasonal signals, like sun warming and upwelling cells, were more likely to influence the shallower northern area off False Bay. These upwelling cells that could be present are driven by the dominant SE wind regime in spring, summer and autumn.

The results presented in Section 4.2 are comparable to this situation. Colder water entered the bay from the SW (in-line with the dominant swell conditions in the area), and flowed in a clockwise direction, as is the preference for current circulation (Dufois & Rouault, 2012) in False Bay. The inhomogeneous path (between CTD 1 and CTD 5) showed higher SST's in the NE side (CTD 5 and CTD 4) compared to the NW, which can be explained by the effect of local

seasonal signals (sun warming). As the colder water (CTD 1 to CTD 3) from the SW enters the area it decays and is replaced by the higher SST's in the NE.

The water column during Profile 1 was highly stratified, displaying the largest difference between surface (16.5°C) and bottom (13°C) water temperatures. During this time surface heat pockets could also be seen. These pockets were possibly the remains of localised warming and South coast water entering False Bay from Cape Hangklip during SE wind conditions. However, the colder water below 2.5 m is suggested to be modified Benguela upwelled water entering from Cape Point as bottom water (pers. Comm. Dr CK Wainman, 2018). The water temperature conditions during Profiles 2 and 3 showed the area between CTD 1 and CTD 4 (Figure 7) to be colder than the surface water towards SJ (CTD 5). Limited previous studies in the area seem to suggest a frontal condition that is present here. This frontal condition showing the 1.5°C surface water temperature difference between CTD stations 1-4 and CTD station 5 could be the result of forcing by the regional wind patterns on the larger False Bay scale (Wainman, 2000). A weak thermocline is present during Profile 4 at approximately 10 m water depth. All the warm surface pockets have disappeared, possibly as a result of the forcing mechanism (i.e., wind) dissipating.

On the two days where the predicted TARMOS profiles best described the atmospheric conditions as measured (Profile 1 and 3), no concrete pattern emerged when only considering the water column temperature. The water column was highly stratified and the SST across the transmission path was inhomogeneous during Profile 1. These conditions were directly opposite to those seen during Profile 3, which had a homogenous transect path and a well-mixed surface layer. Water column properties for Profiles 2 and 4 were similar to those during Profile 3. This would therefore indicate that the water column structure does not play a significant role in the prediction of atmospheric profiles at this specific site. The results in Section 4.1 c do however show that the area in question could change significantly over the 6.5 km of the transect line as a result of processes described above. This change could have an impact on atmospheric profiles predicted using micrometeorology theory, as the numerical models would depend on the input values, which is site specific and not necessarily descriptive of the transect line. Considering that the SST could be very site specific, i.e. changing from one site to the next, these input values could mean the difference between a positive, neutral or negative ASTD as is seen in Table 14 – Profile 1. It is therefore advised to either measure or model the water column properties when using a EO-TDA application in the coastal area of False Bay.

During this study, effort was spent on measuring the SST, as this is an important factor describing the ASTD, which is considered to be one of the main driving forces in utilising micrometeorology theory to predict atmospheric profiles. As the theory is based on bulk parameterisations the question arose whether the 'bucket' or skin SST would be the best to use. In the study the 'bucket' SST was measured by the sensor package on the surfboard and could be considered 'bulk' values as it measured the averaged conditions in the upper 0.5 m of the water column. The skin SST, which only describes the upper 10µm, was acquired using the Heitronics radiometer. The results in Section 4.2 showed that the predictions using the bulk SST better represented the measured condition for Profiles 1 and 3. On closer inspection of the ASTD values, more inconsistencies become visible. According to the ASTD calculations (Tables 8, 9, 10, 11 and 14), the atmosphere was expected to show stable atmospheric conditions during Profile 1 and unstable conditions during Profile 3. Profile 3 best represented the measurements (Figures 31, 32 and 33) when using the bulk SST, with Profile 1 only showing somewhat comparable results (Figures 25, 26 and 27). This led to the assumption that micrometeorology theory would be more accurate during unstable conditions and with a negative ASTD, as indicated in Section 2. During Profiles 2 and 4 the ASTD also indicated unstable conditions but almost no comparison (with the exception of relative humidity during Profile 4) between any of the predicted profiles (Figures 28, 29, 30, 34, 35 and 36) were seen during these days. In fact, the predicted profiles for Profile 1 and 3 still provided the best description of the measured environment even though the one ASTD was indicative of stable and the other of unstable conditions. Thus, although ASTD is an important driving parameter in atmospheric predictions using micrometeorology theory, it does not seem to be the most important in False Bay, and it must be considered in conjunction with the other environmental parameters.

In a separate comparison (Section 4.3) between the Helikite sensor package described in Section 3.2 and that of a GRAW Radiosonde DFM-09 (See Appendix C for specifications), no measured SST (from either the radiometer or surfboard) was available. Therefore, a satellite SST had to be used. When using a satellite SST two important facts must be remembered. Firstly, the SST can be considered to be of the skin, i.e. similar to the measurements acquired by the radiometer in this study. Secondly, satellite values will seldom directly correspond to the time of the profiles or the actual position needed for the prediction, which could differ considerably from the actual conditions at the required site. This was illustrated by the use of the MODIS data in the comparison, as the satellite (MODIS) provided a value averaged over approximately a 4.4 km^2 area and approximately 3 hours before the actual measurement time. This area incorporated the complete SJ transect line, which was shown to have complex

oceanographic conditions and the possibility of inhomogeneity along the path. This SST was therefore not considered to be representative of the SST experienced during this profile, but had to be used as it was the only SST data available. The ASTD calculated using this SST was positive for both the Helikite and the radiosonde predictions (Table 13). When using this as input to TARMOS, the predicted profiles showed little to no agreement with the measured profiles (Figure 38, 39 and 40).

From the results discussed above, it seems like TARMOS, and in effect micrometeorology theory perform better when using the 'bucket' SST at 0.5 m below the surface as it rendered the most comparable results to that of the measured profiles. Possible explanations for the above could be that the theory is based on bulk parameterisations, and that the 'bucket SST' was the most common measurement technique and therefore the measurement used to validate the models. The predicted profiles using the satellite SST showed similar trends to that of the SST from the radiometer with little to no agreement with measured values. Thus, when using micrometeorology theory to describe the atmospheric conditions in False Bay, it is important to understand that the SST conditions can change over a short distance and therefore using a SST from a satellite is less desirable than having a measured SST (bucket). Although it was not tested, it would be recommended that SST inputs from oceanographic models are used with caution until the sensitivity of TARMOS is tested with regards to the model. It is also possible that the resolution of the respective models could miss the complexity of the ocean properties.

After careful consideration of the water column properties and the ASTD as a result of the different SST measurements, it became clear that the synoptic atmospheric conditions in False Bay also play a significant role in the predictions. The first three profiles displayed a 'double-layered' atmosphere with variable conditions seen in the lower 50 m followed by more constant conditions above (Figures 25 to 33). This could be as a result of the geographical location and the effect of the surrounding mountains on the general atmospheric flow in the Bay. A basic study exploring the sea-breeze induced patterns in False Bay (Bonnardot, V., Planchon, O., Carey, V. and Cautenet, 2002) found that a thermal inversion was present over the ocean during the day, as a result of the relatively colder ocean temperatures contributing to the stabilisation of the lower atmosphere. This thermal inversion could possibly be used to explain the lower 50 m showing mostly variable conditions as all profiles were taken during the day. The JASIN experiment in the North Sea (Businger & Charnock, 1983), also found a near-neutral stability in coastal areas where warmer air from the land flowed over the relatively cooler water temperature, which created a shallow boundary layer (Garratt, 1994). These

coastal conditions are representative of False Bay, especially where the profiles where taken. This aspect was however not investigated further during the course of this thesis.

Furthermore it emerged that there were two profiling days where the predictions compared well with the measurements (Profile 1 and 3), and two where the predictions compared poorly with the measurements (Profiles 2 and 4). These findings could not be explained by only looking at the oceanic properties. A closer look at the general atmospheric conditions provided an interesting result (Table 14). Parameters such as wind direction, air temperature and wave height did not show a significant impact as there was no discernible resemblance between the days of Profiles 1 and 3. In fact, the conditions during Profile 1 were in almost all the cases completely different to that of the other profile days. Environmental parameters were however similar on the three sampling days after (Profiles 2 to 4). The parameter that stood out as a possible explanation for the grouping of Profile 1 and 3 and Profile 2 and 4 was precipitation. On the days where the predictions matched the measurements best, no rain was present, in contrast to rain recorded on the days with a weak comparison.

It was therefore useful to compare the performance of TARMOS predictions during 'wet' and 'dry' conditions. Of the predicted TARMOS profiles only one (using the surfboard values) showed a good comparison to the measured profiles during the dry conditions when compared for all parameters. All predicted profiles (TARMOS) however showed significant variation (Section 4.2 a and c). The measured profiles during the 'wet' conditions differed considerably from all the predicted profiles (Section 4.2 b and d), with the TARMOS predicted profiles showing more of an agreement when compared to each other (Section 4.2 b and d). This result show that the changing atmospheric conditions accompanying an approaching cold front or that possibly occur during a rainfall event, can prove difficult for TARMOS to predict. With this in mind and considering the second objective of this thesis, it became essential to briefly describe the basic rainfall patterns in the study area in order to determine the overall suitability of TARMOS in False Bay.

Data from 2004 to 2015, supplied by the South African Weather Service (SAWS) for three weather stations in False Bay (Strand (S), Simon's Town (ST) and Fish Hoek (FH)) indicated that the area on average will experience between 53 and 93 days of rainfall annually. An increase in number of days with a recorded rainfall is seen between May and August, with August recording up to 16 rainy days (Figure 41), which is to be expected as these areas are considered to be in a winter rainfall climate (Section 3.1).

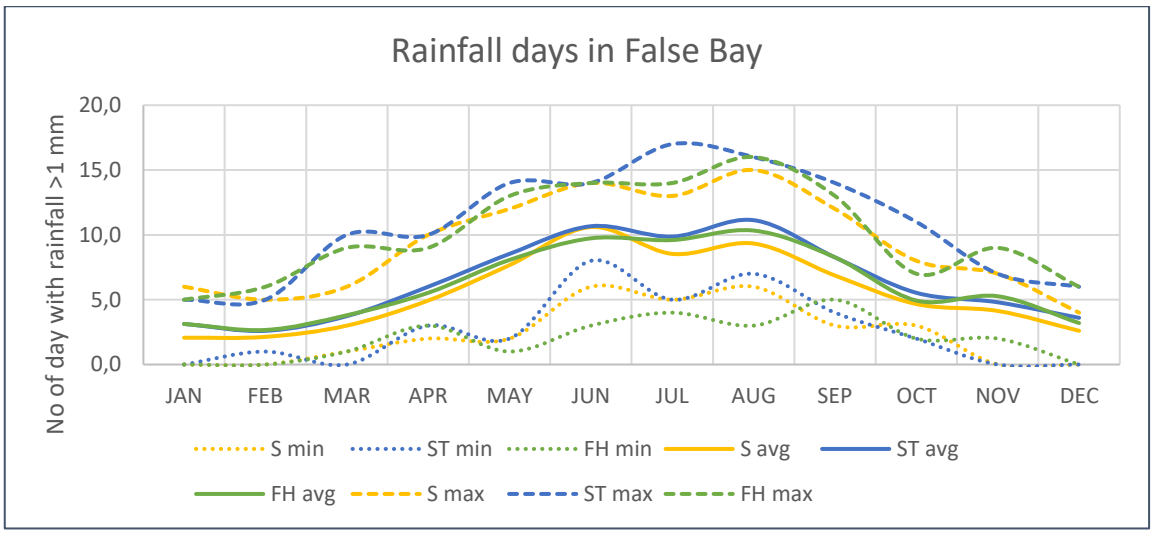

Figure 41: Basic rainfall descriptive statistics (minimum, average and maximum) in False Bay (Data supplied by SAWS)

It should therefore be noted that TARMOS must be used with caution during the winter months in the area of interest, and that it could be ineffective for approximately 20% of the year based solely on rainfall figures and the changing atmospheric conditions that are associated with the seasonal rainfall in the study area.

During the analyses of the environmental parameters above, it became apparent that the localised oceanographic and atmospheric parameters are indicative of a more complex system. The area where the air profiles were recorded is in an area where smaller scale local effects are dominant adding to the complexity of the data, which could explain some of the discrepancies encountered when attempting to reproduce the measured profiles using micrometeorology bulk parameterisations.

As this thesis formed part of larger international experiment with a more operational focus, it was also of interest to present a short discussion regarding the effect of the vertical air profiles on EO propagation prediction in False Bay. In order to illustrate the impact the different atmospheric inputs could have on EO propagation prediction, two of the profiles presented in Section 4 were used. Based on the observations above regarding the differences in model performance during 'dry' and wet' conditions, only Profile 2 (wet) and Profile 3 (dry) were used for this demonstration. The measured and TARMOS predicted profiles for the different conditions were used as input into the tactical decision aid EOSTAR, in order to produce a ray-trace plot for each of the scenarios. A sensor height of 10 m above sea level has been assumed for these simulations. These plots are presented below and the differences between the different air profiles are clear.

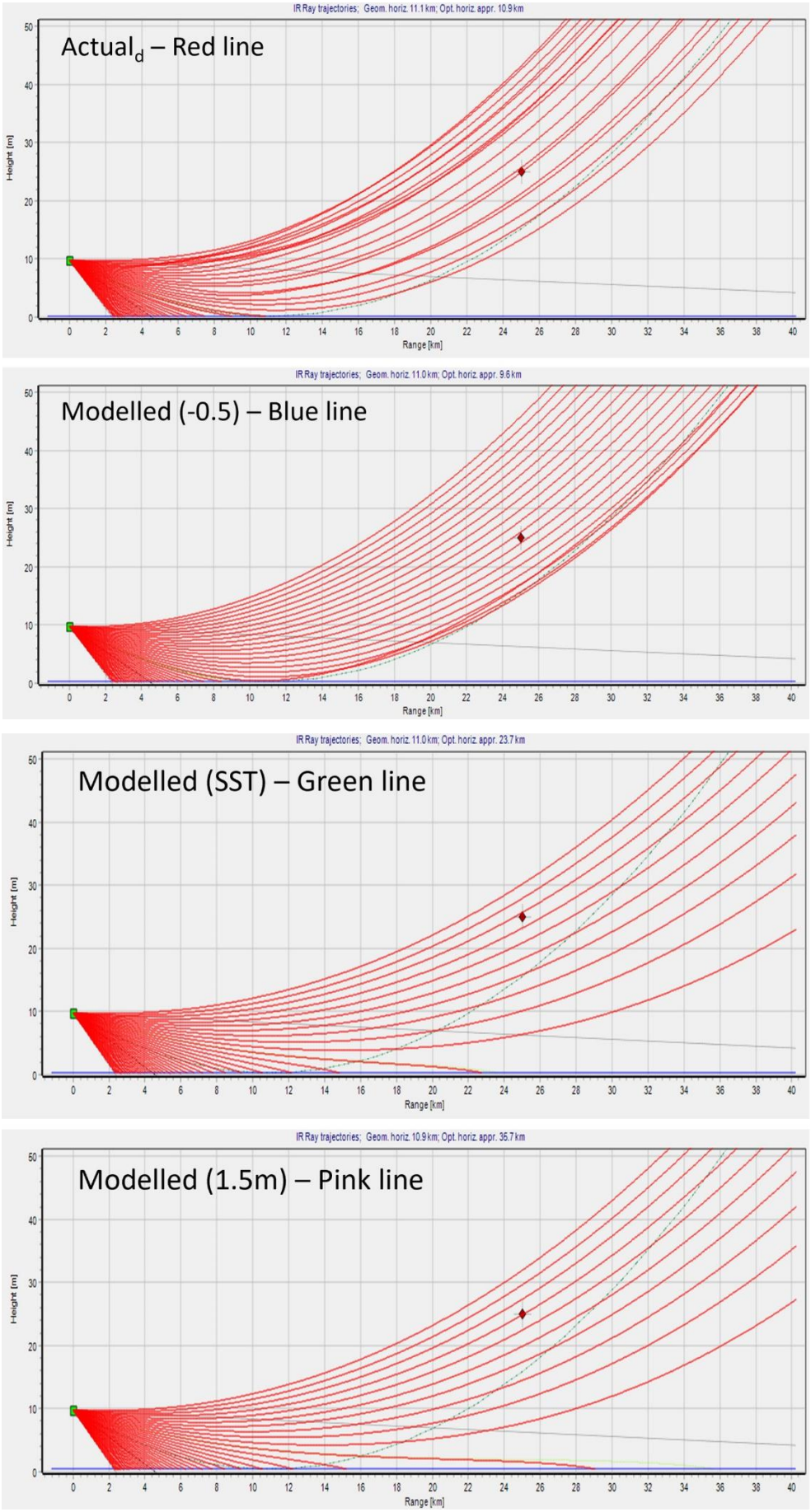

Figure 42: Ray trace predictions using inputs during Profile 3 (dry conditions). Line colours given refer to Figures 31-33

For Profile 3, when the TARMOS predictions better represented the actual measurements, an optical horizon of 10.9 km is predicted when the measured atmospheric conditions are used. The TARMOS prediction using the 'bucket' SST that closely resembled the actual profiles for all parameters had an optical horizon of 1.3 km less (9.6 km). Both profiles using the 'skin' SST showed an increased optical horizon at 23.7 km and 35.7 km respectively (Figure 42).

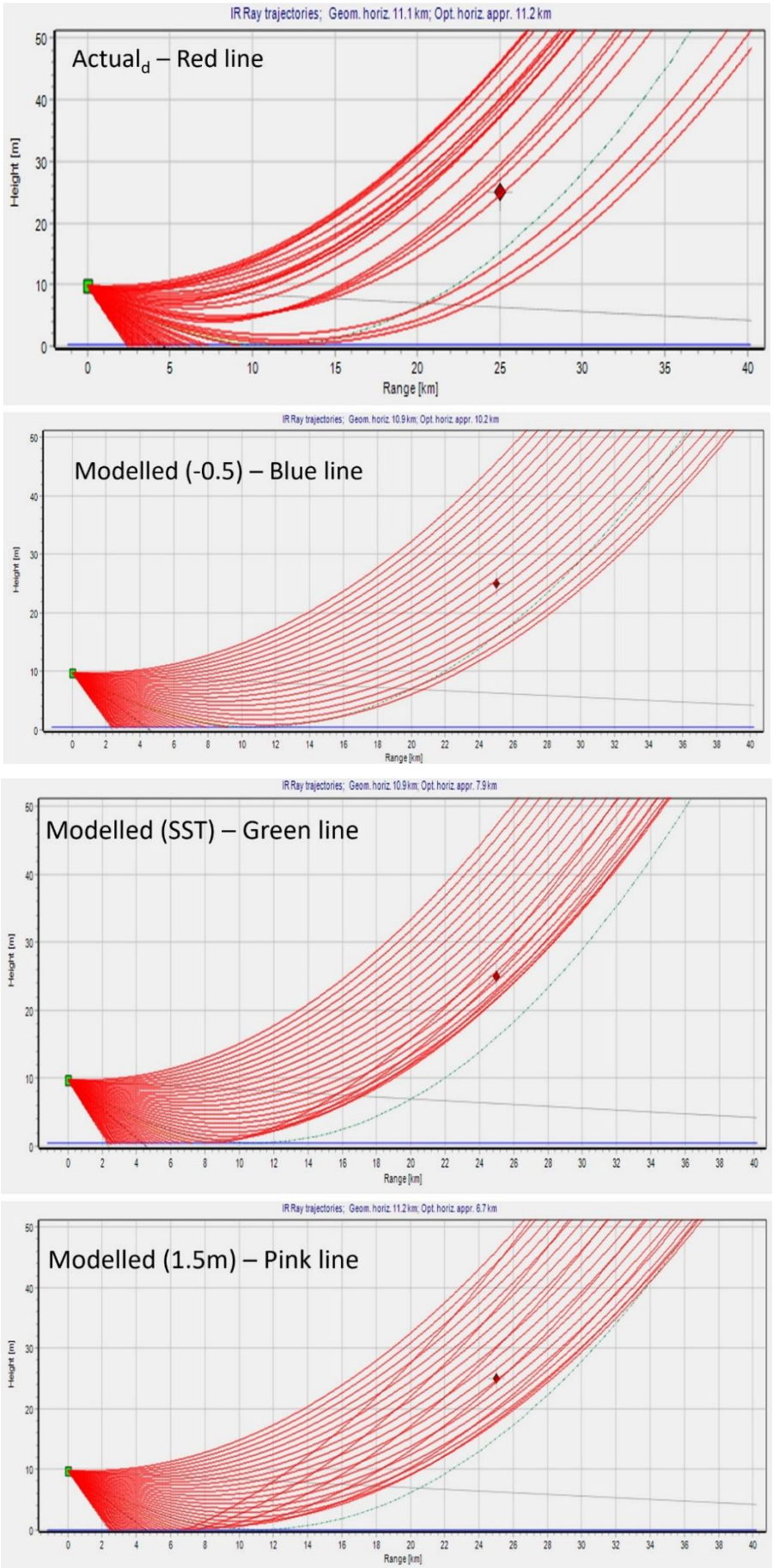

Figure 43: Ray trace predictions using inputs during Profile 2 (wet conditions). Line colours given refer to Figures 28-30

For Profile 2, where the TARMOS predictions showed less comparison to the actual profile, an optical horizon of 11.2 km is seen when using the measured parameters. This was 1 km further than that of the profile predicted using the 'bucket' SST (Figure 43). The distance at which a target would be visible to the EO equipment became less for both profiles that used the 'skin' SST as input (7.9 and 6.7 km respectively).

This is an important observation as the optical horizon in EO propagation represents the distance up to which an EO system will 'see' a target. In the cases above it is apparent that the wrong input parameters into EOSTAR can overestimate this distance by more than 10 km (Figure 42) or underestimate it by approximately 2 km (Figure 43).

It should also be noted that the discussion above was based on only four complete air profiles, and can by no means be considered to be statistically sound. The limited data were due to the fact that it was an investigative set-up during a complex and multi-disciplined international collaborative experiment where time was limited. Given the many objectives of the FESTER experiment, this investigative study had to fit into a schedule where more established data gathering techniques took preference. However, even with the limited data, the results proved interesting and worthy of further exploration in similar experiments.

CHAPTER 6: CONCLUSION

The concept of measuring the atmosphere using a kite is by no means new. Reference to atmospheric measurements using a kite to provide profiles dates to 1915 (Taylor & Shaw, 1915). And although this was ground breaking at the time, equipment did not always lend itself to the frequency of sampling that can be achieved in present days. Work done in 1915 relied heavily on spot measurements and extrapolations of a profile. Problems encountered also included the measurement of the sea surface temperature. This work however paved the way for other research as described in Section 2.5 and proved invaluable to the current understanding of micrometeorology over the ocean and the intricacies of measuring the maritime ASL.

Thus, although this study again proved that air profiles could successfully be measured using a Helikite as a lifting platform, it should be stated that the platform is not the important parameter that distinguished this work from previous studies. The successes achieved were more closely related to the advances in measurement technology (atmospheric and oceanic) that allowed for accurate data recording at an update rate of 1 – 4s.

Furthermore, new developments in unmanned aerial vehicles (UAV's), specifically drones, since a 2001 study (Muschinski et al., 2001) has opened the field considerably for atmospheric research. A recent article in the Meteorological Technology International highlighted the benefits of UAV's as they are becoming more affordable. Using drones or UAV's will add flexibility to research and enable data recording in more extreme environmental conditions. Care should however be taken to ensure that the measuring equipment is mounted in such a way that the platforms propelling system does not interfere with the parameters to be recorded.

While the Helikite system was considered to be successful it should be noted that it did take approximately 60 minutes to complete a profile, which should be considered when the data are used to evaluate the suitability in using micrometeorology theory for describing the marine surface layer in the study area. On two occasions (Profiles 2 and 4) it started raining during the time it took to record a profile, which led to changing atmospheric conditions as the profile was taken. This change is clearly visible when comparing the ascending and descending profiles on those days. Therefore it stands to reason that the TARMOS profiles must be aligned with the exact times of the change in order to have a chance of it being valid. In other words, TARMOS will only provide a prediction during a specific snapshot in time and will have

difficulty in representing the change in the environment. It is therefore a fair assumption that TARMOS (as a snapshot prediction) will not be comparable to the environment in False Bay when the conditions to be predicted were preceded by a low pressure system or cold front.

In analysing the results it seemed that the predictions were reliant on the localised 'now' conditions at the actual site as input. This led to the important observation that the TARMOS model (and in essence the bulk micrometeorological parameterisations) have a relatively small area of influence in a dynamic environment. The sensitivity of TARMOS to the changing False Bay environment has not yet been determined and could prove useful for future studies.

Studies in Denmark and Chesapeake Bay highlighted the importance of wave state in shallow water and fetch limited conditions (Vickers & Mahrt, 1998 and Lin, Sanford, Suttles, & Valigura, 2002). Currently the TARMOS model uses a standard C_D based on values from the North Sea, which might differ from that in False Bay. And although the waves were measured during the FESTER experiment it was not analysed to this level. It would therefore be an interesting theoretical exercise to calculate the C_D for False Bay, even though it is unlikely to have a great influence on the TARMOS outputs when using Helikite profiles.

Results hinted on the importance of the local geographical features surrounding False Bay and their effect on the general atmospheric conditions in order to fully understand the structure of the air column over the ocean in False Bay. This aspect was not investigated further in this thesis. A separate study by the Fraunhofer Institute in Germany investigated this using WRF modelling (Sprung et al., 2018). It is strongly recommended that the two studies should be looked at in parallel in future to understand the impact on any micrometeorological model used to predict air profiles in the area. All parameters in this study was looked at in isolation as the main focus was on the actual measurement techniques and the comparison of each parameter with the TARMOS model output, and the effect of the different physical parameters on each other were not considered.

Although results showed that the water column structure did not really affect the predicted profiles at the measurement site, it could have more of an impact on EO propagation over that path. It is therefore not considered to be of great importance in the scientific context of this thesis, but could present a real problem in the operational field. Results highlight the fact that the oceanic conditions in False Bay change on relatively small scales and the bulk SST could differ considerably from one point to the next. Numerical models that utilise the micrometeorological theory in predicting EO transmission might have to allow for more than

one input point across the transmission path in order to accommodate the changing water column properties. This would mostly be important when the water column is stratified and a shallow thermocline is present.

Various previous studies described experiments and techniques to record relevant data (Section 2.5) for describing micrometeorology, but in most cases focused on only one parameter at a time. For example, the scanning radiometers used by (Cimini et al., 2003)) only provided the skin SST and an air temperature profile. Other systems like the ASIS multipurpose buoy (Graber et al., 2000), proved useful in ASTD studies, but showed limitations in terms of height for the measurement of an atmospheric profile. The complexity of the environment in False Bay, as described in Section 5, thus highlighted the importance of measuring the general weather, wave and water column properties in addition to air profiles. These datasets provided a better understanding of the micrometeorological processes that were obtained in the study area, and emphasised the need for reliable measurement techniques (air profiling) and knowledge of the natural driving forces when conducting experiments, such as FESTER.

REFERENCES

A.M.J. van Eijk, M.A.C. Degache, D.J. de Lange, S. M. H. and D. T. (2010). EOSTAR Pro: a flexible extensive library to assess EO sensor performance. In J. . Stein, K. & Gonglewski (Ed.), *Optics in Atmospheric Propagation and Adaptive Systems XIII*. https://doi.org/10.1117/12.868184

Arya, P. S. (2001). *Introduction to Micrometeorology* (Vol. 79). Academic Press.

Augstein, E., Schmidt, H., & Ostapoff, F. (1974). The vertical structure of the atmospheric planetary boundary layer in undisturbed trade winds over the Atlantic Ocean. *Boundary-Layer Meteorology*, *6*, 129–150.

Ayra, S. P. (1988). *Introduction to Micrometeorology* (Frist; J. . Dmowska, R, and Holton, Ed.). Academic press, inc.

Bauer, E. (1996). *Effects of the Atmospheric refraction on long range near surface electro-optical sensing over water*. Institute for Defense Analyses, Document D-1815

Birol Kara, A., Rochford, P. A., & Hurlburt, H. E. (2000). Efficient and Accurate Bulk Parameterizations of Air – Sea Fluxes for Use in General Circulation Models. *Journal of Atmospheric and Oceanic Technology*, *17*(10), 1421–1438. https://journals.ametsoc.org/doi/full/10.1175/1520-0426%282000%29017%3C1421%3AEAABPO%3E2.0.CO%3B2

Bonnardot, V., Planchon, O., Carey, V. and Cautenet, S. (2002). *Diurnal wind, relative humiduty and temperature variation in the Stellenbosch-Groot Drakenstein Wine-growing area*. South African Journal of Enology and Viticulture (South Africa), Vol 23, No. 2, 2002.

Businger, J. A., & Charnock, H. (1983). Boundary layer structure in relation to larger-scale flow: some remarks on the JASIN observations. *Philosophical Transactions of the Royal Society of London. Series A, Mathematical and Physical Sciences*, *308*(1503), 445–449.

Cimini, D., Shaw, J. A., Westwater, E. R., Han, Y., Irisov, V., Leuski, V., & Churnside, J. H. (2003). Air temperature profile and air/sea temperature difference measurements by infrared and microwave scanning radiometers. *Radio Science*, *38*(3), MAR10/1-MAR10/19. https://doi.org/10.1029/2002RS002632

Davidson, B. (1968). the Barbados Oceanographic and Meteorological Experiment. *Bulletin of the American Meteorological Society*, *49*(9), 928–935. https://doi.org/10.1175/1520-0477-49.9.928

Data sheet DFM-09 GRAW radiosondes. Vol 1.13 https://www.graw.de/fileadmin/cms_upload/en/Resources/.pdf

Driggers, R. G., Cox, P., & Edwards, T. (1999). *Introduction to Infrared and Electro-optical Systems*. Bosten London, Artech House.

Dufois, F., & Rouault, M. (2012). Sea surface temperature in False Bay (South Africa): Towards a better understanding of its seasonal and inter-annual variability. *Continental Shelf Research*, *43*, 24–35. https://doi.org/10.1016/j.csr.2012.04.009

Dyer, A. J. (1967). The turbulent transport of heat and water vapour in an unstable atmosphere. *Quarterly Journal of the Royal Meteorological Society*, *93*(398), 501–508. https://doi.org/10.1002/qj.49709339809

Eisele, C., Seiffer, D. P., Stein, K., Sucher, E., Gunter, W. H., February, F., … Griffith, D. (2016). FESTER: A propagation experiment, overview and first results. *Proceedings of SPIE - The International Society for Optical Engineering*, *10002*. https://doi.org/10.1117/12.2240771

Farmer, W. M. (2001). *The Atmospheric Filter, Volume I, Sources*. JCD Publishing.

Garratt, J. R. (1994). Review: the atmospheric boundary layer. *Earth-Science Reviews*, *37*(1–2), 89–134. https://doi.org/10.1016/0012-8252(94)90026-4

Geernaert, G., & Katsaros, K. B. (1986). Incorporation of Stratification Effects on the Oceanic Roughness Length in the Derivation of the Neutral Drag Coefficient. *Journal of Physical Oceanography*, *16*(9), 1580–1584. https://doi.org/10.1175/1520-0485(1986)016<1580:IOSEOT>2.0.CO;2

Geernaert, G L. (1990). Bulk Parameterizations for the Wind Stress and Heat Fluxes. In G L Geernaert & W. L. Plant (Eds.), *Surface Waves and Fluxes: Volume I --- Current Theory* (pp. 91–172). https://doi.org/10.1007/978-94-009-2069-9_5

Geernaert, Gerald L., Katsaros, K. B., & Richter, K. (1986). Variation of the drag coefficient and its dependence on sea state. *Journal of Geophysical Research: Oceans*, *91*(C6), 7667–7679. https://doi.org/10.1029/JC091iC06p07667

Gildenhuys, S. and Wainman, C. K. (2012). *Long-term ocean health monitoring in Simon's bay: consolidated results of project amber(2000 – 2012)*. IMT, Simon's Town, South Africa, report TV0010-212058-730 (2012).

Graber, H. C., Terray, E. A., Donelan, M. A., Drennan, W. M., Van Leer, J. C., & Peters, D. B. (2000). ASIS-a new Air-Sea Interaction Spar buoy: Design and performance at sea. *Journal of Atmospheric and Oceanic Technology*, *17*(5), 708–720. https://doi.org/10.1175/1520-0426(2000)017<0708:AANASI>2.0.CO;2

Gunter, W. H. (2010). *Thermal Infrared Systems Curriculum*. IMT internal report, Simon's Town, South Africa.

Gunter, W. H. (2014). *FESTER STATUS REPORT: PHASE 1*. IMT, Simon's Town, South Africa, report TV0010-215001-730 (2014)

Gunter, W. H. (2017). *FESTER DATA ANALYSIS STATUS AND RESULTS*. IMT, Simon's Town, South Africa, report TV0010-217002-730 (2017)

K. Taylor, P., & Yelland, M. (2000). The Dependence of Sea Surface Roughness on the Height and Steepness of the Waves. *J. Phys. Ocean.*, *31*, 572–590. https://doi.org/10.1175/1520-0485(2001)031<0572:TDOSSR>2.0.CO;2

Kettle, A. J. (2015). A Diagram of Wind Speed Versus Air-sea Temperature Difference to Understand the Marine atmospheric Boundary Layer. *Energy Procedia*, *76*, 138–147. https://doi.org/10.1016/j.egypro.2015.07.879

Kondo, J. (1975). Air-sea bulk transfer coefficients in diabatic conditions. *Boundary-Layer Meteorology*, *9*(1), 91–112.

Kunz, G. J. (1996). *A bulk model to predict optical turbulance in the marine layer*. TNO report FEL-96-A053

Lin, W., Sanford, L. P., Suttles, S. E., & Valigura, R. (2002). Drag Coefficients with Fetch-Limited Wind Waves*. *Journal of Physical Oceanography*, *32*(11), 3058–3074. https://doi.org/10.1175/1520-0485(2002)032<3058:DCWFLW>2.0.CO;2

Liu, W. T. L., Katsaros, K., & Businger, J. (1979). Bulk Parameterization of Air-Sea Exchanges of Heat and Water Vapor Including the Molecular Constraints at the Interface. *Journal of Atmospheric Sciences*, *36*, 1722–1735. https://doi.org/10.1175/1520-0469(1979)036<1722:BPOASE>2.0.CO;2

MacKellar, M. C., McGowan, H. A., & Phinn, S. R. (2013). An observational heat budget analysis

of a coral reef, heron reef, great barrier reef, Australia. *Journal of Geophysical Research Atmospheres*, *118*(6), 2547–2559. https://doi.org/10.1002/jgrd.50270

Muschinski, A., Frehlich, R., Jensen, M., Hugo, R., Hoff, A., Eaton, F., & Balsley, B. (2001). Fine-scale measurements of turbulence in the lower troposphere: An intercomparison between a kit-and balloon-borne, and a helicopter-borne measurement system. *Boundary-Layer Meteorology*, *98*(2), 219–250. https://doi.org/10.1023/A:1026520618624

Naicker, K., Anderson, F., Le Roux, A., & Alhuwaimel, S. (2011). Validation of vertical refractivity profiles as required for performance prediction of coastal surveillance radars. *Saudi International Electronics, Communications and Photonics Conference 2011, SIECPC 2011*. https://doi.org/10.1109/SIECPC.2011.5876967

Panofsky, H. A., & Dutton, J. A. (1984). Atmospheric turbulence, John Wiley. *New York*.

Pollard, R. T., & Gu, E. (1978). *The Joint Air-Sea Interaction Experiment - JASIN 1978*. *59*(10), 1310–1318.

Roychoudhuri, C., & Pedrotti, L. (2009). Basic Geometrical Optics. In *Fundamentals of Photonics*. https://doi.org/10.1117/3.784938.ch3

Schlitzer, R. (2019). *Ocean Data View*.

Shaw, J. a, Cimini, D., Westwater, E. R., Han, Y., Zorn, H. M., & Churnside, J. H. (2001). Scanning infrared radiometer for measuring the air-sea temperature difference. *Applied Optics*, *40*(27), 4807–4815. https://doi.org/10.1364/AO.40.004807

Smith, S. D., Fairall, C. W., Geernaert, G. L., & Hasse, L. (1996). Air-sea fluxes: 25 years of progress. *Boundary-Layer Meteorology*, *78*(3–4), 247–290. https://doi.org/10.1007/BF00120938

Smith, Stuart D. (1988). Coefficients for sea surface wind stress, heat flux, and wind profiles as a function of wind speed and temperature. *Journal of Geophysical Research: Oceans*, *93*(C12), 15467–15472.

Sprung, D., van Eijk, A. M. J., Ullwer, C., Gunter, W., Eisele, C., Seiffer, D., … Stein, K. (2018). Optical turbulence in the coastal area over False Bay, South Africa: comparison of measurements and modeling results. In K. U. Stein & S. Gladysz (Eds.), *Environmental Effects on Light Propagation and Adaptive Systems* (Vol. 10787, pp. 1 – 8). https://doi.org/10.1117/12.2325609

Talley, L. D., Pickard, G. L., Emery, W. J., & Swift, J. H. (2011). *Descriptive Physical Oceanography: An Introduction* (6th ed.), Acedemic Press.

Taylor, G. I., & Shaw, W. N. (1915). I. Eddy motion in the atmosphere. *Philosophical Transactions of the Royal Society of London. Series A, Containing Papers of a Mathematical or Physical Character*, *215*(523–537), 1–26. https://doi.org/10.1098/rsta.1915.0001

Tennekes, H. and Lumley, J. L. (1972). *A First Course in Turbulence*. MIT Press.

Van Eijk, A. M. J. (2013). *The metereological processor of EOSTAR and the Delphi libraries*. TNO Report R10941

Van Eijk, A. M. J., Gunter, W. H., February, F. J., Maritz, B., Vrahimis, G., Koago, M. S., … Griffith, D. (2016). The FESTER field trial. *Proceedings of SPIE - The International Society for Optical Engineering*, *9979*. https://doi.org/10.1117/12.2240642

Vickers, D., & Mahrt, L. (1998). Fetch limited drag coefficients. In *Kluwer Academic Publishers*.

http://citeseerx.ist.psu.edu/viewdoc/download?doi=10.1.1.40.1388&rep=rep1&type=pdf

Wainman, C. K. (2000). *Water quality and processes in Simon's Bay*. University of Cape Town.

Wesely, M. L. (1980). Comments on "Bulk Parameterization of Air-Sea Exchanges of Heat and Water Vapor Including the Molecular Constraints at the Interface." *Journal of the Atmospheric Sciences*, Vol. 37, pp. 2798–2800. https://doi.org/10.1175/1520-0469(1980)037<2798:COPOAS>2.0.CO;2

APPENDIX A - TECHNICAL SPECIFICATIONS OF THE HELIKITE AND WINCH

Table 1: Summary of the technical specifications for the Skyhook 3.0 Helikite

Helium Capacity	3 m^3
Lift in no wind:	1.5 kg
Lift in 24 km/h wind:	6 kg
Max. wind speed (approx.):	56 km/h
Max. altitude unloaded (approx.):	1000 m
Helikite length inflated:	3.0 m
Helikite width inflated:	1.65 m
Balloon material thickness (thou' inch):	2 Thou/inch
Helium quality	High quality, 99.999%
Helikite performance:	All figures for performance above are for Imperial Standard Temperature & Pressure conditions
	Extra heat, humidity, and height will reduce lift.
	Rain, snow, dew and mist all add weight over the entire surface of a Helikite, which will reduce the lifting capacity

Table 2: Summary of the technical specifications for the Kingcone Winch TDS-9.5CY

Line pull:	4,309 kgs
Motor:	12V/5.0HP 24V/3.0HP
Gear Train:	Three stage
Gear Ratio:	173:1
Freespooling Clutch:	Rotating ring gear
Dyneema string size:	*Φ11/32"×100'(Φ8.7mm×30m)*
Dyneema string Type:	*Aircraft A7×19*
Drum Size:	Φ2.5"×9"(Φ63.5mm×229mm)
Weight:	44.5kg

Table 3: Line pull per layer of wire rope

Layer of Wire Rope	Max Line Pull
1	4,309kgs
2	3,500kgs
3	2,977kgs
4	2,578kgs

Table 4: Line speed and amp draw (1st layer of rope on the drum)

Load	Line Speed	AMP Draw(12V)	AMP Draw(24V)
No Load	55.8FPM/17MPM	60	40
907kgs	14.7FPM/4.5MPM	140	106
1,814kgs	12.5FPM/3.8MPM	181	158
2,722kgs	8.9FPM/2.7MPM	248	187
3,650kgs	8.2FPM/2.5MPM	295	226
4,309kgs	7.5FPM/2.3MPM	338	259

The dimensions (mm) of the winch is provided in Figure 1.

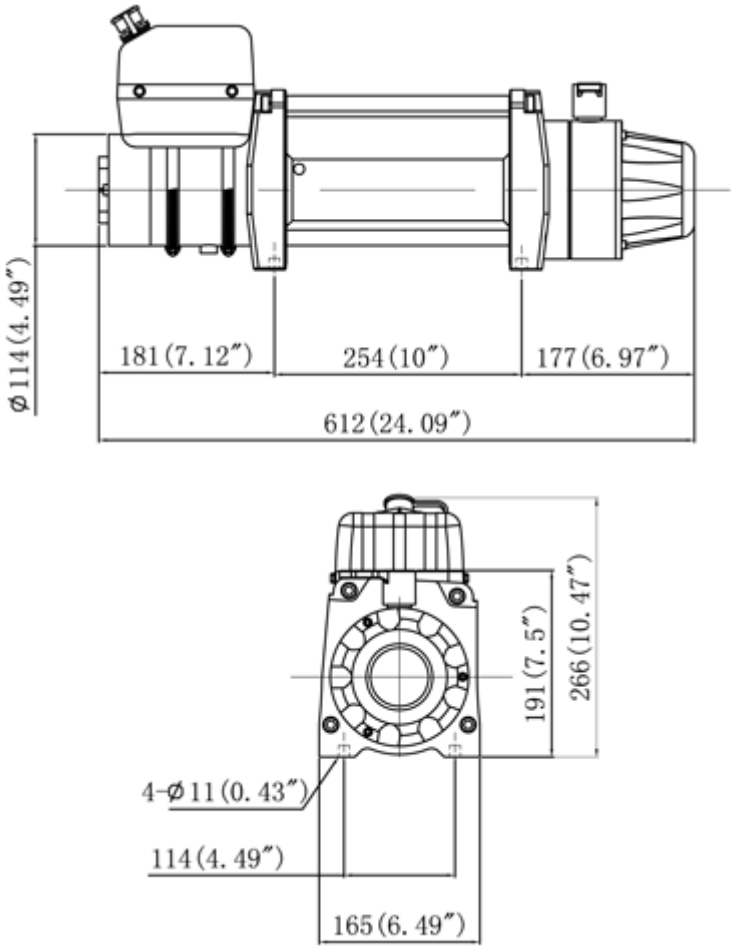

FIGURE 1: DIMENSIONS OF THE WINCH

APPENDIX B - TECHNICAL SPECIFICATION OF THE HELIKITE SENSOR PACKAGE

- Airmar PB200 weather station
  - Wind Speed Range: 0 knots to 80 knots
  - Wind Speed Resolution: 0.1 knots
  - Wind Speed Accuracy @ 0°C to 55°C, no precipitation*:
    - Low Wind Speeds: 0 knots to 10 knots; RMS error of 1 knot +10% of reading
    - High Wind Speeds: 10 knots to 80 knots; RMS error of 2 knots or 5% RMS, whichever is greater
  - Wind Speed Accuracy in wet conditions: 5 knots RMS
  - Wind Direction Range: 0° to 360°
  - Wind Direction Resolution: 0.1°
  - Wind Direction Accuracy @ 0°C to 55°C, no precipitation:
    - Low Wind Speeds: 4 knots to 10 knots; 5° RMS typical
    - High Wind Speeds: >10 knots; 2° RMS typical
  - Wind Direction Accuracy in wet conditions: >8 knots; 8° RMS typical
  - Compass Accuracy:
    - 1° static heading accuracy
    - 2° dynamic heading accuracy
  - Rate-of-Turn: 0° to 70° per second
  - Rate-of-Turn Accuracy: 1° per second
  - Rate-of-Turn Data Output Update Rate:
    - 2 Hz—NMEA 0183 (Adjustable up to 10 Hz)
    - Adjustable up to 20 Hz—NMEA 2000
  - Pitch and Roll Range/Accuracy: ±50° in 4 knot wind
  - Barometric Pressure Range: 850 mbar to 1150 mbar
  - Barometric Pressure Resolution: 0.1 mbar
  - Barometric Pressure Accuracy: ±2 mbar when altitude correction is available
  - GPS Position Accuracy: 3 m (10') with WAAS/EGNOS (95% of the time, SA off)
  - Operating Temperature Range: -25°C to 55°C
  - Supply Voltage: 9 VDC to 16 VDC
  - Supply Current: <220mA
  - Weight: 285g
  - Dimensions
- LM35 – Air and water temperature sensor
  - Calibrated Directly in Celsius (Centigrade)
  - Linear + 10-mV/°C Scale Factor
  - 0.5°C Ensured Accuracy (at 25°C)
  - Rated for Full −55°C to 150°C Range
  - Suitable for Remote Applications
  - Operates from 4 V to 30 V
  - Less than 60-µA Current Drain
  - Low Self-Heating, 0.08°C in Still Air
  - Non-Linearity Only ±¼°C Typical
  - Low-Impedance Output, 0.1 Ω for 1-mA Load
  - Supply Min 4 Volt
  - Quiescent Current_ 56 uA
  - Temperature Min -40, -55, 0 deg C
  - Temperature Max 100, 110, 150 deg C

- Accuracy

Parameter	Conditions	LM35A		
		Typical	Tested Limit (Note 4)	Design Limit (Note 5)
Accuracy (Note 7)	T_A=+25°C	±0.2	±0.5	
	T_A=−10°C	±0.3		
	T_A=T_{MAX}	±0.4	±1.0	
	T_A=T_{MIN}	±0.4	±1.0	
Nonlinearity (Note 8)	$T_{MIN} \le T_A \le T_{MAX}$	**±0.18**		**±0.35**

  - Sensor Gain 10 mV/Deg C
  - The LM35 series are precision integrated-circuit temperature sensors, whose output voltage is linearly proportional to the Celsius (Centigrade) temperature.

- Data logger – SEEEDUINO Stalker
  - Compatible with Seeeduino (I/O ports use 3.3V Logic). Can be programmed with Arduino Processing language.
  - Onboard microcontroller: ATMega328P
  - Onboard Real Time Clock chip (Socket for a CR2032 Cell which acts as a backup power source for RTC)
  - Serial interface with DTR for auto reset during programming when operating in standalone mode. (For programming, UartSBee must be bought separately)
  - microSD card socket
  - 4 Pin Grove header (operation voltage is selectable: 5.0V or 3.3V)
  - I2C Pin header (operation voltage is selectable: 5.0V or 3.3V)
  - User LED on Digital pin 8(PB0)
  - Reset buttons for XBee Modules and ATMega328P

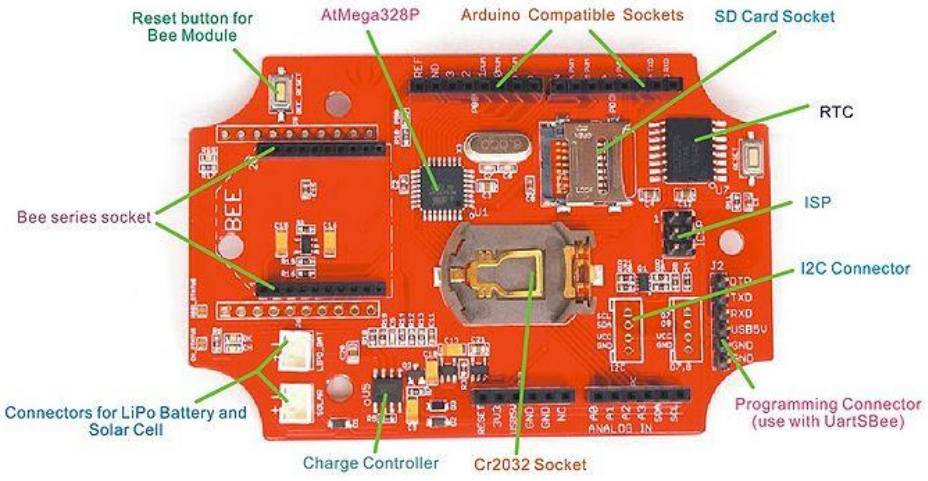

FIGURE 1: SEEEDUINO STALKER DATALOGGER

  - Key Technical Specifications

Microcontroller:	ATmega328P

On Board Crystal	8 MHz
PCB size:	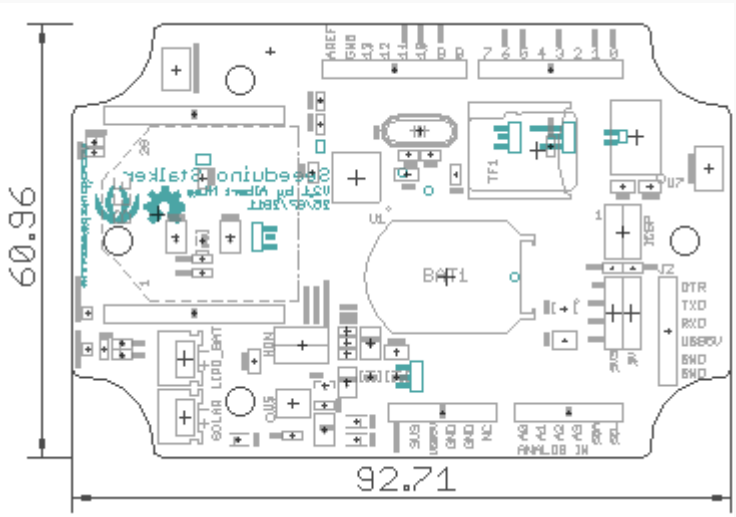 in millimeter
Indicators:	Reset, Power, LED on PB0 (Arduino Pin 8)
Power supply:	3.7v Lipo Battery, Use 5VDC solar panel for charging the battery.
Power Connector:	2 pin JST/ USB
I/O counts:	20
ADC input:	Dedicated 4 channel (ADC0~ADC3, 10 bit resolution)
Connectivity:	I^2C, UART, SPI
DS3231 RTC Accuracy:	±2ppm from 0°C to +40°C / ±3.5ppm from -40°C to +85°C
DS3231 Temperature SensorAccuracy:	±3°C

Kestrel weather station

- DIMENSIONS: 127MM X 45MM X 28MM
  - Weight: 102g
  - Wind speed:
    - Operational range 0.4m/s to 60m/s (0.8 to 135.0mph)
    - Specification range 0.4m/s to 40m/s (0.8 to 89.0mph)
    - On axis accuracy ± 3% of reading or ± 0.1 m/s. (Some loss of accuracy from bearing wear may occur with sustained operation at or near maximum speed)
    - Off -axis response -1% @ 5°, -2% @ 10°, -3% at 15°
    - Calibration drift <1% after 100hrs at 7 m/s
    - Resolution 0.1 kt, m/s, km/h, mph. 1 FPM below 1999 FPM, 10 FPM above 2000 FPM. 1 Beaufort (0 to 12)
  - Wind direction Forward Heading (1 sec response)
    - Operational range 360°
    - Specification range 0 to 360°
    - Accuracy ±5°
    - Resolution 1°, 16 point
  - Temperature (1 sec response)
    - Operational range -45.0°C to +125.0°C
    - Specification range -29.0°C to +70.0°C
    - Accuracy ±1°C
    - Resolution 0.1°
    - Wind chill accuracy ±1.0°C (from wind speed and temperature)
  - Relative Humidity (1 min response)
    - Operational range 0% to 100%
    - Specification range 5% to 95% non-condensing
    - Resolution 0.1%
    - Accuracy ±3% (when unit allowed to equilibrate to external temperature)
    - Calibration drift ±2% over 24 months (correctable)
    - Dew point accuracy ±2°C (above 20% relative humidity)
    - Heat index accuracy ±2°C (between 21.1°C and 54.4°C)
  - Barometric Pressure (1 sec response)
    - Operational range 10 to 1100 mbar at 25°C
    - Specification range 750 to 1100 mbar at 25°C Resolution 0.1 mbar
    - Accuracy ±1.5 mbar (max error over range 0°C to 70°C: ±2.0 mbar)
    - Calibration drift Typically ±1 mbar per year (correctable)
    - Wet bulb temperature accuracy ±2°C (between 0°C and 37.8°C)
    - Density altitude accuracy ±75m (between 0°C and 37.8°C)
  - Altitude (1 sec response)
    - Operational range -2000m to +9000m
    - Specification range -2000m to +6000m at 25°C
    - Accuracy ±15m (max error out of spec range: ±30m)
    - Performance Resolution 1m
  - Impeller Diameter 25mm. High precision axle and jewel (sapphire) bearings. User replaceable impeller assembly
  - Temperature thermally isolated, hermetically sealed precision thermistor
  - Relative Humidity Polymer capacitive sensor, mounted externally in thin-walled chamber
  - Pressure Monolithic piezo-resistive silicon based sensor with second-order temperature correction Sensors
  - Compass 2-axis solid state magneto-resistive sensor. Declination/variation adjustable for true north readout. Self calibration routine
  - Sealing Electronics enclosure IP67 [Water resistant]

APPENDIX C - TECHNICAL SPECIFICATION OF THE DFM-09 GRAW RADIOSONDE (*DFM-09*, n.d.)

GRS-KD-0038-en

DFM-09

Data Sheet

V01.13

Issue

Information on issue	
Document ID	GRS-KD-0038-en
Issue	V01.13
Date	May 2019

Issued by

Muggenhofer Str. 95
90429 Nuremberg
Germany
Phone: +49 911 3201 100
Fax: +49 911 3201 150
Email: info@graw.de

Table of Contents

1

1.1 Data Transmission

Data channels:	T, U, GPS (P optionally)
Free channels (optionally):	1 free channel, e. g. for an external sensor
Sampling rate:	T, U In total for all sensors for a TU radiosonde: 672 ms ➢ Measurement and transmission time for one sensor: 224 ms ➢ Reference measurement: 224 ms ➢ Every additional sensor increases the sampling rate by 224 ms
Coding:	Digital bi-phase Manchester
Transmission rate:	T, U ➢ Transmission rate of TU data: 1250 baud in a timeslot of 57.6 ms GPS ➢ Transmission rate of GPS data in 4 timeslots of 166.4 ms (224 ms - 57.6 ms = 166.4 ms); The transmission of the GPS-data is done in the background during the TU-measurement. One complete set of GPS data is transmitted per second in addition to the TU-transmission.
Error correction:	The microcontroller in the radiosonde expands 4 bits to 8 bits. By this operation it is possible to correct one error and detect two errors. Additionally, the radiosonde carries out an interleaving over 7 bytes.
Identification code:	Transmit of the identification code in the reference channel is possible (no change of the sampling rate of the sensors; sampling rate of about 2 s for the identification code) or instead of a sensor (the sampling rate of each sensor extends by 224 ms).

1.2 Transmitter

Type:	PLL Synthesizer based circuit
Tuning range:	400.01 MHz to 405.99 MHz
Channel spacing:	20 kHz
Frequency stability:	Δ f = ±3 kHz
Modulation:	FSK
Frequency deviation:	Δ f = ±3 kHz
Output power:	P = 100 mW ERP or 20 dBm
Harmonic suppression:	0 GHz to 1 GHz: P = -57 dBm From 1 GHz: P = -36 dBm
Antenna:	Quarter wave vertical monopol
RF polarisation:	Linear, vertical
Telemetry range:	250 km minimum

1.3 Power supply

Battery:	High Power Primary Lithium Battery with short circuit protection.
Source:	150 minutes minimum
Capacity:	1.4 Ah
International Transportation:	ICAO International Civil Aviation Organisation; IMO International Marine Organisation. Each battery cell contains less than 1 g of lithium or lithium alloy (less than 2.0 g for assembled batteries). Therefore the lithium batteries are considered as not dangerous and with short circuit protection air transport und sea transport is allowed.
Activating power supply:	Via slide switch

1.4 GPS

Receiving antenna type:	Patch
General:	Frequency L1 1575.42 MHz Code C.A. Code
Accuracy:	Position < 10 m 90 % Velocity < 0.1 m/s

1.5 Sensors

Installation of the sensors:	Temperature and humidity sensors are installed prior to launch.
Protection of sensors:	During the transport the temperature and the humidity sensors are protected inside the radiosonde housing.
Calibration:	Calibration coefficients are stored in an EEPROM on board of the radiosonde.
Transmission of calibration data:	Transmission of the calibration data to the groundstation before the launch via connection cable.
Recalibration before start:	Not required

1.5.1 Pressure sensor (optionally)

Type:	Piezo-resistive
Range:	10 - 1100 hPa
Accuracy:	Δ P = ±0.5 hPa
Resolution:	Δ P = ±0.1 hPa

1.5.2 Temperature sensor

Type:	Thermistor
Range:	-95 °C to +50 °C
Accuracy:	Δ T = ±0.2 °C
Resolution:	Δ T = ±0.01 °C

1.5.3 Humidity sensor

Type:	Capacitive polymer
Range:	0 to 100 % r. H.
Accuracy:	4 %
Resolution:	1 %

1.6 General data

Dimensions:	20 cm x 4 cm x 6 cm
Weight with batteries:	100 g
Housing:	Styrofoam
Operating temperature:	-95°C to +50°C
Storage conditions (open package):	Shelf life: 2 years Temperature: +5 to +40 °C rel. Humidity: 0 to 60 %
Storage conditions (vacuum package with dry powder):	Shelf life: 4 years Temperature: -40 to +40 °C rel. Humidity: 0 to 95 %